Instituto Alberto Luiz Coimbra de
Pós-Graduação e Pesquisa de Engenharia
COPPE
UFRJ

VALIDATION AND APPLICATION OF BREAKAGE MODEL IN THE DISCRETE ELEMENT METHOD THROUGH THE SIMULATION OF COMMINUTION SYSTEMS

Flávio Pereira André

Dissertação de Mestrado apresentada ao Programa de Pós-graduação em Engenharia Metalúrgica e de Materiais, COPPE, da Universidade Federal do Rio de Janeiro, como parte dos requisitos necessários à obtenção do título de Mestre em Engenharia Metalúrgica e de Materiais.

Orientador: Luís Marcelo Marques Tavares

Rio de Janeiro
Agosto de 2019

VALIDATION AND APPLICATION OF BREAKAGE MODEL IN THE DISCRETE ELEMENT METHOD THROUGH THE SIMULATION OF COMMINUTION SYSTEMS

Flávio Pereira André

DISSERTAÇÃO SUBMETIDA AO CORPO DOCENTE DO INSTITUTO ALBERTO LUIZ COIMBRA DE PÓS-GRADUAÇÃO E PESQUISA DE ENGENHARIA (COPPE) DA UNIVERSIDADE FEDERAL DO RIO DE JANEIRO COMO PARTE DOS REQUISITOS NECESSÁRIOS PARA A OBTENÇÃO DO GRAU DE MESTRE EM CIÊNCIAS EM ENGENHARIA METALÚRGICA E DE MATERIAIS.

Examinada por:

Prof. Luís Marcelo Marques Tavares, Ph.D.

Prof. Rodrigo Magalhães de Carvalho, D.Sc.

Prof. José Luis Drummond Alves, D.Sc.

Dr. Alexander Potapov, Ph.D.

RIO DE JANEIRO, RJ – BRASIL
AGOSTO DE 2019

André, Flávio Pereira

Validation and application of breakage model in the Discrete Element Method through the simulation of comminution systems/ Flávio Pereira André. – Rio de Janeiro: UFRJ/COPPE, 2019.

XVI, 121 p.: il.; 29,7 cm.

Orientador: Luís Marcelo Marques Tavares

Dissertação (mestrado) – UFRJ/ COPPE/ Programa de Engenharia Metalúrgica e Materiais, 2019.

Referências Bibliográficas: p. 114-121.

1. Cominuição. 2. Método dos elementos discretos. 3. Rocky DEM. I. Tavares, Luís Marcelo Marques. II. Universidade Federal do Rio de Janeiro, COPPE, Programa de Engenharia Metalúrgica e de Materiais. III. Título.

ACKNOWLEDGEMENTS

I would like to thank my family for their support throughout this journey. Without them, none of this would be possible. I would also like to thank my wife Hayla for being present whenever I needed and for providing the necessary encouragement for me to follow my goals.

I would like to express my gratitude to Professor Luís Marcelo for providing me with this opportunity and guiding me during this work. The knowledge and advices shared were fundamental to the success of the research.

I am also grateful for the help of Dr. Alex Potapov, not only in the immediate implementation of code changes, but also in sharing his extensive knowledge of the subject. Reaching this stage of the work was only possible due to his help.

I would also like to thank my colleagues at the Laboratório de Tecnologia Mineral for contributing with relevant knowledge on the topic and also for making the days we shared so enjoyable. They have made the laboratory a second home for me during this work, while enriching this dissertation in important discussions on the subject. The assistance of Professor Rodrigo Carvalho during this work is also very recognized.

The support of ESSS in providing new versions of the software on demand is also greatly acknowledged.

This study was financed in part by the Coordenação de Aperfeiçoamento de Pessoal de Nível Superior - Brasil (CAPES) - Finance Code 001.

Resumo da Dissertação apresentada à COPPE/UFRJ como parte dos requisitos necessários para a obtenção do grau de Mestre em Ciências (M.Sc.)

VALIDAÇÃO E APLICAÇÃO DE MODELO DE QUEBRA NO MÉTODO DOS ELEMENTOS DISCRETOS ATRAVÉS DA SIMULAÇÃO DE SISTEMAS DE COMINUIÇÃO

Flávio Pereira André
Agosto/2019

Orientador: Luís Marcelo Marques Tavares

Programa: Engenharia Metalúrgica e de Materiais

O presente trabalho descreve um modelo empírico-fenomenológico que cobre todos os aspectos relevantes da quebra de partículas e foi implementado na plataforma comercial Rocky DEM, adotando um esquema de substituição de partículas para representar a fragmentação de partículas. O modelo descreve propriedades fundamentais de partículas minerais, como a distribuição de energia de fratura em uma população de partículas, o efeito de tamanho na probabilidade de quebra, o enfraquecimento de partículas devido a impactos repetidos e a relação entre energia e a distribuição de tamanho de fragmentos. Numa primeira fase, a verificação do modelo foi realizada comparando os resultados do modelo analítico previamente ajustado aos dados experimentais com as simulações de testes de quebra de partículas individuais. A análise de sensibilidade das simulações variando diferentes parâmetros relevantes também foi realizada. Posteriormente, o modelo de simulação foi validado através da comparação de seus resultados com experimentos de teste de impacto em leitos de partículas não confinados. A boa concordância demonstra o potencial do modelo para simular sistemas mais complexos nos quais as simulações do DEM devem incluir uma descrição efetiva da quebra. Por fim, o modelo foi utilizado para a simulação de um britador cônico em escala de laboratório e um britador de impacto de eixo horizontal em escala piloto.

Abstract of Dissertation presented to COPPE/UFRJ as a partial fulfillment of the requirements for the degree of Master of Science (M.Sc.)

VALIDATION AND APPLICATION OF BREAKAGE MODEL IN THE DISCRETE ELEMENT METHOD THROUGH THE SIMULATION OF COMMINUTION SYSTEMS

Flávio Pereira André
August/2019

Advisor: Luís Marcelo Marques Tavares

Department: Metallurgical and Material Engineering

The present work describes a detailed empirical-phenomenological model that characterizes all relevant aspects of body breakage and has been implemented in the commercial DEM platform Rocky DEM, adopting a particle replacement scheme to represent particle fragmentation. The model describes fundamental properties of ore particles, such as the distribution of fracture energy among a population of particles, the size effect on breakage probability, the weakening of particles due to repeated stressing events and the relation between energy and fragment size distribution. At a first stage, the verification of the model has been carried out by comparing results from the analytical model previously fitted to experimental data with simulations of single particle breakage tests. Sensitivity analysis of simulations varying different relevant parameters has also been performed. Afterwards, the simulation model was validated by comparing its results to drop ball test experiments on unconfined particle beds. The good agreement demonstrates the potential of the model to simulate more complex systems in which DEM simulations must include an effective description of breakage. Finally, the model has been used to simulate a laboratory-scale cone crusher and a pilot-scale horizontal shaft impact crusher.

SUMMARY

ACKNOWLEDGEMENTS iv

LIST OF FIGURES x

LIST OF TABLES xvi

1. INTRODUCTION 1

2. OBJECTIVE 4

3. LITERATURE REVIEW 5

  3.1. Industrial comminution and particle breakage 5

    3.1.1. Crushing 7

    3.1.2. Grinding 10

  3.2. Breakage modeling 12

    3.2.1. Breakage characterization tests of individual particles 13

      3.2.1.1. Single impact tests 14

      3.2.1.2. Double impact tests 16

      3.2.1.3. Limitations of characterization tests 19

    3.2.2. Breakage tests of beds of particles 21

  3.3. UFRJ model 22

    3.3.1. Fracture energy distribution and breakage probability 25

    3.3.2. Damage mechanics 27

    3.3.3. Particle size distribution 32

  3.4. Discrete element method 36

    3.4.1. Contact modeling in DEM 38

      3.4.1.1. Hysteretic linear spring model 38

      3.4.1.2. Linear spring Coulomb limit model 40

    3.4.2. Breakage modeling in DEM 41

      3.4.2.1. Breakage modeling adopting bonding elements 42

      3.4.2.2. Breakage modeling adopting particle replacement scheme 46

    3.4.3. Rocky DEM 49

      3.4.3.1. Ab-t_{10} model 50

3.4.3.2. Tavares breakage model 51

3.4.3.3. Laguerre-Voronoi tessellation 56

4. METHODOLOGY 59

4.1. Software and hardware 59

4.2. Materials 60

4.3. Simulation modeling 63

4.3.1. Verification stage 63

4.3.1.1. Single and double impact tests 64

4.3.2. Validation stage 65

4.3.2.1. Unconfined particle bed breakage tests 66

4.3.2.2. Laboratory cone crusher 67

4.3.3. Application stage 71

4.3.3.1. Pilot horizontal shaft impact crusher 71

4.3.4. Contact modeling 72

4.3.5. Particle parameters 73

4.3.6. Particle shape 74

4.3.7. Rocky DEM solver parameters 75

5. RESULTS AND DISCUSSION 77

5.1. Verification stage 77

5.1.1. Simulations of breakage probability 77

5.1.2. Simulations of particle fragmentation 79

5.1.3. Simulation of damage accumulation 84

5.1.4. Effects of minimum size variation 86

5.1.5. Effects of Young’s modulus variation 89

5.1.6. Effect of restitution coefficient variation 92

5.2. Validation stage 92

5.2.1. Unconfined particle bed breakage tests 92

5.2.2. Laboratory cone crusher 101

5.3. Application stage 107

5.3.1. Pilot horizontal shaft impact crusher 107

6. CONCLUSIONS 111

7. FUTURE WORK 113

BIBLIOGRAPHY 114

LIST OF FIGURES

Figure 3.1 - Stress application methods in comminution equipment. Citing the load application on individual particles (a) and particle beds (b), particle propelling against a surface (c) or another particle (d), use of cutting equipment (e), application of shear (f), application of non-mechanical energy such as high voltage pulses, microwave or heat (g) and abrasion due to surface breakage (h) 6
Figure 3.2 - Tensile stresses at the tip of a crack caused by compression (RUMPF, 1973) 7
Figure 3.3 - Schematic diagram of a jaw crusher (left) and a gyratory crusher (right) indicating important components of their operation (Adapted from GUPTA & YAN, 2016) 8
Figure 3.4 - Schematic view of the crushing zone of the cone crusher (KING, 2001) 9
Figure 3.5 - Cross-section of an operating VSI crusher (CEPURITIS *et al.*, 2015) 10
Figure 3.6 - Motion of charge inside a tumbling mill (WILLS & NAPIER-MUNN, 2006) 11
Figure 3.7 - Breakage mechanisms classified according to the applied energy level (Adapted from CUNHA, 2014) 14
Figure 3.8 - Single impact tests used for ore characterization (Adapted from TAVARES, 2007) 15
Figure 3.9 - Double impact tests used for ore characterization (Adapted from TAVARES, 2007) 17
Figure 3.10 - Force-time profile measured in the ILC resulting from impact of a 2.4 mm copper ore particle in the ILC (TAVARES, 2007) 18
Figure 3.11 - Breakage probability distribution of 12.5 mm fired clay pellets under different stressing methods (TAVARES, 2007) 19
Figure 3.12 - Effect of loading geometry on breakage of 2.00-2.80 mm apatite particles at 874 J/kg (left) and 6488 J/kg impact energy (right) (TAVARES, 2007) 20
Figure 3.13 - Energy transfer efficiency from the ball to breakage energy for different materials in the ILC as a function of relative impact energy (TAVARES, 2007) 21
Figure 3.14 - Snapshots from experiment of an impact of 5 layer particle bed with an 88 mm steel ball with impact energy of 3.05 J (JIMÉNEZ-HERRERA *et al.*, 2018) 22
Figure 3.15 - General scheme of the operating principles of the UFRJ model as originally proposed to ball mills (Adapted from CARVALHO, 2009) 23
Figure 3.16 – Particle fracture energy distributions of 2.0 – 2.8 mm particles of various minerals. Lines represent data from equation (3.7) (TAVARES & KING, 1998)........... 26
Figure 3.17 - Variation of mean specific particle fracture energy with particle size for different materials. Lines represent fitting of equation (3.9) to data (TAVARES, 2007) 27

Figure 3.18 - Particle weakening due to accrual of damage in unsuccessful loading events (TAVARES, 2009) 28
Figure 3.19 - Predicted force-deformation profiles resulting from repeated loading of a marble particle (TAVARES & KING, 2002) 29
Figure 3.20 - Experimental (triangles) and predicted (lines) cumulative percentage broken after repeated impacts at two impact energies of bauxite ore of 45.0 – 37.5 mm (TAVARES, 2009) 32
Figure 3.21 – Relationship between $t10$ and stressing intensity for various materials (TAVARES, 2004) 33
Figure 3.22 - Appearance function for a sample of copper ore. Lines represent fitting with splines (TAVARES, 2007) 34
Figure 3.23 - Relation between measured $t10$ values and fitted results using equation (3.23) for a copper ore sample (CARVALHO & TAVARES, 2011) 35
Figure 3.24 - Flowchart indicating the working principles of a DEM algorithm (Adapted from SEVILLE & WU, 2016) 37
Figure 3.25 - Typical loading cycle in a force-deformation diagram comparing with the overlap between two particles in the hysteretic linear spring model (ROCKY DEM, 2018) 39
Figure 3.26 - Cluster of spherical particles representing a 3D scanned particle with realistic shape (QUIST & EVERTSSON, 2016) 42
Figure 3.27 - Schematic representation of two particles bonded together with a cylindrical beam leading to different load modes (Adapted from POTYONDY & CUNDALL, 2004) 43
Figure 3.28 - Illustration of particle breakage in two dimensions adopting polyhedral particles with bonding joints between the elements (JIMÉNEZ-HERRERA *et al.*, 2018) 44
Figure 3.29 - Snapshots of a single particle impacting a surface using the model by OROZCO *et al.* (2019) 46
Figure 3.30 - Illustration of the particle replacement model (JIMÉNEZ-HERRERA *et al.*, 2018) 47
Figure 3.31 - Packing of progeny particles occupying the volume of a superquadric particle (DELANEY *et al.*, 2010) 48
Figure 3.32 - Comparison between the analytical solutions of equations (3.23) and (3.43) for a population of 5,000 copper ore particles of 5.5 mm in size, presenting the tendency of overestimation when adopting the specific fracture energy of each particle to calculate the values of $t10$ 53
Figure 3.33 - Calculation cycle of the Tavares breakage model 54

Figure 3.34 - Evolution of particle fragmentation in a drop weight test simulated in Rocky DEM, indicating that fine fragments are generated due to multiple rebreakage of particles being the time elapsed between the first and the last frame of 2e-03 s 55

Figure 3.35 - Packing of spheres of different radii (left) and the Laguerre-Voronoi tessellation (right) (FALCO *et al.*, 2017) 58

Figure 4.1 - Comparison of primary fragment size distributions given by the model for the four materials studied 61

Figure 4.2 - Variation of median mass-specific fracture energies for the materials as a function of particle size 62

Figure 4.3 - Comparison between the predicted values of $t10$ using the original equation of the UFRJ model for a value of b' of 0.0294 and different values of b' using the adapted equation for a discrete approach in Rocky DEM 63

Figure 4.4 - Simulation setup for drop weight tests (left) and single impact tests (right). Particles are shown in red 64

Figure 4.5 - Simulation setup for the damage accumulation test consisting of 20 consecutive drops of same height (left) and frames from different impacts (right). The corresponding impact number is presented in each frame 65

Figure 4.6 - Exemplification of the setups adopted in experiments (left) and simulations (right) 66

Figure 4.7 - Different bed arrangements of copper ore particles of 6.1 mm in size tested in unconfined bed breakage tests 67

Figure 4.8 - Laboratory-scale cone crusher used in experiments (left) (MAGALHÃES & TAVARES, 2014) and modeled version adopted in simulations (right) 68

Figure 4.9 - Cutaway view of the laboratory-scale cone crusher adopted in simulations of the validation stage 68

Figure 4.10 - Horizontal motion of the cone in simulations in parallel view. The red lines represents the maximum displacements measured in laboratory cone crusher (top view of the cone) 69

Figure 4.11 - Illustration of a parallel view of the closed-sized setting of 5.0 mm, represented by the internal red circle (left) and the open-sized setting of 5.5 mm, represented by the external red circle (right) 70

Figure 4.12 - Modeled horizontal shaft impact crusher used in simulations. The black arrow indicates the direction of rotation 72

Figure 4.13 - Particle shape adopted throughout the simulations 74

Figure 4.14 - Additional particle shapes adopted for crushing simulations 75

Figure 5.1 - Comparison between the modeled (lines) and simulated (symbols) breakage probabilities for drop weight tests and single impact tests of 5.5 mm particles of different materials 78
Figure 5.2 - Comparison between the modeled (lines) and simulated (symbols) breakage probabilities for drop weight tests and single impact tests of copper ore particles of different sizes (triangles are single impact and squares, drop weight test simulations) 79
Figure 5.3 - Comparison between the modeled (lines) and simulated (symbols) $t4$ values for drop weight tests of 5.5 mm particles (solid lines and hollow symbols) and 28.9 mm particles (dashed lines and filled symbols) of copper ore 80
Figure 5.4 - Comparison between the modeled (lines) and simulated (symbols) $t2$ values for drop weight tests of 5.5 mm particles (solid lines and hollow symbols) and 28.9 mm particles (dashed lines and filled symbols) of copper ore 80
Figure 5.5 – Comparison between the relative impact energy and the fragmentation data for drop weight tests of 5.5 mm particles and 28.9 mm particles of copper ore 81
Figure 5.6 - Comparison between the modeled (lines) and simulated (symbols) $t4$ values for drop weight tests of 5.5 mm particles of granulite, limestone #1 and limestone #2 82
Figure 5.7 - Comparison between the modeled (lines) and simulated (symbols) $t2$ values for drop weight tests of 5.5 mm particles of granulite, limestone #1 and limestone #2 83
Figure 5.8 - Comparison between modeled (symbols) and simulated (lines) progeny size distributions for drop weight tests of 5.5 mm limestone #2 particles for different impact energies 84
Figure 5.9 - Comparison between modeled (symbols) and simulated (lines) progeny size distributions for drop weight tests of 28.9 mm copper ore particles for different impact energies 84
Figure 5.10 - Comparison between the modeled (lines) and simulated (symbols) values of cumulative broken for consecutives single impacts. The solid lines are the expected values for cumulative broken and the dashed line the values of cumulative broken for the adjusted impact energy to match the breakage probability 85
Figure 5.11 - Comparison between the modeled (lines) and simulated (symbols) values of cumulative broken of limestone #1 particles for consecutives single impacts of 10.5 J/kg and different values of γ. 86
Figure 5.12 - Comparison between the modeled (line) and simulated (symbols) breakage probabilities for drop weight tests of 28.9 mm particles of copper ore for different minimum particle sizes 87
Figure 5.13 - Comparison between modeled (symbols) and simulated (lines) progeny size distributions for drop weight tests of 28.9 mm copper ore particles for different minimum particle size adopting an impact energy of 201 J/kg 88

Figure 5.14 - Comparison between modeled (symbols) and simulated (lines) progeny size distributions for drop weight tests of 28.9 mm copper ore particles for different minimum particle size adopting an impact energy of 1089 J/kg.................................. 89

Figure 5.15 - Comparison between the modeled (lines) and simulated (symbols) breakage probabilities for drop weight tests and single impact tests of 5.5 mm particles of copper ore and limestone #1 adopting a Young's modulus of 1e+08 N/m² for ore particles and 1e+09 N/m² for the steel 90

Figure 5.16 - Comparison between the modeled (lines) and simulated (symbols) breakage probabilities for drop weight tests and single impact tests of 5.5 mm particles of copper ore and limestone #1 adopting a Young's modulus of 5e+08 N/m² for ore particles and 5e+09 N/m² for the steel 91

Figure 5.17 - Comparison between the modeled (line) and simulated (symbols) breakage probabilities for single impact tests of 5.5 mm particles of copper ore for different restitution coefficients 92

Figure 5.18 - Comparison of the broken mass of particles (passing a 4.75 mm sieve) in experiments and simulations of impact with an 88 mm diameter ball in beds under different arrangements for the materials studied at 3.05 J.. 94

Figure 5.19 - Comparison of cutaway views of the 5-layer beds of limestone #1 (left) and copper ore (right) particles from impacts at 3.05 J with an 88 mm diameter ball at the exact time elapsed from simulation. Particles colored as a function of their size......... 95

Figure 5.20 - Distance between the bottom of the dropping ball and the anvil during impact test of the 88 mm ball against a five-layer copper ore bed for energies of 3.05 J 96

Figure 5.21 - Comparison between size distributions of the bed material after impact at 3.05 J with an 88 mm diameter steel ball for copper ore particles. Symbols represent experimental data and lines simulations... 97

Figure 5.22 - Comparison between size distributions of the bed material after impact at 3.05 J with an 88 mm diameter steel ball for granulite particles. Symbols represent experimental data and lines simulations... 97

Figure 5.23 - Comparison between size distributions of the bed material after impact at 3.05 J with an 88 mm diameter steel ball for limestone #1 particles. Symbols represent experimental data and lines simulations... 98

Figure 5.24 - Comparison of the broken mass of particles (passing a 4.75 mm sieve) in experiments and simulations of impact with an 88 mm diameter ball in a monolayer bed of 6.1 mm copper ore particles... 99

Figure 5.25 - Comparison between the size distributions of the material from impact of an 88 mm diameter ball in a monolayer bed of 6.1 mm copper ore particles at different impact energies 99
Figure 5.26 - Exemplification of the technique adopted to measure the radii of capture of particles in experiments (left) and simulations (right) for an impact of 3.05 J with an 88 mm diameter steel ball on copper ore particles. The capture radii are represented by the circles in both illustrations 100
Figure 5.27 - Comparison of the radii of capture of particles in experiments and simulations as a function of impact energy for an 88 mm diameter steel ball dropping on a monolayer bed of 6.1 mm copper ore particles 101
Figure 5.28 - Frame of a simulation of the laboratory cone crusher with a CSS of 5.0 mm being fed with granulite particles sized from 16 mm to 22.4 mm 102
Figure 5.29 - Simulated discharge rate in crushing tests involving copper ore, granulite and limestone #1 particles. Throughput analysis starts at 3 seconds of simulation ... 103
Figure 5.30 - Simulated power draw of crushing tests involving copper ore, granulite and limestone #1 particles 104
Figure 5.31 - Illustration of material leaving the crusher without undergoing further rebreakage due to the elongated shape of the fragments 106
Figure 5.32 - Comparison between simulated (left) and experimental (right) particle sizes distributions of crushing tests involving copper ore, granulite and limestone #1 particles 106
Figure 5.33 - Distribution of breakage probability for copper ore and limestone #1 particles of 16 mm to 22.4 mm in size. Vertical lines indicate the impact energy of a collision between a particle and the blow bar for the different rotational velocities tested 108
Figure 5.34 - Feed and product size distributions from simulation using a HSI crusher. Particle size distributions of the blended feed (black dashed line) and product (black continuous line) for a rotational velocity of 1089 rpm. Blue and red continuous lines represent the individual analysis of the copper ore and the limestone products that composes the blended product, respectively 109
Figure 5.35 - Feed and product size distributions from simulation using a HSI crusher. Particle size distributions of the blended feed (black dashed line) and product (black continuous line) for a rotational velocity of 281 rpm. Blue and red continuous lines represent the individual analysis of the copper ore and the limestone products that composes the blended product, respectively 110

LIST OF TABLES

Table 3.1 - Comparison between the main DEM works adopting breakage on comminution equipment.. 56
Table 4.1 - Configuration of the workstation used to perform the simulations............. 59
Table 4.2 - Summary of particles breakage parameters of the Tavares breakage model adopted in the simulations 60
Table 4.3 - Mass parameters of the cone geometry 71
Table 4.4 - Contact parameters adopted in the simulations to verify the Tavares breakage model... 73
Table 4.5 - Particles parameters adopted in the simulations to verify the Tavares breakage model 73
Table 4.6 - Parameters adopted to model the particle shape used in simulations 74
Table 4.7 - Additional particle shapes adopted in crushing simulations....................... 75
Table 5.1 - Timestep duration for each simulation performed during the verification stage 77
Table 5.2 - Predicted and adjusted values of specific impact energy and breakage probability for copper ore and limestone #1 particles subjected to repeated impacts of the same magnitude 85
Table 5.3 - Timestep duration for each simulation performed varying the Young’s modulus of the materials.. 90
Table 5.4 - Timestep duration for simulations of unconfined particle bed breakage 93
Table 5.5 - Timestep duration for cone crusher simulations 103
Table 5.6 - Comparison between simulated and experimental results for throughput, power draw and specific energy of cone crusher tests 105
Table 5.7 - Composition of the products finer and coarser than 16.0 mm based on the proportion of broken mass for a rotational velocity of 281 rpm 110

1. INTRODUCTION

Comminution is one of the most important processes in the minerals industry, especially owing to its high cost. The understanding of this stage comprises a vital part of the researchers' role in ensuring the feasibility of the industry, however the advances arising from research need to be applied efficiently in industrial practice. The correct implementation of robust models in simulation software is one important part of this process of interaction between industry and research and development.

It is currently estimated that 1.8% of world energy is consumed only in the comminution process (NAPIER-MUNN, 2015) and this stage accounts for approximately 50% of the energy consumption in an industrial processing plant (JESWIET & SZEKERES, 2016). According to NAPIER-MUNN *et al.* (1996), growth in the efficiency of comminution may occur through changes in the technologies adopted or improvements on operational practice of existing technologies. Both options aim to optimize the process performance, ensuring better energy utilization of the equipment and, consequently, reducing operating costs, increasing production and improving the efficiency of downstream processes.

The understanding of the fundamentals involving the fracture of ore particles is indispensable for the development of new techniques that allow increasing the efficiency of the comminution process. However, comminution is a complex process which, in spite of the efforts made throughout the last century, has not yet been adequately described through a quantitative theoretical treatment (TAVARES & KING, 1998). Currently, there are no models capable of describing particle breakage based on the physical properties of particulate materials, such as their composition, specific gravity and crack size distribution, among others. Yet, particle properties, such as the breakage probability of a population (TAVARES & KING, 1998, VOGEL & PEUKERT, 2003), damage accrual by impacts of lower magnitude than that necessary to lead particles to breakage (TAVARES & KING, 2002) and particles fragmentation based on the input energy (SHI & KOJOVIC, 2007, NAPIER-MUNN *et al.*, 1996, TAVARES, 2009) have been successfully used to characterize ore particles.

Most of the breakage models that exist today are calibrated from data obtained experimentally to represent the real behavior of particles. However, the exclusive application of these models is not able to describe quantitatively the complexity of the breakage phenomena in a particulate system due to the large number of interactions between particles of different characteristics that are subjected to the most varied types of stresses during their processing in a comminution device. Currently, the adoption of robust numerical methods and computational simulation make it possible to deal with several variables that are associated to a particle stream.

The use of computer simulations as an alternative to solve problems whose analytical solutions are unavailable started at the end of the first half of the twentieth century with the advent of computational techniques that were robust enough to perform small calculations (ECKHARDT, 1987). Since then, computational models have been widely used in science for the proper understanding of processes and for the development of more efficient equipment. The main benefits of these tools are the reduction of costs and risks of new projects by reducing the need for prototyping and testing.

The discrete element method (DEM) (CUNDALL & STRACK, 1979) consists of an important tool for the understanding of several equipment and processes in a wide range of areas. In the mineral processing area, DEM allowed for better understanding of internal dynamics on crushers and mills, providing important information regarding particle flow, distribution of collision energies, rate of collisions, residence time and so on (CLEARY, 1998, WILLS & NAPIER-MUNN, 2006, WEERASEKARA *et al.*, 2013). Due to its capability of reproducing the behavior of particulate flow, DEM has become an outstanding technique in the development of mechanistic models (WEERASEKARA *et al.*, 2013, TAVARES, 2017), overcoming the limitation of models that were developed in the past that were dedicated to specific comminution devices and scenarios.

Yet, the discrete element method faces several challenges and restrictions to represent breakage of particles (JIMÉNEZ-HERRERA *et al.*, 2018). In most of these simulations, breakage is often left to a post-processing stage using the information collected from the simulations or even altogether disregarded. However, a proper breakage description is of key importance for the understanding of several types of crushers and mills in which particle flow and particle size reduction cannot be decoupled. Different approaches have been adopted in recent years to overcome this limitation, most of them by representing particles as a cluster of spherical (POTYONDY & CUNDALL, 2004) or polyhedral (POTAPOV & CAMPBELL, 1994) elements bonded together or by replacing the original particle by a set of progeny particles (CLEARY, 2001, POTAPOV *et al.*, 2007). These methodologies, however, are only valid in combination of models that are able to properly represent particle breakage. The approaches adopted so far present several limitations regarding the correct description of the breakage phenomena and the necessary computational power to perform it.

A useful breakage description in DEM simulations must be supported by models that are able to describe the phenomena numerically without the need for complex calibration tests. The Tavares breakage model comprises a series of equations proposed by TAVARES (2004, 2009) and TAVARES & KING (1998, 2002) to address important characteristics of particle breakage based on the dissipated energy in each collision event, and therefore, decoupling dominant mechanisms involved in the comminution process. The model covers important rock behavior, such as the variation of particles' fracture energy within particles of same size and different sizes and rock weakening due to damage accumulation. The Tavares breakage model has been firstly introduced without validation in the version 4.1 of the commercial software Rocky DEM (ROCKY DEM, 2018).

The equations that make up the Tavares breakage model are derived from the UFRJ mill model, a model that has been successfully used to address particle breakage in mills as a post-processing stage (TAVARES & CARVALHO, 2009, CARVALHO & TAVARES, 2011, 2013), but of straight-forward implementation on a DEM platform to mimic breakage in real time during simulations. The use of the commercial software Rocky DEM to reproduce particle breakage also grants the advantages of mass and volume conservation after a breakage event as a result of adopting polyhedrons to represent irregular particle shapes.

The present work shows the implementation of the Tavares breakage model in Rocky DEM and its verification on the basis of single particle impact tests widely used in the minerals industry to describe ore behavior. Hereafter, the model is tested in different size reduction systems for validation purposes and to verify the feasibility of its use to represent particle breakage in a DEM environment.

2. OBJECTIVE

The objective of this research is to introduce and test the Tavares Breakage Model implemented in the commercial platform of discrete element method (DEM) Rocky DEM. The work aims to implement the equations of the model in the simulation platform, providing the necessary changes to guarantee the correct description of particle breakage. On the sequence, the present work targets the verification of the breakage model using individual particles characterization tests adopted to describe ore behavior in the mineral industry and, lastly, the work aims to validate the model on simulations of varied comminution systems ranging from laboratory scale to pilot scale equipment.

3. LITERATURE REVIEW

3.1. Industrial comminution and particle breakage

Comminution is the fragmentation process of coarse particles into finer particles. Its use is not restricted to the minerals industry, in which it is widely adopted in the liberation of valuable minerals from gangue and to facilitate the handling of exploited material to processing plants (WILLS & NAPIER-MUNN, 2006). Comminution plays an important role in a range of areas, such as the cement industry to prepare raw materials and clinker, in the aggregate industry to produce fine and coarse aggregates in a given size and shape requirements and in the pharmaceutical and food industry to increase the contact surface of the material, improving its chemical reactivity (WEERASEKARA *et al.*, 2013).

Different comminution devices are used depending on the size of the particle to be comminuted and the desired product. Usually, crushing is the first of the comminution processes and is used downstream from rock blasting in the mine. Several types of crushers are used in multiple stages, such as roll crushers, jaw crushers, gyratory crushers, cone crushers or impact crushers. The crushing stage often has the primary role of preparing the feed for the grinding stage, which will carry out particle size reduction up to the desired fineness and degree of liberation using ball mills, rod mills, autogenous and semi-autogenous mills, among others.

Industrial comminution is typically inefficient in relation to energy use, since it consumes significantly more energy than what is required to perform particle breakage (TAVARES, 2004). Several studies have attempted to quantify the inefficiency of this process by relating the energy required for individual breakage of particles with the energy consumed in the grinding and crushing process in attempts to propose solutions to increase energy efficiency in comminution (SCHÖNERT, 1972, PAUW & MARÉ, 1988, MORRELL *et al.*, 1992, FUERSTENAU & ABOUZEID, 2002, TAVARES, 2004).

Particle size reduction is achieved using different force application mechanisms on comminution devices, which one presenting its own characteristics regarding breakage mode and progeny size distribution. Figure 3.1 illustrates the most common modes of stressing application in equipment that are either adopted in the mineral industry or that are object of study.

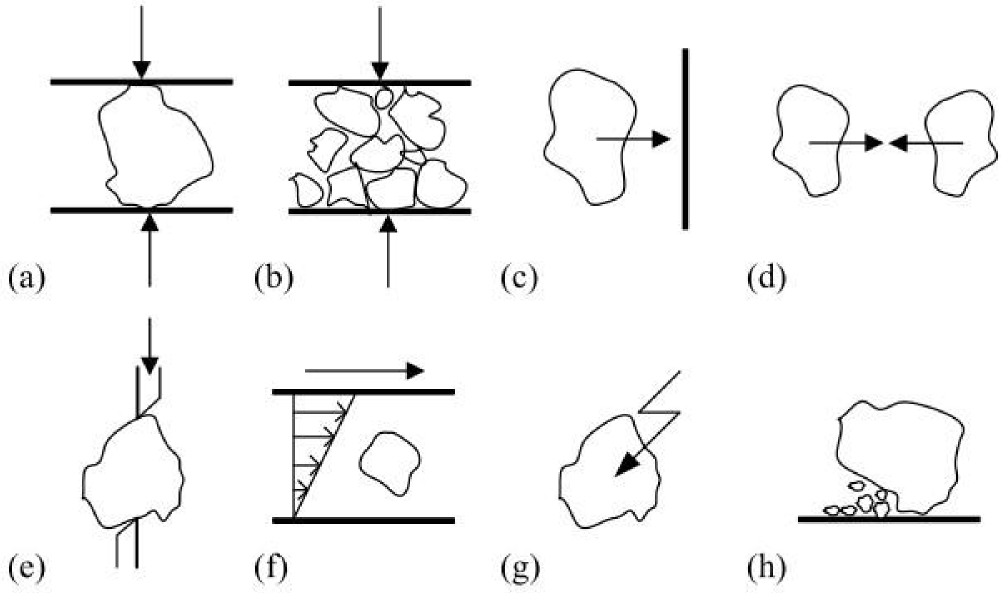

Figure 3.1 - Stress application methods in comminution equipment. Citing the load application on individual particles (a) and particle beds (b), particle propelling against a surface (c) or another particle (d), use of cutting equipment (e), application of shear (f), application of non-mechanical energy such as high voltage pulses, microwave or heat (g) and abrasion due to surface breakage (h)

Breakage can be described as a series of events regarding microcrack propagation. According to RUMPF (1973) there is a critical stress level in which microcracks start to propagate from points of weakness or flaws in the atomic structure of the material, as shown in Figure 3.2, and before this critical stress, the impact energy is stored as elastic strain energy in the particle. Another assumption that is made is based on Griffith's theory, stating that brittle materials such as rocks contain a distribution of flaws in their internal structure and the number of flaws would be directly related to particle size, since coarser particles could, potentially, contain larger flaws. Therefore, breakage initiation would be favored on coarser particles. The theory that the flaws control particle breakage is reinforced by the evidence observed on finer particles, where there would be a size in which particles would contain no flaws and fracture would be replaced by plastic deformation (NAPIER-MUNN *et al.*, 1996).

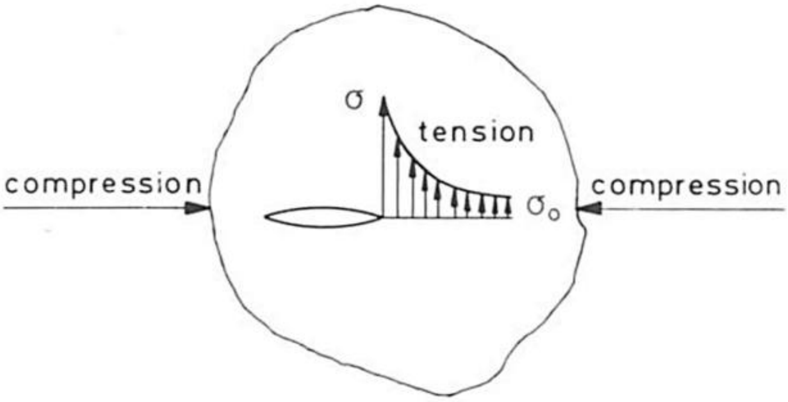

Figure 3.2 - Tensile stresses at the tip of a crack caused by compression (RUMPF, 1973)

These observations indicate that the specific fracture energy used for particle fragmentation is not only the energy needed to break bonds when forming new surfaces, but also involves an activation energy at the crack tip that is converted to heat and can partially alter the atomic structure near the crack (FUERSTENAU & ABOUZEID, 2002). However, the application of this theory to quantify the critical stress necessary to induce particle breakage lies on the need to know, a priori, the size and orientation of cracks within a particle before determining the stresses that might lead to particle fracture.

3.1.1. Crushing

Crushing is the first mechanical stage in the process of comminution. It is usually performed dry, but a crushing plant might include a washing stage if necessary to avoid problems in crushing and screening due to the presence of clay in the mineral body being exploited (WILLS & NAPIER-MUNN, 2006). The crushing process is often carried out in several sequential stages combined with screening processes to ensure recirculation of oversize material and particle classification when necessary. Different types of crushers can be used to promote particle size reduction depending on particle size and the final use of the comminuted material.

Particle size reduction is an important process in the minerals industry and can be used in different roles that will determine the appropriate flowsheet for a plant. According to NAPIER-MUNN *et al.* (1996), the objectives of the crushing process include: maximum size reduction, often as a preparation for a grinding circuit; maximum product of a specified size for aggregates used in civil engineering; top size reduction for material handling and top size control with minimum fines productions for commodities such as iron ore and coal.

Crushers are often classified based on their position on the crushing circuit. Jaw and gyratory crushers are mostly used for primary crushing. They are characterized by their wide gape, narrow discharge size distribution and their capacity to handle large quantities of material (KING, 2001). Due to their simple design, in which particles are only retained within the jaws or inside the crushing chamber while their size is larger than the discharge gap, there is no opportunity for re-breakage of the fragments and maximum particle size and size distribution of the fragments will be governed by the open (OSS) and closed-side settings (CSS). Jaw crushers are able to produce size reduction ratios between 4:1 and 9:1, while gyratory crushers often operate on a range from about 3:1 to 10:1 of size reduction ratio (KING, 2001). Figure 3.3 presents the schematic diagram of jaw and gyratory crushers.

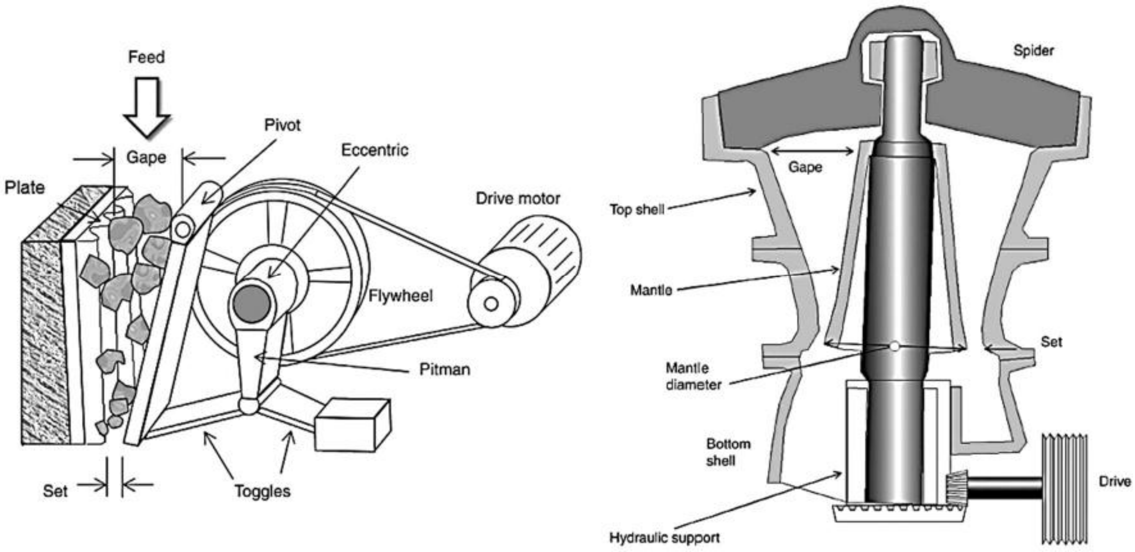

Figure 3.3 - Schematic diagram of a jaw crusher (left) and a gyratory crusher (right) indicating important components of their operation (Adapted from GUPTA & YAN, 2016)

Cone crushers are commonly used in secondary, tertiary and quaternary crushing stages. The main difference between a cone crusher and a gyratory crusher is in the shape of their chamber, presenting parallel surfaces between the cone and the concaves to ensure longer time of particle retention in the crushing chamber and maximize particle size reduction (LUZ *et al.*, 2004). Figure 3.4 illustrates the crushing zone on a cone crusher. Reduction ratios from 6:1 to 8:1 are common for secondary cone crushers and from 4:1 to 6:1 for tertiary and quaternary cone crushers (KING, 2001). Particle size distribution tends to be determined primarily by the CSS since every particle will experience at least one closed-size nip when passing through the crusher.

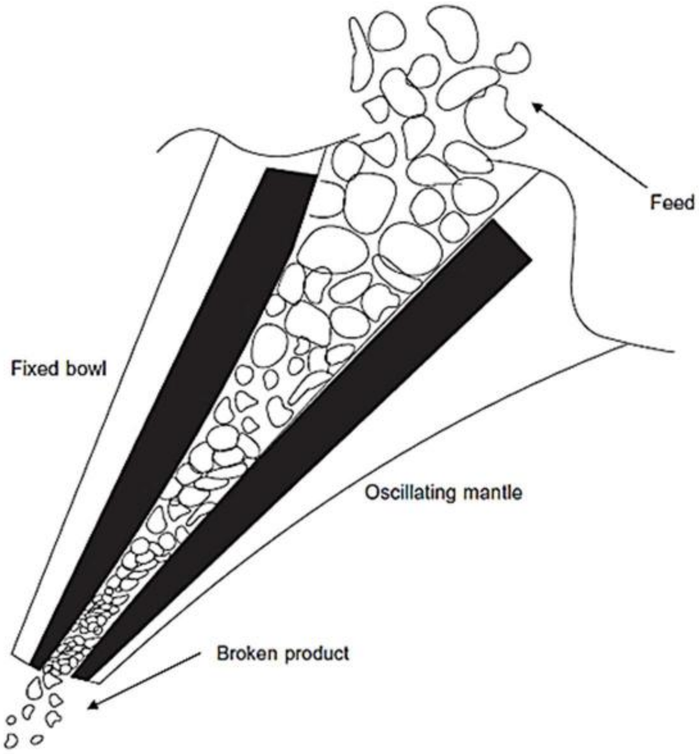

Figure 3.4 - Schematic view of the crushing zone of the cone crusher (KING, 2001)

Impact crushers have reached some popularity on a wide range of applications, in particular in the quarry industry. Since they promote breakage by impact rather than by compression, fracture will leave no residual stresses in the particles, increasing their strength. Impact crushers are also responsible for generating cubic-shaped particles due to abrasion and breakage of elongated particles (WILLS & NAPIER-MUNN, 2006). Vertical shaft impact crushers (VSI) are characterized for being autogenous crushers, using the rock fed into the machine to carry out comminution of the material itself and are generally applied in the last stages of the crushing circuit. They can also have a cascade system, as presented in Figure 3.5, allowing fine-tuning of the final product size distribution and shape and providing extra crushing capacity in the machine. In this case size reduction occurs when the material fed through the center of the rotor is accelerated at high speeds and released onto the material passing outside the rotor as a cascade (LUZ *et al.*, 2004).

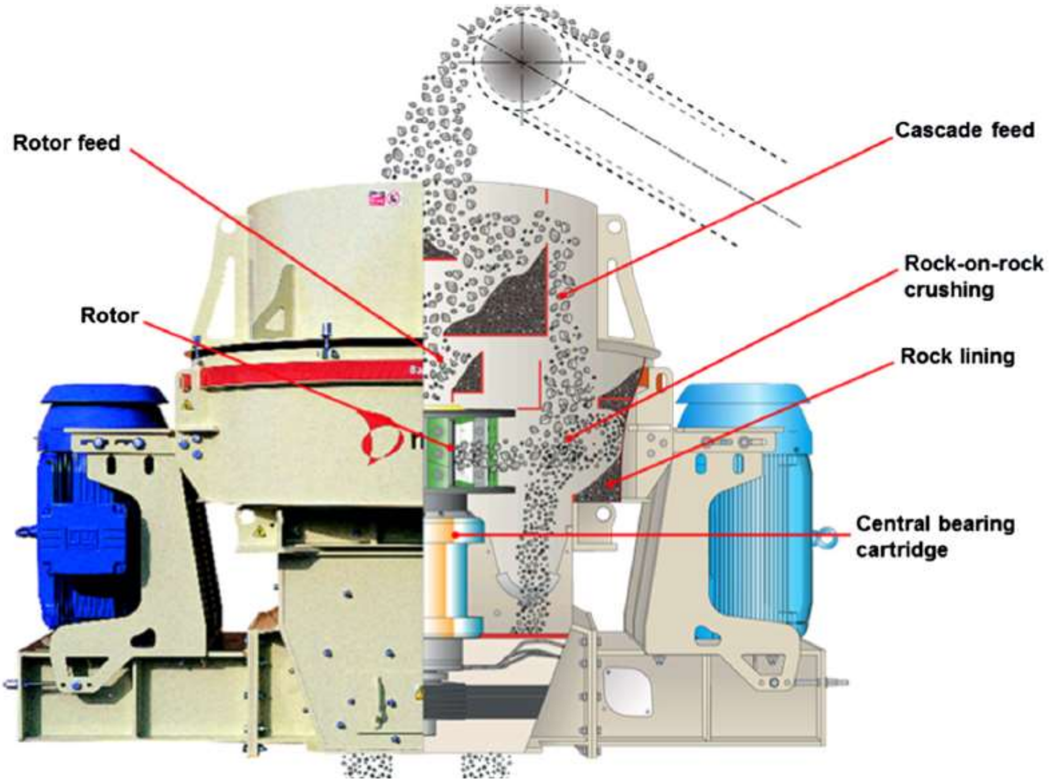

Figure 3.5 - Cross-section of an operating VSI crusher (CEPURITIS *et al.*, 2015)

Other crusher types that are not the main focus of the present work but are widely used in the mineral processing industry include the high-pressure grinding rolls (HPGR) and the hammer crusher (commonly referred to as hammer mill). It is also possible to cite novel crushing techniques, such as the VeRo Liberator® (BORG *et al.*, 2015) and the multi-shaft mill (BRACEY *et al.*, 2016).

3.1.2. Grinding

Grinding is the last stage of comminution processes and it is often needed because the crushing stage cannot provide a product fine enough to reach the appropriate mineral liberation. Particle size reduction in grinding processes is achieved through a combination of impact and abrasion and can be performed either in a dry or wet environment. Industrial grinding machines used in the mineral processing industries are mostly of the tumbling mill type and breakage is induced by the motion between particles and grinding media inside the mills, where the charge is raised against the perimeter of the mill in the direction of motion and cascades to the bottom of the mill (GUPTA & YAN, 2016). Steel rods, balls or rocks themselves can be used to induce breakage inside a tumbling mill. Tumbling mills are employed for coarse-grinding processes, reducing particle size from between 5 to 250 mm to 40 to 300 µm (WILLS & NAPIER-MUNN, 2006).

The motion of particles is determined primarily by the rotation speed of the mill, being also influenced by the conditions of both liners and lifters. Liners are responsible for protecting the outer shell of the mill from wear and lifters are used to prevent slippage between the grinding media and the charge, avoiding the waste of energy and increasing the transmission of energy to the tumbling charge (KING, 2001). Although tumbling mills present great mechanical reliability, they are quite energy inefficient when compared to single-particle breakage. This is due to the fact that it is not possible to accurately control the impact energy applied to each particle and it is neither possible to determine whether the collision will result in particle breakage. Furthermore, most of the energy of the tumbling load is ultimately dissipated as heat and noise (WILLS & NAPIER-MUNN, 2006). Figure 3.6 illustrates the motion of the charge on a tumbling mill where it is possible to identify two different zone where particle size reduction occurs.

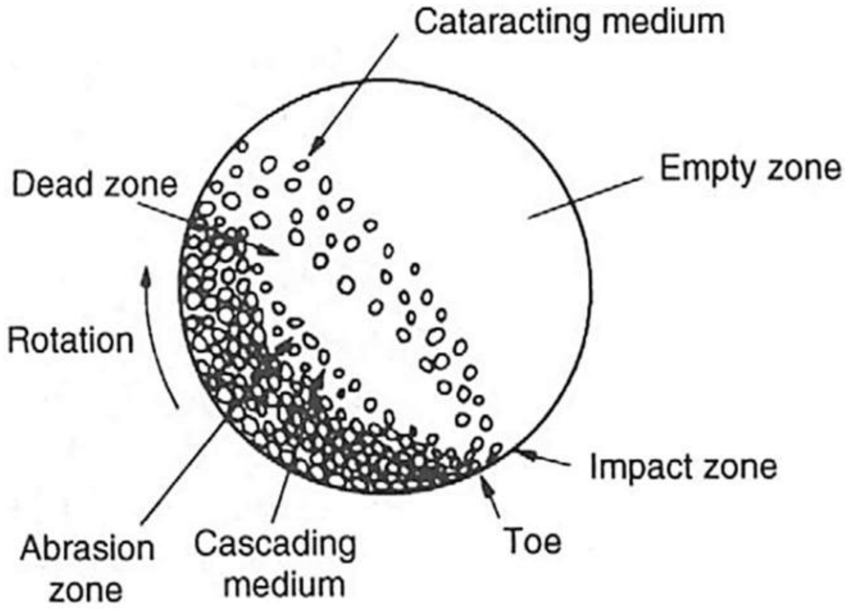

Figure 3.6 - Motion of charge inside a tumbling mill (WILLS & NAPIER-MUNN, 2006)

In ball mills, the grinding environment is not remarkably influenced by the ore characteristics and the sizing of ball mill and its operational conditions will be determined based on particle size. In general, the larger the feed size the larger needs to be the mill diameter. Due to the grater surface area per unit weight of their grinding media, ball mills are more appropriate to fine grinding.

In autogenous mills (AG), coarse ore particles act as grinding media and breakage occurs mainly due to the fall of these particles on a particle bed inside the mill and by attrition between particles of the charge due to the movement of the mill. Semi-autogenous mills (SAG), on the other hand, contain steel grinding media along with autogenous grinding media, to assist in size reduction. The greater benefit of AG/SAG mills is the use of freely available grinding media as replacement of expensive steel balls and rods, responsible for accelerating the wear on liners. However, it is necessary to use competent ores to ensure a large enough amount of lumps inside the mill (GUPTA & YAN, 2016).

3.2. Breakage modeling

A model consists of an equation or set of equations that relate a response of interest to controllable independent variables (WILLS & NAPIER-MUNN, 2006). A mathematical model is capable of representing hypotheses quantitatively and can be verified by comparing actual measurements and modeled data. In a review of the different types of model used in the mineral industry, CONCHA (1995) identified the presence of three major classes of models: empirical, phenomenological and mechanistic models.

Empirical models are the simplest models available, being generated from data based on the observation of unit processes. Since they often rely on linear regression methods to determine process responses, data extrapolation beyond the range of study as well as its adoption in other processes are quite limited (WILLS & NAPIER-MUNN, 2006). Although simplistic, empirical models can be easily developed and are helpful as a basis to generate more complex models, besides allowing a better understanding of the process.

Phenomenological models aim to represent phenomena based on experimental results of the processes, through statistical analysis and without considering the influence of physical principles involved in the process (NAPIER-MUNN *et al.*, 1996). Due to the nature of their development, phenomenological models are characterized by their inability to decouple effects related to the equipment in the response of interest, nevertheless they are robust tools for the representation of a process, allowing some extrapolation. An example of a phenomenological model is the population balance approach, which has been successfully used to simulate comminution processes.

Mechanistic models are models based on Newtonian mechanics by directly considering the behavior of individual parts of the system (NAPIER-MUNN *et al.*, 1996). In the study of comminution, mechanistic models are based on the analysis of the interactions between ore and components of the equipment and, because they rely on more fundamental descriptions, can potentially decouple the contributions of the devices in the calibration of parameters. The level of complexity of mechanistic models is comparatively higher, requiring greater computational power for their application. The mechanistic modeling of comminution processes guarantees the scale-up of the process, allowing the representation of simple tests to industrial-scale equipment.

Due to limited computational power, the first models developed for comminution were purely empirical, correlating the energy consumption to a given reduction ratio (CONCHA, 1995), based on the surface area or the particle size distribution of the product. Further development in the capacity of processing information allowed the development of more complex models, making phenomenological models more popular and, even more recently, supporting the formulation of mechanistic models applied to comminution. The adoption of simulations in DEM made it possible to have access to information that was previously unavailable, allowing the prediction of contacts and the stresses involved. In this scenario, the characterization of breakage became indispensable to determine the behavior of the ore when subjected to different collision energies and types of contacts.

3.2.1. Breakage characterization tests of individual particles

Individual particle characterization tests aim to describe the physical properties of an ore. The development of comminution models has been intrinsically related to the behavior of a material in relation to the applied energy, i.e., its energy-specific breakage function. Individual particle characterization tests have a great advantage in relation to batch grinding tests for the purpose of model calibration, since the latter do not allow decoupling the influence of specific ore properties from the properties of the equipment used, such as its breakage rate and selection function (NAPIER-MUNN *et al.*, 1996).

A large variety of tests is available for individual characterization of particles according to their breakage mode (TAVARES, 2007, MWANGA *et al.*, 2015) since they are subject to different types of stresses in different magnitudes in a comminution equipment, which can lead to their surface breaking or body breakage, as illustrated in Figure 3.7. When particles are subjected to insufficient compressive stresses to promote their fragmentation or shear stresses, surface breakage may occur due to abrasion or chipping. On the other hand, the volumetric or body breakage, characterized by a mass loss of more than 10% of the original mass of the particle (TAVARES, 2007), occurs when the energy applied to the particle is equal to or greater than the energy required to promote its breakage. Impacts involving high energy magnitudes are characterized by transferring some of this energy to the kinetic movement of the fragments and to secondary breakage of the progeny (TAVARES & KING, 1998).

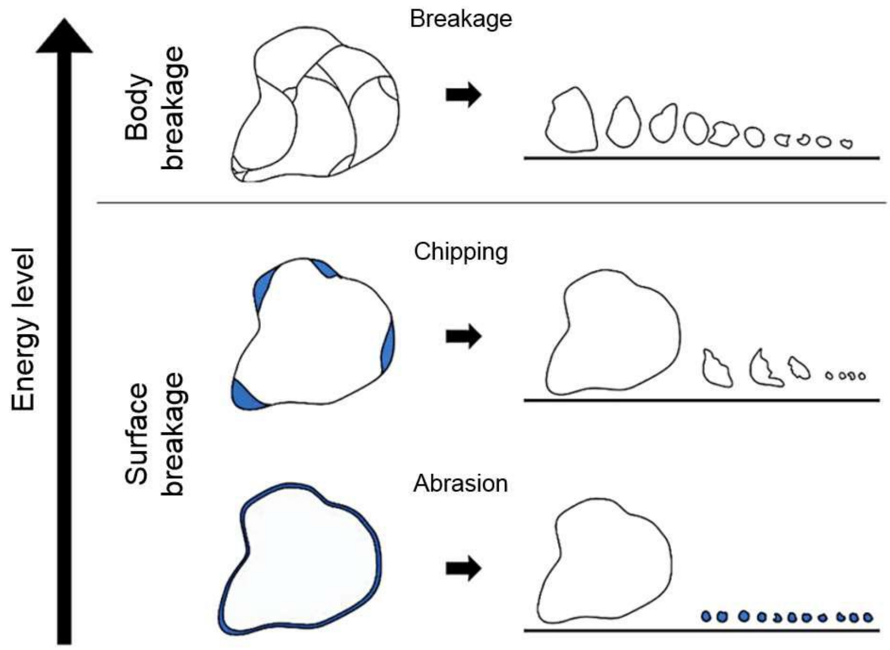

Figure 3.7 - Breakage mechanisms classified according to the applied energy level (Adapted from CUNHA, 2014)

Given their importance in most crushing and grinding processes, greater emphasis is given as follows to tests that involve rapid application of stresses. According to the number of contacts existing during the impact, they can be classified as single or double impacts.

3.2.1.1. Single impact tests

Single impact tests are characterized by the collision between a particle and the surface. The simplest of the tests consists of the free fall of particles on a metallic surface (Figure 3.8A), in which the impact energy can be estimated through the gravitational potential energy equation given by

$$E_{pg} = mgh \tag{3.1}$$

where m is the mass of the particle, g is the gravitational acceleration and h is the distance between the bottom of the particle and the metal surface. However, for drops at high heights, equation (3.1) becomes inaccurate due to air drag and estimation of the velocity of the particle immediately before the contact becomes necessary for the correct calculation of the energy involved in the collision (TAVARES *et al.*, 2018). As such, due to the low velocity at the instant of the impact, the drop test is often used just for coarse particles that present low specific fracture energy.

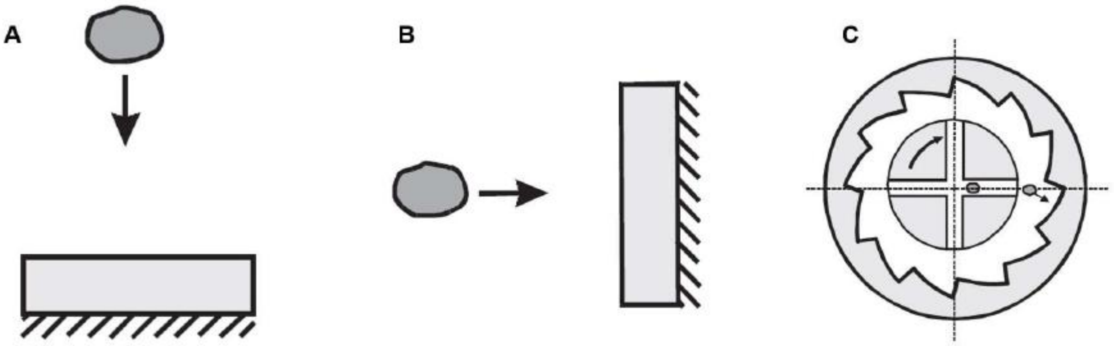

Figure 3.8 - Single impact tests used for ore characterization (Adapted from TAVARES, 2007)

Another single impact test adopted is the propelling of particles against a metallic surface, according to Figure 3.8B. The apparatus allows contacts at higher velocities than the free fall test by adoption of compressed air to propel the particle. The contact impact energy is obtained by the kinetic energy equation, given by

$$E_c = \frac{mv^2}{2} \tag{3.2}$$

where v is the velocity of the particle at the instant before the contact. The determination of particle velocity can be done through high speed cameras during the test.

In addition to direct propelling particles against metal surfaces, another single impact apparatus usually adopted is the projection of particles against anvils induced by the rotation of a rotor, according to Figure 3.8C. Rotary breakers have the advantage of being able to process larger amounts of samples when compared to other characterization tests, obtaining statistically more precise sets of data. The most popular rotary test is the JK Rotary Breakage Tester, or JKRBT (SHI *et al.*, 2009), in which the specific impact energy can be estimated by

$$E_{cs} = 3.046 \text{ x } 10^{-6} C^2 N^2 \left(r + \frac{x}{2}\right)^2 \tag{3.3}$$

where C is a calibration constant for each equipment, N is the rotation frequency in rpm, r is the radius of the rotor and x, the mean particle size. A recent study, however, has shown that significant re-breakage can occur due to the ricocheting of a fraction of fragments against the rotor, leading to biased results when calibrating incremental breakage of low-energy collision (CUNHA *et al.*, 2018).

3.2.1.2. Double impact tests

Double impact tests are characterized by the rapid compression of a particle between two rigid surfaces. The Drop Weight Test (DWT) has been widely used in the minerals industry to characterize breakage of different materials (NAPIER-MUNN *et al.*, 1996). The test consists of the impact of a falling weight from a known height on a particle resting on a metallic surface, according to Figure 3.9A. The variation of the energy applied is carried out by changing the height of fall and/or the mass of the weight, being related to the degree of fragmentation after the impact. The particle size distribution of the product is usually adopted to determine the relationship between the impact energy and the breakage intensity. For the cases where the weight falls freely, the impact energy is obtained based on equation (3.1). However, for the cases where guiding systems are used, equation (3.2) becomes more appropriate because of the friction introduced into the system. For both cases, m corresponds to the weight mass.

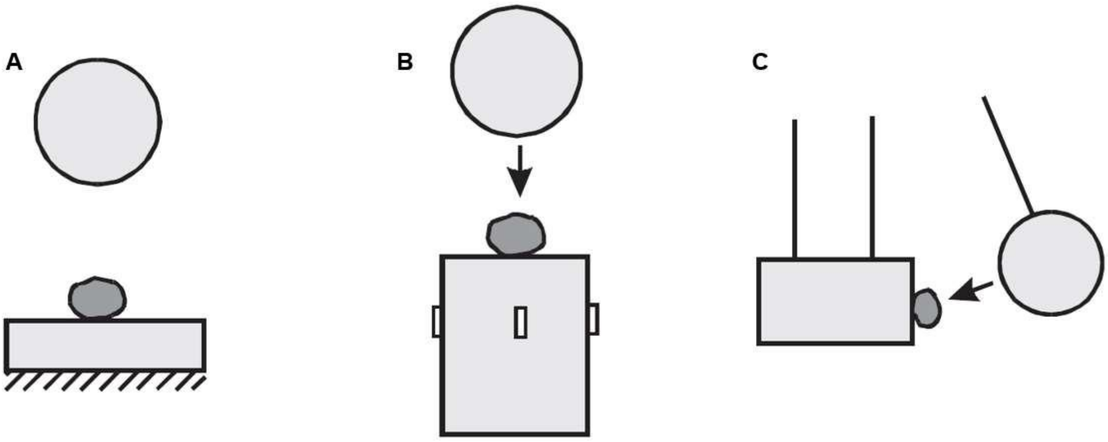

Figure 3.9 - Double impact tests used for ore characterization (Adapted from TAVARES, 2007)

The impact load cell (ILC) is a combination between the traditional drop weight test and the Hopkinson pressure bar (Figure 3.9B). It consists of a long steel rod instrumented with deformation sensors that acquire the force transmitted to the bar during the collision between the falling weight and the particle resting at the end of the bar. The instrumentation of the bar allows the generation of a profile of force along the time. The major variation of the ILC in relation to the standard DWT is the quantification of the energy consumed during the impact, allowing the determination of the specific energy of fracture of the particle. Analysis of the force profile over time also makes it possible to distinguish between primary and secondary particle breakage, as shown in Figure 3.10. Moreover, it allows estimating the stiffness of the particle, represented by the amount of energy accumulated in the particle in the form of deformation before the fracture (TAVARES & KING, 1998).

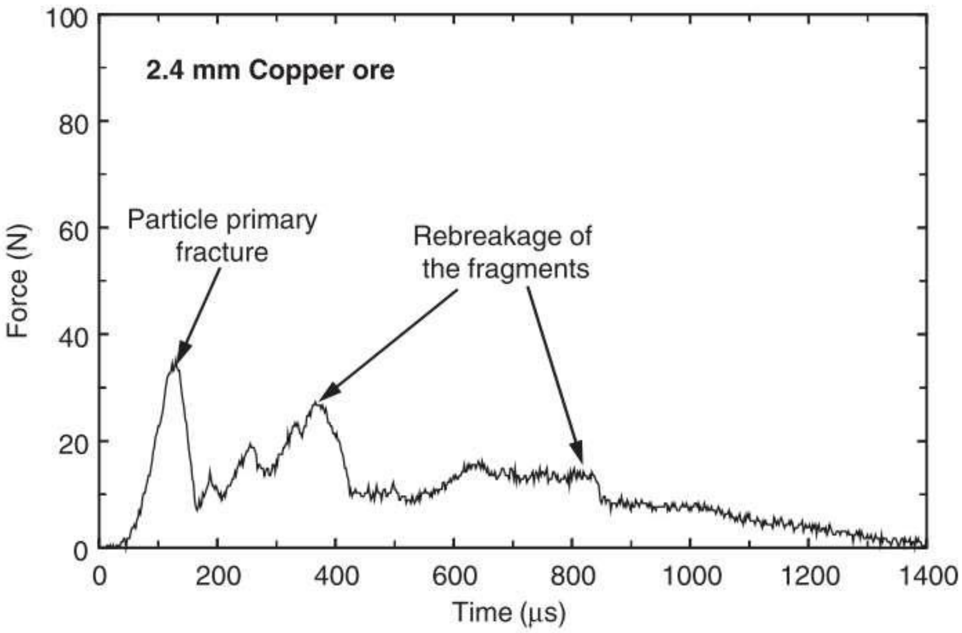

Figure 3.10 - Force-time profile measured in the ILC resulting from impact of a 2.4 mm copper ore particle in the ILC (TAVARES, 2007)

The drop weight test, standardized by the Jullius Kruttschnitt Mineral Research Centre (JKMRC), was developed to replace pendulum tests for assessing impact breakage characteristics of ores (NAPIER-MUNN *et al.*, 1996), even though tests using pendulums exhibit similar ability regarding easiness of use and variation of impact energies. Modifications made to the test made it more robust, allowing the energy consumed in the impact to be obtained. The configuration of the test presented in Figure 3.9C allows for appropriate monitoring of the energy absorbed by the pendulum and the residual energy of the spherical pendulum, making it possible to estimate the specific energy of comminution using the equation:

$$E_c = E_i - E_t - E_r \tag{3.4}$$

where E_c is the consumed energy, E_i is the energy applied to the particle, E_t is the energy transmitted to the resting pendulum and E_r, the residual energy of the spherical pendulum. It should be noted that the comminution energy established by equation (3.4) also considers the energies dissipated during impact in the form of heat and sound (NAPIER-MUNN *et al.*, 1996). Although the pendulum test presents an easy execution, it has limitations on the applied energy, besides a certain inaccuracy in the calculation of the energy necessary for breakage.

3.2.1.3. Limitations of characterization tests

Although compressive impact tests are widely used to determine ore characteristics, some intrinsic limitations concerning their use exist. The behavior of ores when subjected to impacts of different types and magnitudes is not fully predictable and the correct choice of characterization tests based on the purpose of their use is necessary. The work of TAVARES (2007) summarizes the main differences between breakage tests. Figure 3.11 illustrates the breakage probability distributions for single and double impact tests, comparing them to slow compression tests. It is possible to observe that the breakage probability distribution is strongly influenced by the stressing method adopted.

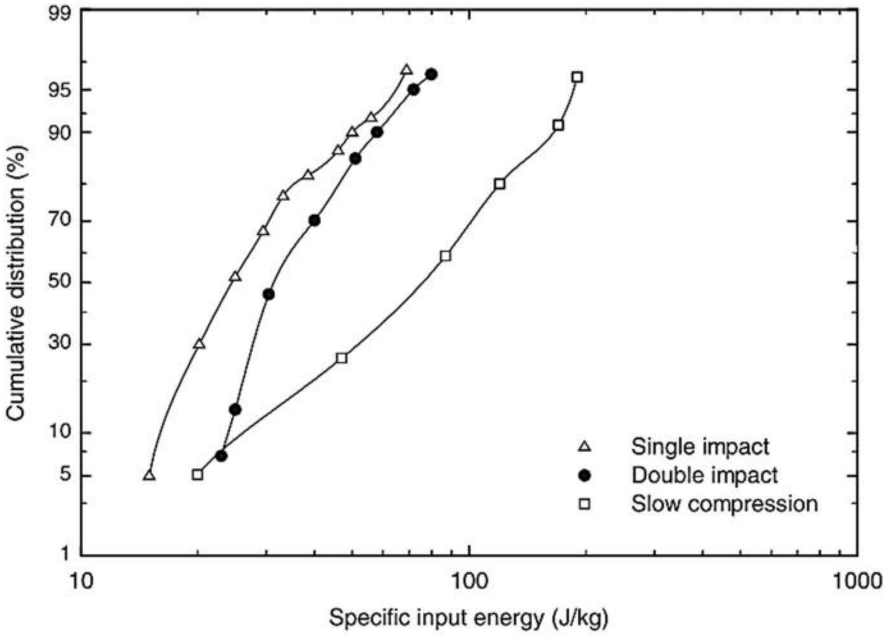

Figure 3.11 - Breakage probability distribution of 12.5 mm fired clay pellets under different stressing methods (TAVARES, 2007)

Furthermore, the geometry of the striker adopted to apply energy to an ore particle also influences the progeny size distribution. This effect can be intensified based on the magnitude of energy input. Figure 3.12 illustrates the differences of particle size distributions of fragments based on the geometry of the striker and the anvil for the same type of ore and different impact energies. The reason for the larger discrepancy at higher energies is due to the availability of remaining energy after the first breakage event. The narrow size distribution with smaller proportion of fines of the flat-flat surfaces loading is a consequence of coarse particles being trapped between the geometries and subsequently selected for further re-breakage whereas in the ball-ball loading the fragments will escape laterally but the high concentration of energy will result in the generation of a large proportion of fines. The same behavior cannot be observed on low impact energies due to the amount of remaining energy after the primary breakage being insufficient to promote further breakage (TAVARES, 2007).

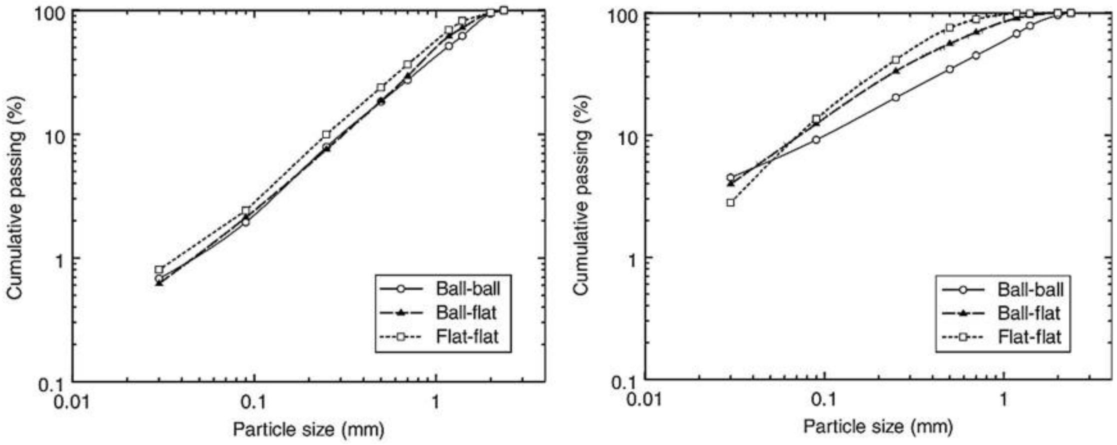

Figure 3.12 - Effect of loading geometry on breakage of 2.00-2.80 mm apatite particles at 874 J/kg (left) and 6488 J/kg impact energy (right) (TAVARES, 2007)

More than being just related to how the characterization test is performed, the ore properties also have a significant effect on the results of breakage tests. The energy transfer efficiency can be successfully measured based on the energy that is effectively converted into strain energy using an impact load cell. Highly brittle material tends to have lower efficiency due to fragments being ejected at high velocities outside the crushing zone, generating less re-breakage and dissipating energy mostly on the rebound of the striker and steel-on-steel collisions. Less brittle materials, on the other hand, present the opposite behavior and fragments tend to remain between the striker and the anvil due to agglomeration of the fragments, resulting in successive breakage until all the kinetic energy of the ball is consumed (TAVARES, 2007). Figure 3.13 illustrates the efficiency of energy transfer from a falling ball to breakage on different materials. It is possible to notice that brittle materials, such as quartz, presents low energy efficiency transfer when compared to the selected ores, such as copper ore and iron ore. For those, the efficiency is still relatively high for larger impact energies.

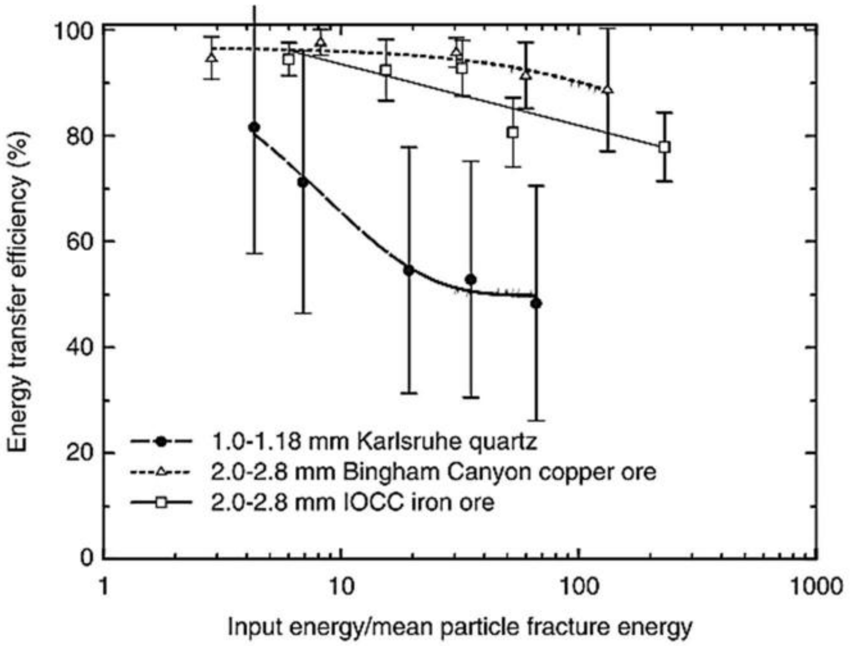

Figure 3.13 - Energy transfer efficiency from the ball to breakage energy for different materials in the ILC as a function of relative impact energy (TAVARES, 2007)

3.2.2. Breakage tests of beds of particles

Whereas breakage tests of single particles describe physical properties of an ore, breakage tests of particles beds provide better understating of particle breakage in several comminution devices. This is due to the uncertainties associated to the application of stresses when particles are grouped in beds of one or more layers at different arrangements. Although presenting a relevant probabilistic effect depending on the material composing the bed, breakage of beds also relies on the geometry of the bed, the type of confinement, the size of the particles and characteristics of the stressing body. Due to that, breakage of beds presents several uncertainties associated to the proportion of the stressing energy that particles positioned in different parts of the bed actually receive. Under unconfined conditions, for example, part of the material will be ejected and escape from being stressed during the nipping phase of the contact (BARRIOS *et al.*, 2011). Because of that, breakage of particles in compressed beds cannot be considered an energy efficient process when compared to single particle breakage. FUERSTENAU *et al.* (1991) estimates that single particle are two times more efficient than breaking particles under confined conditions and four times better than breaking particles under unconfined conditions.

Several models have been developed in recent years to describe breakage of particles on beds. The works of FUERSTENAU *et al.* (1996) and LIU & SCHÖNERT (1996) in confined beds may be cited. The first investigated the effects of bed pressure, material hardness and feed size on energy absorption, energy utilization and product size distribution whereas the latter have studied the influence of feed particle size distribution and the interaction between particles of different sizes.

More recently, BARRIOS *et al.* (2011) investigated breakage of unconfined beds composed of same size particles and impacted by steel balls, equivalent to the environment found in tumbling mills. The authors proposed a model that describes the influences of particle size, impact energy, ball size and bed configuration for different materials. Bed arrangements tested involved the addition of a ring of particles around a central particle until reaching four rings of particles, named monolayer, and three and five layers of particles. To guarantee unconstrained conditions, a fragile paper ribbon was placed around the bed, preventing the bed from falling apart but tearing right after the first contact between the ball and the bed, just as shown in Figure 3.14.

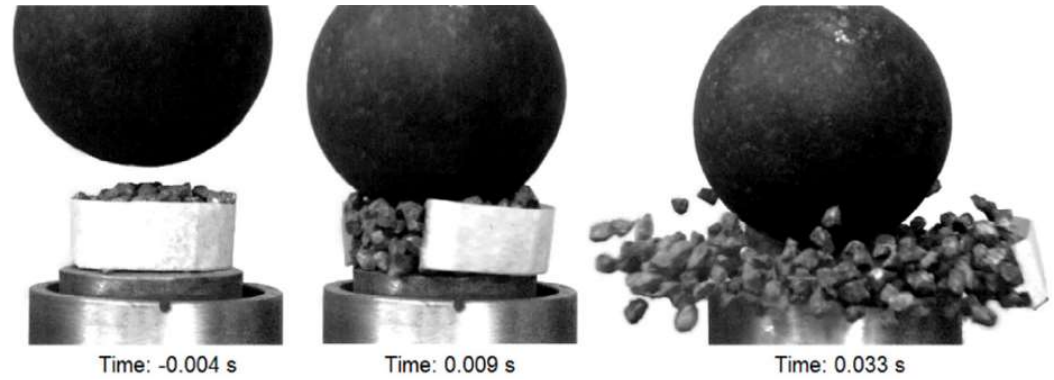

Figure 3.14 - Snapshots from experiment of an impact of 5 layer particle bed with an 88 mm steel ball with impact energy of 3.05 J (JIMÉNEZ-HERRERA *et al.*, 2018)

3.3. UFRJ model

The mechanistic approach of comminution processes aims to decouple the contributions of the comminution devices in the calibration of equations that govern the process. TAVARES & CARVALHO (2009) proposed a mathematical model of batch grinding that was able to describe breakage by impacts from grinding media, producing body breakage, abrasion and weakening from repeated stressing. The model overcame limitations of traditional size-mass balance formulations by taking into account the distribution of stressing energies in the mill and the distribution of fracture energies contained in the charge. The results proved the ability of the model to overcome the limitations of previous approaches that deal with the average properties of the material and that are only able to represent breakage rate as a first order function.

Later named UFRJ model (CARVALHO, 2013), the model comprises a set of equations proposed by TAVARES & KING (1998, 2002) and TAVARES (2004, 2009) that was used to determine the reduction of particle size in a post-processing stage based on energy transfer information collected in DEM simulations, using a microscale formulation of the population balance model (CARVALHO & TAVARES, 2013). The UFRJ model has as advantage the ability to decouple the dominant mechanisms involved in the comminution process, besides considering important aspects, such as the variability of particles properties among themselves, expressed by the distribution of fracture energies, i.e. the breakage probability distribution and their variability over time, reproduced by the weakening of particles due to the accrual of damage in repetitive impacts.

Although it has been designed to operate continuously on a mill by describing the process as a perfect mixer, the use of the UFRJ model can be extended to different comminution and particle degradation processes. The model has already been successfully used in a post-processing stage to predict particle breakage in ball mills (TAVARES & CARVALHO, 2009), autogenous and semi-autogenous mills (CARVALHO & TAVARES, 2011), impact crushers (CUNHA *et al.*, 2014) and the degradation of lump ores and iron ore pellets during handling (TAVARES & CARVALHO, 2012 and TAVARES *et al.*, 2015). Figure 3.15 presents a general scheme of the operating principles of the UFRJ model.

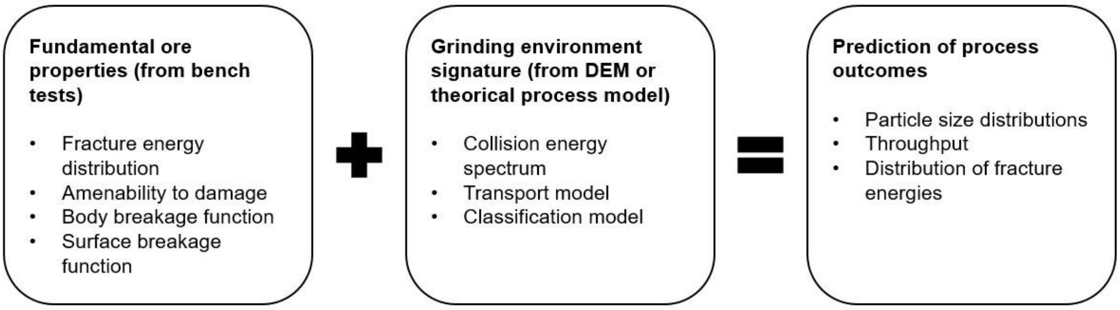

Figure 3.15 - General scheme of the operating principles of the UFRJ model as originally proposed to ball mills (Adapted from CARVALHO, 2009)

The UFRJ model considers the outcome of a stressing event to describe the rates of changes in mass of material contained in size classes i. Particles captured in a stressing event may undergo catastrophic breakage or not depending on the energy involved in the event. If a particle is stressed with enough energy to promote body breakage, it will break and produce progeny fragments. If stresses are insufficient to cause body breakage, particles will suffer surface breakage by abrasion or chipping and will also become weaker. The equation that describes the rates of changes in mass of material in a size class i of a batch mill is (CARVALHO & TAVARES, 2013)

$$\frac{dw_i(t)}{dt} = \frac{1}{M}\sum_j \omega_j \left[-D_{ji,b}(t) - D_{ji,s}(t) + A_{ji,b}(t) + A_{ji,s}(t)\right] \tag{3.5}$$

where M is the mill hold-up, $w_i(t)$ is the mass fraction contained in size class i in the mill, j the collision type and ω is the frequency of stressing events in the comminution machine. D and A are functions that describe the rate of disappearance and appearance of materials in size class i due to body breakage (represented by the subscript b) and surface breakage (represented by the subscript s).

The model's description of particle breakage and weakening is described on the basis of specific equations derived from the microscale characterization of the fracture of individual particles. These equations are dependent on the distribution of fracture energies, which must be calculated simultaneously with equation (3.5). The distribution of fracture energies varies with time and is given by the following equation after a timestep Δt (CARVALHO & TAVARES, 2013):

$$F_i(E, t + \Delta t) = \frac{G_i F_i^*(E, t + \Delta t) + H_i F_i(E, 0) + I_i F_i(E, t)}{G_i + H_i + I_i} \tag{3.6}$$

where G_i is the fraction of material in the class i that has been damaged but remained in the original size range, H_i is the fraction of material that appeared in the class i due to body or surface breakage and I_i is the fraction of material that did not undergo any impact event during the timestep Δt. In equation (3.6), $F_i^*(E, t + \Delta t)$ is the distribution of fracture energies of the particles in class i that were captured in an impact event during the timestep Δt but did not fracture, $F_i(E, 0)$ is the original distribution of fracture energies and $F_i(E, t)$ is the distribution of fracture energies of the material contained in size class i before the timestep Δt.

The equations adopted in the UFRJ model to describe body breakage, particle weakening due to unsuccessful impacts and the fracture energy distribution are detailed in the following sections of the present work. Further details concerning equations (3.5) and (3.6) can be found elsewhere (CARVALHO & TAVARES, 2013).

3.3.1. Fracture energy distribution and breakage probability

The energy involved in a contact is responsible for leading particles to breakage. When the dissipated energy on the particle surpasses the minimum energy required for breakage, the particle will fail. Due to uneven presence of internal flaws and particle shape (TAVARES & KING, 1998), individual fracture energies of particles within a sample are scattered and must be represented by an appropriate statistical distribution. Among the available distributions used to describe single-particle fracture energy, the upper-truncated log-normal distribution has provided the most accurate fit between experimental data and analytical equations, consisting of a cumulative probability distribution for a measured value of energy dissipated in the contact, as presented in Figure 3.16. The upper-truncated log-normal distribution is given by (TAVARES & KING, 1998, 2002)

$$P_o(E) = \frac{1}{2}\left[1 + \operatorname{erf}\left(\frac{\ln E^* - ln\, E_{m50}}{\sqrt{2\sigma^2}}\right)\right] \tag{3.7}$$

and

$$E^* = \frac{E_{max}\, E_m}{E_{max} - E_m} \tag{3.8}$$

where E_m is the energy absorbed by the particle during the collision, which corresponds to the specific fracture energy of the particle, E_{max} is the upper truncation value of the distribution, E_{m50} and σ^2 are the median and the geometric variance of the distribution, respectively.

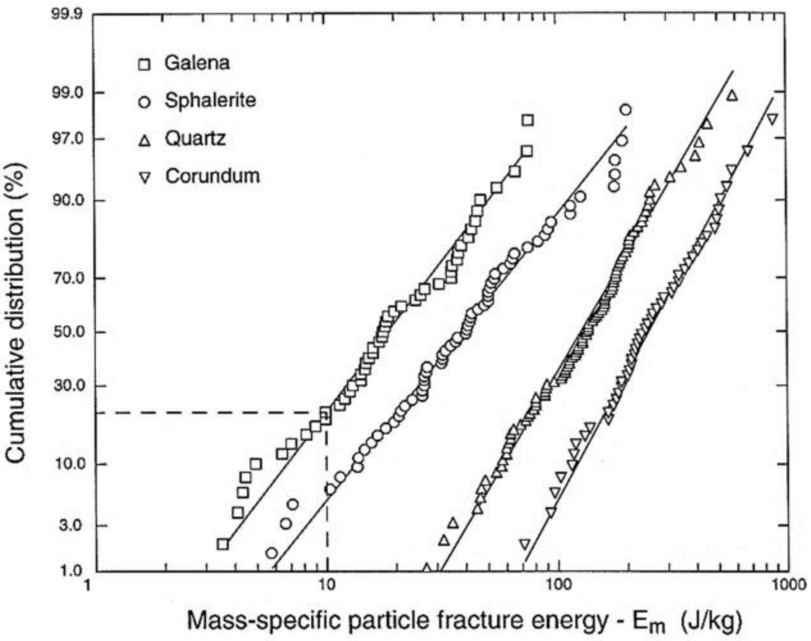

Figure 3.16 – Particle fracture energy distributions of 2.0 – 2.8 mm particles of various minerals. Lines represent data from equation (3.7) (TAVARES & KING, 1998)

Particle fracture energy and particle strength are strongly related to particle size. When decreasing particle size both distributions will shift towards higher values. This behavior is explained by Griffith's theory, stating that the size of cracks decreases as particles become finer (TAVARES & KING, 1998). The reduction in the number and size of cracks is responsible for increasing the fracture energy of the particles. The relationship between particle size and the median fracture energy of a specific size is described by (TAVARES & KING, 1998)

$$E_{m50} = E_{\infty}\left[1 + \left(\frac{d_o}{d_j}\right)^{\varphi}\right] \tag{3.9}$$

where E_{∞}, d_o and φ are model parameters fitted to experimental data and d_j is the representative size of the size class of interest. Figure 3.17 illustrates the variation on the mean specific particle fracture energy when changing the particle size. The model parameters in equation (3.9) may be estimated based on the data presented in Figure 3.17 by least-squares.

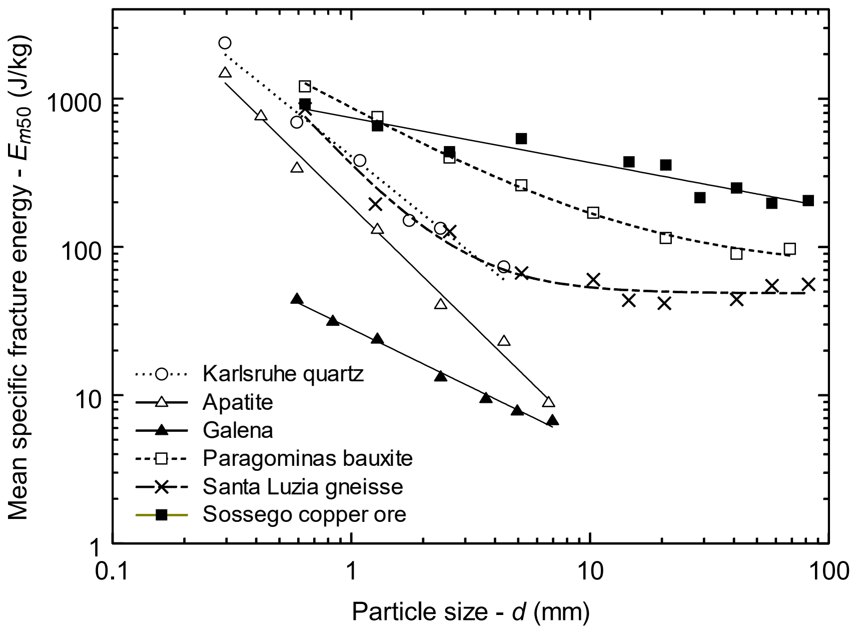

Figure 3.17 - Variation of mean specific particle fracture energy with particle size for different materials. Lines represent fitting of equation (3.9) to data (TAVARES, 2007)

3.3.2. Damage mechanics

Particles are often subjected to impacts that are insufficient to cause breakage inside a comminution device. Evidence of fracture by repeated stressing on autogenous and semi-autogenous mills (MORRISON & CLEARY, 2004) and compression crushers, such as jaw, cone and gyratory crushers (TAVARES & CARVALHO, 2007) are well-known and the proper description of comminution on several equipment is only possible when taking this mechanism into consideration.

According to VERVOORN & AUSTIN (1990), there are at least two reasons why a particle may not break on the first impact but only after several loading events. The first reason can be explained by the orientation of the particle during the collision, indicating that repeated impacts are necessary in order to achieve a favorable orientation regarding existing cracks in the particle. The second reason concerns the growth of pre-existing defects during repeated impacts, reaching their critical size or concentration. However, when testing particles in a drop weight test apparatus, not many orientations can be tested, leading to the conclusion that the second argument of defect growth is doubtless the mechanism that governs particle breakage due to repetitive impacts (TAVARES & KING, 2002).

Whenever an amount of energy that is insufficient to lead a particle to its breakage is applied, the particle will become more amenable to break on a subsequent stressing event due to the volume change of internal cracks and flaws. Evidence of propagation of pre-existing cracks are shown by TAVARES & KING (2002). Figure 3.18 illustrates how the applied energy induces internal changes to the structure of a particle, resulting in a weaker particle.

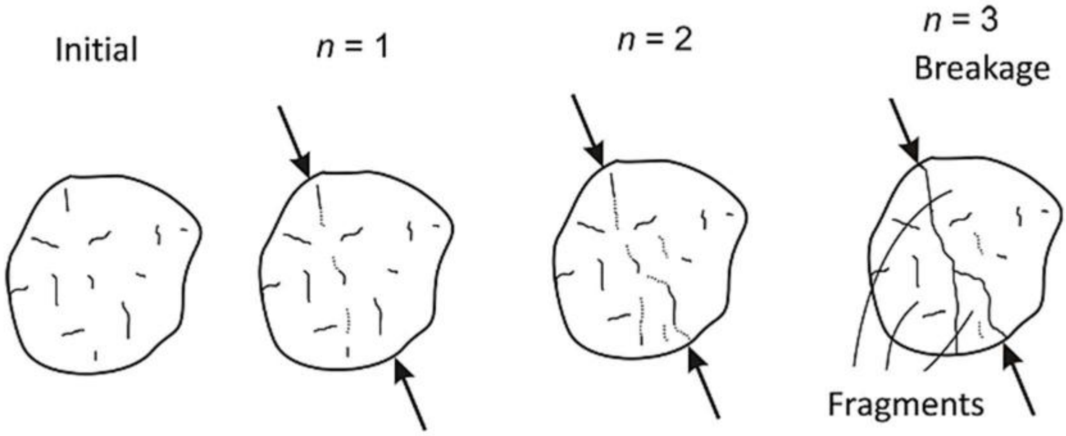

Figure 3.18 - Particle weakening due to accrual of damage in unsuccessful loading events (TAVARES, 2009)

The numerical model used to characterize damage accrual in the UFRJ model is described by TAVARES & KING (2002) and is based on Hertz contact theory and continuum damage mechanics. Considering F as the force acting on a particle during impact and ϑ the deformations, the equation describing the force-deformation relation is given by

$$F = \frac{d^{\frac{1}{2}}}{3}\,\tilde{k}\vartheta^{\frac{3}{2}} \tag{3.10}$$

and

$$\tilde{k} = k(1 - D) \tag{3.11}$$

where $\tilde{k}$ represents the stiffness of the particle, a value that reduces as it suffers deformations and k is the stiffness of the particle before impact. D represents the damage and it is responsible for the reduction in particle stiffness.

Considering the relation between damage and deformation as

$$D = \left(\frac{\vartheta}{\vartheta_c}\right)^{\gamma} \tag{3.12}$$

where ϑ_c is the deformation at fracture and γ is the damage accumulation constant, that varies accordingly to material. Larger values of γ indicates low weakening by damage while small values of γ indicates that damage is significant at low relative deformations.

Damage is irreversible and due to that, the force-deformation profile during unloading will not match the observed one during particle loading. According to TAVARES & KING (2002), when internal damage is sustained, part of the solid is relaxed and local strain energy is converted to heat, in addition to that used to break the bonding between the fresh internal surfaces produced. This loss of strain energy cannot be recovered during restitution, as presented in Figure 3.19. Adapting equation (3.11), the stiffness reduction due to an impact is given by

$$k_n = k_{n-1}(1 - D_n^*) \tag{3.13}$$

where k_{n-1} and k_n are the stiffness of the particle prior and after the *n*th impact and D_n^*, the amount of damage induced in the particle after the *n*th impact.

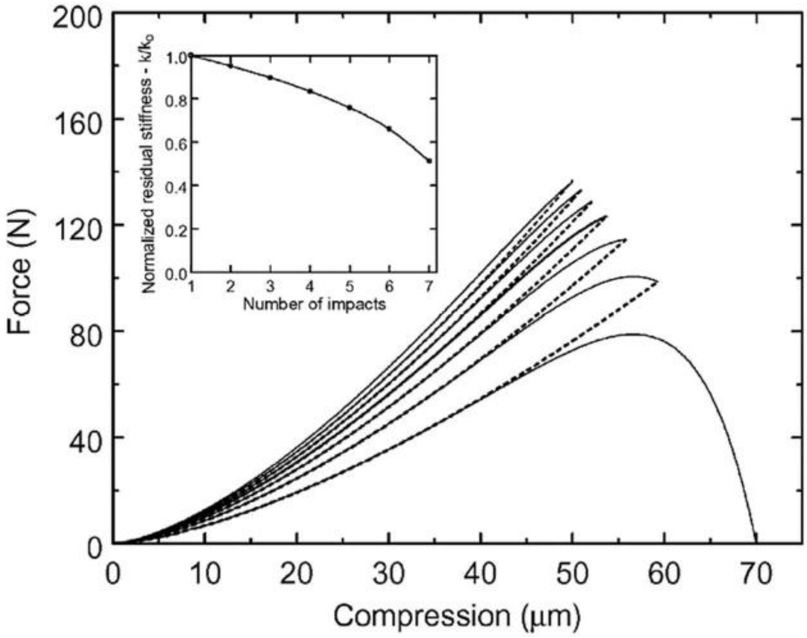

Figure 3.19 - Predicted force-deformation profiles resulting from repeated loading of a marble particle (TAVARES & KING, 2002)

The specific strain energy absorbed by one particle subjected to load can be calculated by the integration of the force-displacement profile divided by particle mass m_p,

$$E_{k,n} = \frac{1}{m_p}\int_0^{\vartheta_n} F d\vartheta \tag{3.14}$$

Assuming that all the energy applied to a particle, which corresponds to the kinetic energy of the striker, is effectively converted into strain energy, then substituting equations (3.10) to (3.12) in equation (3.14), the specific strain energy will be

$$E_{k,n} = \frac{1}{m_p}\int_0^{\vartheta_n} \frac{k\sqrt{d}}{3}\left[1-\left(\frac{\vartheta}{\vartheta_c}\right)^{\gamma}\right]\vartheta^{\frac{3}{2}} d\vartheta \tag{3.15}$$

By defining D_n^* according to

$$D_n^* = \left(\frac{\vartheta_n}{\vartheta_c}\right)^{\gamma} \tag{3.16}$$

where ϑ_n is the maximum deformation reached during the *n*th impact, equation (3.16) becomes

$$E_{k,n} = \frac{2}{15}\left(\frac{2\gamma + 5 - 5D_n^*}{2\gamma + 5}\right)\frac{d^{\frac{1}{2}}\, k_{n-1}\, \vartheta_n^{\frac{5}{2}}}{m_p} \tag{3.17}$$

where $E_{k,n}$ is the kinetic specific energy of the striker at the *n*th impact.

The energy required to fracture a particle can be calculated by considering D_n^* = 1 and ϑ_n = ϑ_c in equation (3.17), which gives

$$E_{n-1} = \frac{4\gamma}{15(2\gamma + 5)}\frac{d^{\frac{1}{2}}\, k_{n-1}\, \vartheta_c^{\frac{5}{2}}}{m_p} \tag{3.18}$$

Assuming that the equation (3.18) remains valid throughout several impacts, by replacing equation (3.18) in equation (3.13) the relation between specific particle fracture energies at successive impacts is given by

$$E_n = E_{n-1}(1 - D_n^*) \tag{3.19}$$

At last, by rearranging equations (3.17) and (3.18) and substituting the ratio between maximum deformation at an impact and the threshold deformation for fracture as given in equation (3.16) the amount of damage sustained in the *n*th impact cycle is given by

$$D_n^* = \left[\frac{2\gamma}{(2\gamma + 5 - 5D_n^*)} \frac{E_{k,n}}{E_{n-1}}\right]^{\frac{2\gamma}{5}} \tag{3.20}$$

The only parameter of the model that requires fitting is γ, therefore its application is quite simple and only demands few tests per ore type. Due to the fact that D_n^* is implicit in equation (3.20), the application of the model requires simultaneous use of equations (3.19) and (3.20) in an iterative process that typically converges to a solution in about 10 iterations from an initial guess of D_n^* = 0. TAVARES (2009) also demonstrated that the parameter is relatively independent of particle size. Figure 3.20 shows the agreement between predicted and expected values for limestone particles subjected to different impact energies.

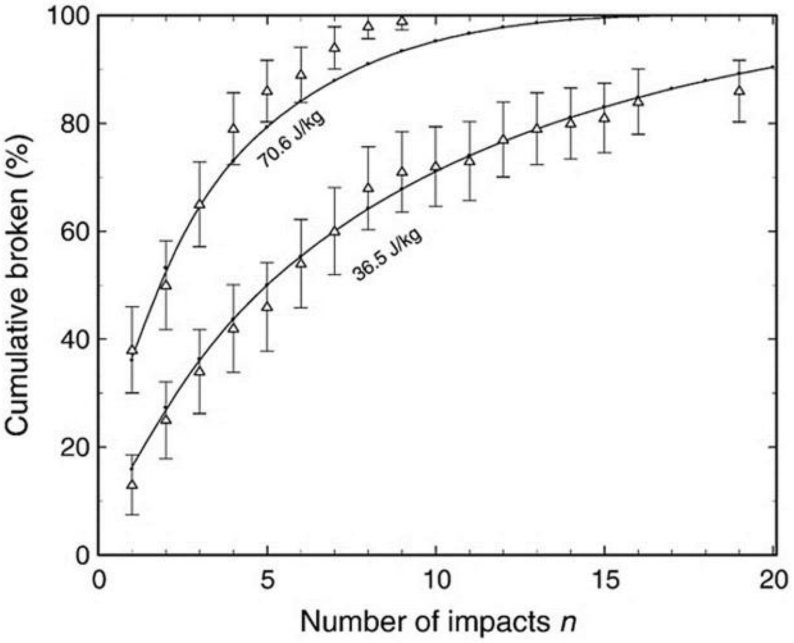

Figure 3.20 - Experimental (triangles) and predicted (lines) cumulative percentage broken after repeated impacts at two impact energies of bauxite ore of 45.0 – 37.5 mm (TAVARES, 2009)

3.3.3. Particle size distribution

Body breakage and progeny size can be described on the basis of empirical models that correlate particle fragmentation and the stressing energy applied to the particle. NARAYANAN & WHITEN (1988) parameterized particle breakage on the basis of t_n parameters, which correspond to the percentage, in mass, of material passing on a screen aperture equivalent to the original particle size divided by the *n* index:

$$t_n = P\left(\frac{d_o}{n}\right) \tag{3.21}$$

where d_o is the original size of the particle, representing the representative size of a class, and $P(x)$ is the cumulative passing on the size d_o/n.

Progeny fineness is directly related to energy input and can be successfully described based on t_{10} parameter, which corresponds to the cumulative passing on a sieve with aperture of 1/10th the original particle size, according to the exponential function (NAPIER-MUNN *et al.*, 1996):

$$t_{10} = A(1 - e^{-bE_{cs}}) \tag{3.22}$$

where A and b are model parameters fitted to experimental data and vary as function of the ore breakage properties and E_{cs} is the specific impact energy.

The parameters t_{10}, A and b are of great importance for the analysis of the degree of fragmentation imposed to a particle. The product between A and b is widely used as an index to determine ore amenability to breakage. Lower values of $A * b$ indicate that the ore is hard to break. In addition, the relation between t_{10} and E_{cs} characterizes the effect of input energy on breakage fineness, as illustrated in Figure 3.21. The explanation of finer fragmentation of the original particle is due to the occurrence of successive breakage events until the complete dissipation of the input energy. However, the parameter A indicates the saturation value of t_{10} for a specific energy, in which any value of energy beyond will not generate finer progeny.

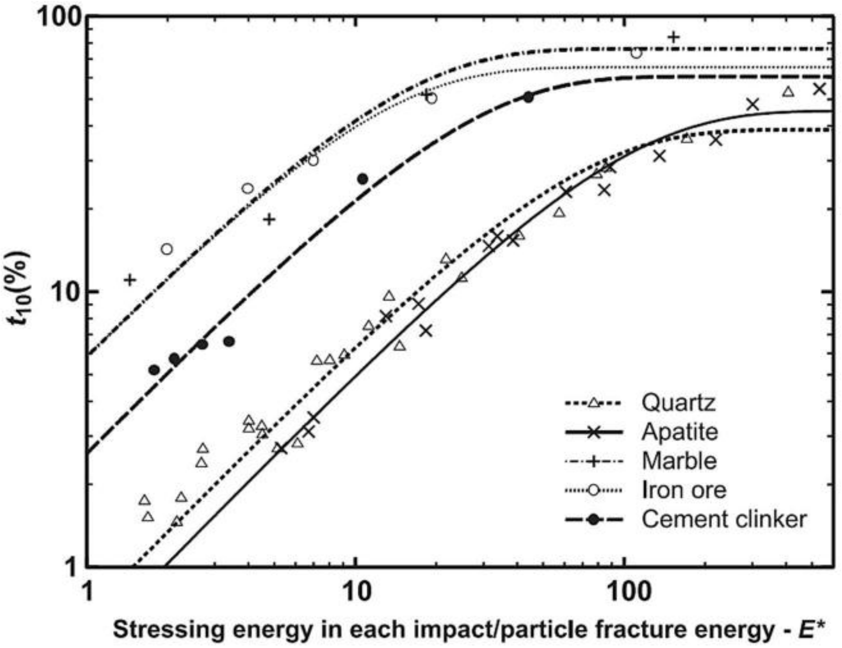

Figure 3.21 – Relationship between t_{10} and stressing intensity for various materials (TAVARES, 2004)

The relation between t_{10} and t_n parameters can be expressed by interpolation using a set of cubic splines in a t_{10} versus t_n graph. The interpolation data set is named appearance function and it is helpful in the determination of the progeny size distribution in the cumulative percentage passing form, as presented in Figure 3.22. The appearance function can be populated based on impact tests.

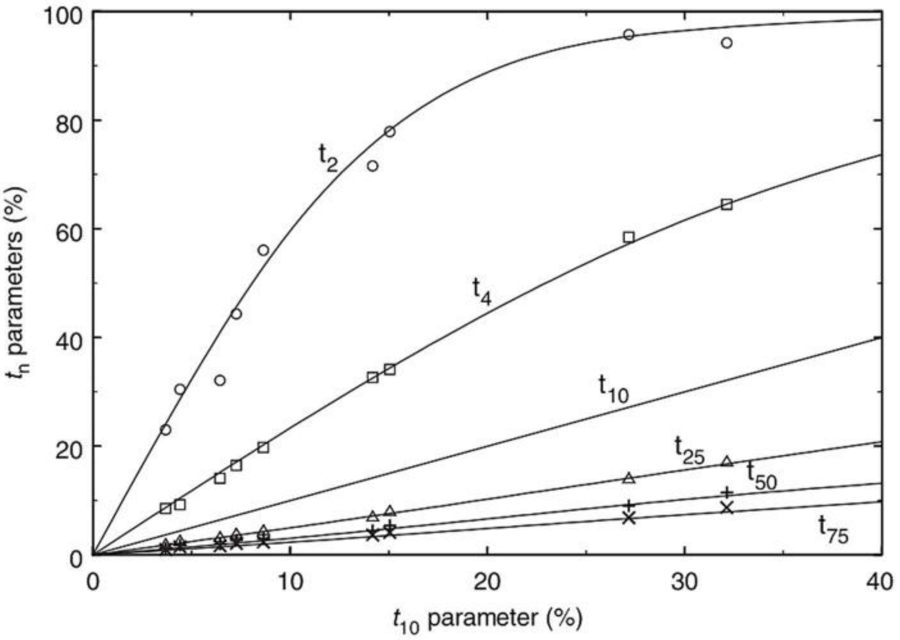

Figure 3.22 - Appearance function for a sample of copper ore. Lines represent fitting with splines (TAVARES, 2007)

Although equation (3.22) correlates t_{10} and E_{cs}, it does not take into account the variation of particle size in this relation. The UFRJ model utilizes an adaptation of the original equation introduced by NARAYANAN & WHITEN (1988) that incorporates the effect of fracture energy, which is governed by particle size and influences the t_{10} and E_{cs} relationship. The new expression for t_{10} is given by (TAVARES, 2009)

$$t_{10} = A\left[1 - \exp\left(-b' \frac{E_{k,n}}{E_{50b}}\right)\right] \tag{3.23}$$

where A and b' are fitting parameters of the equation and E_{50b} is the median mass-specific particle fracture energy of the particles that break in an impact of magnitude $E_{k,n}$. For the cases where $E_{k,n}$ is higher than the fracture energy of the toughest particle of the size class E_{50b} becomes E_{50}, which is the median fracture energy of the distribution determined by equation (3.7) and (3.8). The agreement between fitted and measured results for different particle sizes is show in Figure 3.23. The familiarity with the equation (3.22) is explicit by recognizing that the parameter A has the same meaning in both equations, whereas the parameter b' can be approximately given by

$$b = \frac{b'}{E_\infty \left[1 + \left(\frac{d_o}{38.1}\right)^{\varphi}\right]} \tag{3.24}$$

where 38.1mm is the average size of particles used in standard test (13.2 to 63 mm) of the original procedure proposed by the Julius Kruttschnitt Mineral Research Centre (JKMRC) (NAPIER-MUNN *et al.*, 1996).

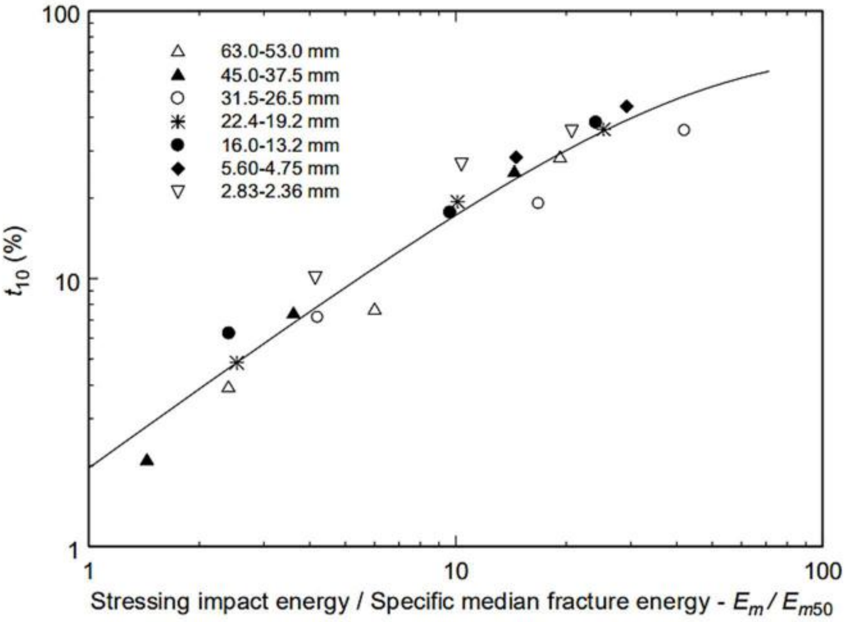

Figure 3.23 - Relation between measured t_{10} values and fitted results using equation (3.23) for a copper ore sample (CARVALHO & TAVARES, 2011)

The expression to determine E_{50b} of the original distribution can be derived from equation (3.7) and it is only valid to represent the median fracture energy of the particles that break in the first impact. The expression is given by (TAVARES, 2009)

$$E_{50b} = E_{50} \exp\left[\sqrt{2}\sigma \operatorname{erf}^{-1}(P(E_{k,n}) - 1)\right] \tag{3.25}$$

Another characteristic of the UFRJ model is the introduction of the incomplete beta function to determine the relationship between t_{10} and the various values of t_n, overcoming the limitations imposed by the adoption of the cubic spline method to define the progeny size distribution. The incomplete beta function is mathematically described by (CARVALHO & TAVARES, 2013):

$$t_n(t_{10}) = \frac{100}{\int_0^1 x^{\alpha_n - 1}(1-x)^{\beta_n - 1}dx}\int_0^{t_{10}/100} x^{\alpha_n - 1}(1-x)^{\beta_n - 1}dx \tag{3.26}$$

where each t_n corresponds to the percentage passing in a sieve with aperture of d_j/n, in which d_j is the original particle size and α_n and β_n are model parameters fitted to experimental data for each value of t_n.

3.4. Discrete element method

The discrete element method (DEM) is a numerical method initially proposed by CUNDALL (1971) to describe blocks of rock and later generalized to granular materials by CUNDALL & STRACK (1979). Previously limited to simulations involving few particles in two dimensions, the method became more robust due to the rapid advance in computational performance that occurred in the second half of the twentieth century, making it able to simulate a large number of particles in three dimensions.

The working principle of DEM is the tracking of individual rigid particles in a particulate flow by reproducing their movements and interactions, thus allowing the prediction of the behavior of the flow. The method is based on the determination of the movement of the particles based on forces calculated from each contact using a previously select contact model. It is a cyclic process performed at each timestep until the end of the simulation is established, according to the flowchart of Figure 3.1.

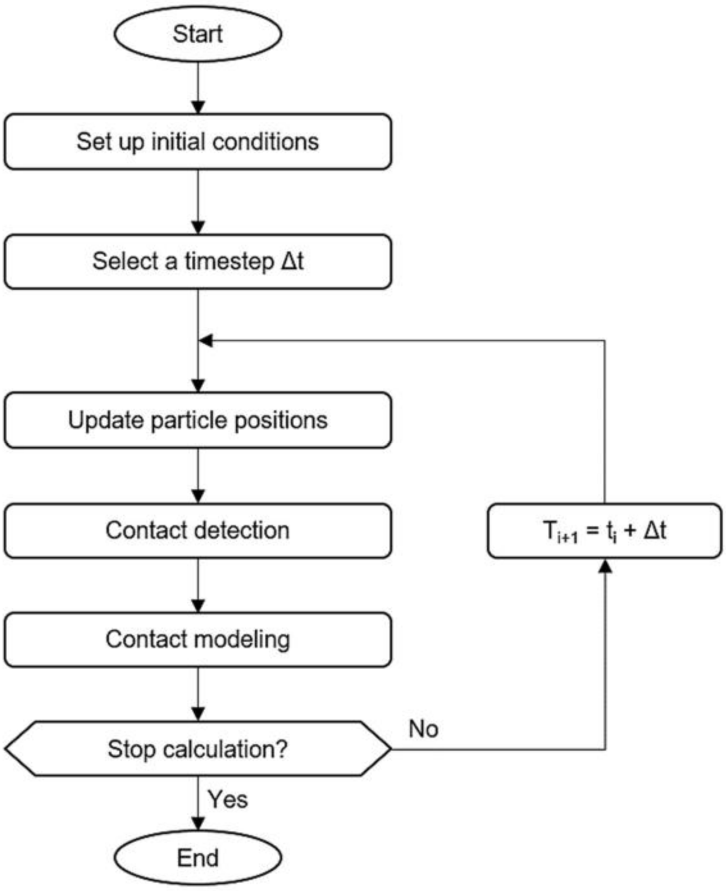

Figure 3.24 - Flowchart indicating the working principles of a DEM algorithm (Adapted from SEVILLE & WU, 2016)

The detection of a contact occurs through the overlap of two elements. It is inferred that this overlap corresponds to a local deformation of the particle and that its size is very small when compared to the particle size (SEVILLE & WU, 2016). One of the most common problems associated with DEM simulations is the use of a very large time interval, resulting in unnatural overlap between particles and the generation of high contact forces. In order to guarantee that forces resulting from the contacts are determined only from the interaction between neighboring particles it is necessary to establish a time interval that is small enough to ensure that the perturbations do not propagate to any particles other than those in direct contact (CUNDALL & STRACK, 1979), which makes the method computationally costly.

The motion of each particle is determined by the application of Newton's second law based on the forces resulting from interactions with other particles or geometries. Thus, the translational and rotational movements of each particle in a given timestep are obtained, respectively, by the equations:

$$m_i \frac{d^2}{dt^2}\overrightarrow{x_i} = \sum_{i=1}^{n} F_i + m_i g \tag{3.27}$$

$$I_i \frac{d}{dt}\overrightarrow{\omega_i} = \sum_{i=1}^{n} T_i \tag{3.28}$$

where m_i, $\overrightarrow{x_i}$, I_i e $\overrightarrow{\omega_i}$ are, respectively, the mass, the position, the moment of inertia and the angular velocity of the particle, F_i corresponds to the sum of forces due to interactions with other particles or geometries of the system, T_i, the sum of torques resulting from tangential contact forces and g, the acceleration of gravity.

3.4.1. Contact modeling in DEM

The calculated contact forces from the overlap between particles are directly related to the contact model used. There are several models capable of describing the interaction between different elements, and the main ones are implemented in the various commercially available discrete element simulation tools, such as the Hertz-Mindlin model for normal and tangential components (HERTZ, 1882, MINDLIN, 1949, MINDLIN & DERESIEWICZ, 1953), adopted as standard in the EDEM® platform and the hysteretic linear spring model (WALTON & BRAUN, 1986) for calculating the normal component and the linear spring Coulomb limit model for the tangential component, both used as standard on the Rocky DEM platform. It should be emphasized that the comparison between different contact models is not the subject of interest in the present work and that Rocky DEM was the only software used to perform the simulations, and therefore, greater attention will be given to the last two models cited.

3.4.1.1. Hysteretic linear spring model

The hysteretic linear spring model, proposed by WALTON & BRAUN (1986), is a normal elastoplastic contact model, allowing the introduction of plastic deformation behavior in the mechanics of contact. In this model, the particles exhibit elastic behavior until a critical deformation, from which they begin to reproduce the behavior of a plastic deformation (DEM SOLUTIONS, 2018). Analyzing the force-displacement diagram and the contact description shown in Figure 3.25, it is noticed that after unloading of the contact, i.e., when the force becomes null, there is a remaining overlap between the particles representing the plastic deformation suffered by them. At the end of the contact, the residual deformation is not recorded by the model and the particle will behave like an original particle, in the case where the particle is reloaded before the end of the contact, loading will respect the slope BC of the force-deformation diagram. According to the model, the energy dissipated in the collision is numerically equal to the region delimited by the triangle ABC of Figure 3.25.

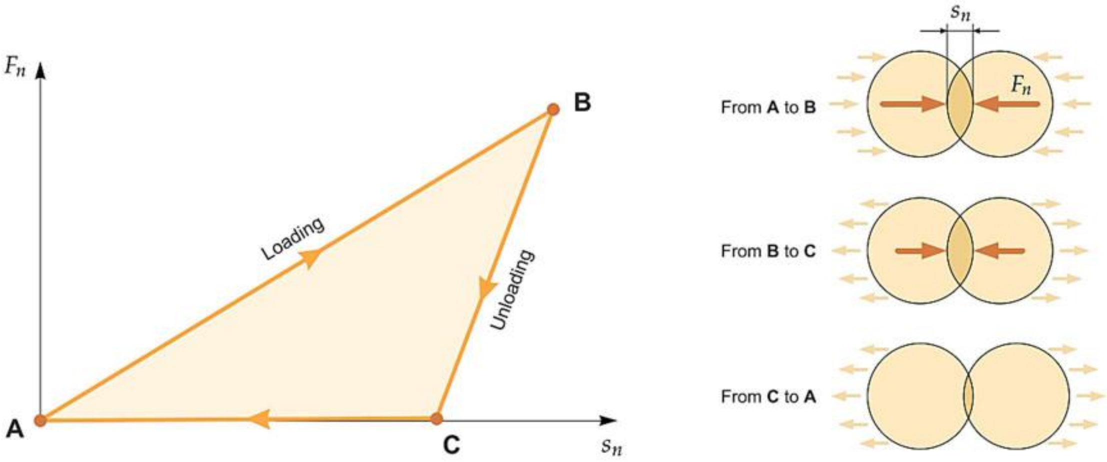

Figure 3.25 - Typical loading cycle in a force-deformation diagram comparing with the overlap between two particles in the hysteretic linear spring model (ROCKY DEM, 2018)

The normal forces of the contacts detected by the hysteretic linear spring model respect the equations (ROCKY DEM, 2018):

$$F_n^t = \min\left(K_c \text{ x } s_n,\ F_n^{t-\Delta t} + K_d \text{ x } \Delta s_n\right) \quad \text{if } \Delta s_n \geq 0 \tag{3.29}$$

$$F_n^t = \max\left(F_n^{t-\Delta t} + K_d \text{ x } \Delta s_n, 0.001 K_c \text{ x } s_n\right) \quad \text{if } \Delta s_n < 0 \tag{3.30}$$

where Δt is the timestep adopted, F_n^t and $F_n^{t-\Delta t}$ correspond to the normal elastoplastic forces of the contact at timesteps t and $t - \Delta t$, respectively, K_c and K_d correspond to the contact's loading and unloading normal stiffness, respectively, s_n is the overlap between the elements and Δs_n, the difference between the overlaps at timesteps t and $t - \Delta t$.

Equations (3.29) and (3.30) are valid for both loading and unloading of the contact due to the use of minimum and maximum functions while determining the normal contact force. The expression $0.001 K_c \text{ x } s_n$ in equation (3.30) ensures that the normal contact force will remain zero during the unloading phase of the contact from C to A shown in Figure 3.25.

The loading (K_c) and unloading (K_d) normal stiffness relies on the particle size (d_i), bulk Young's modulus (Y), hereinafter referred to interchangeably as "Young's modulus", and the coefficient of restitution of the elements in contact (ε) according to the following equations:

$$K_c = \frac{K_{c,i}K_{c,j}}{K_{c,i} + K_{c,j}} \tag{3.31}$$

$$K_d = \frac{K_c}{\varepsilon^2} \tag{3.32}$$

where $K_{c,i}$ and $K_{c,j}$ are the stiffnesses of the elements involved in the contact, which can be both a particle or a geometry of the system. The calculation of the normal stiffness of each element is given by

$$K_c = Y \text{ x } d_i \tag{3.33}$$

and considering that for a particle–particle contact, d_i corresponds to the size of each particle and for a particle–geometry contact, d_i corresponds to the size of the particle involved in the impact, making the calculation of the contact stiffness dependent only on the respective bulk Young 's moduli of the elements involved in the contact.

3.4.1.2. Linear spring Coulomb limit model

The linear spring Coulomb limit model is an elastic-frictional model for the tangential component of the contact (ROCKY DEM, 2018). In this model the tangential force of the contact (F_τ^t) cannot exceed the Coulomb limit, respecting the following equations:

$$F_\tau^t = \min\left(\left|F_{\tau,e}^t\right|, \mu F_n^t\right)\frac{F_{\tau,e}^t}{\left|F_{\tau,e}^t\right|} \tag{3.34}$$

$$F_{\tau,e}^t = F_\tau^{t-\Delta t} - K_\tau \Delta s_\tau \tag{3.35}$$

$$K_\tau = r_K K_c \tag{3.36}$$

where $F_{\tau,e}^{t}$ is the tangential force of the contact, defined by equation (3.35), if it was considered purely elastic, F_n^t is the normal contact force and μ is the coefficient of friction. $F_\tau^{t-\Delta t}$ is the tangential force at the previous timestep $(t - \Delta t)$, Δs_τ is the tangential relative displacement between two particles during the timestep and K_τ is the tangential stiffness, defined by equation (3.36). r_K is the tangential stiffness ratio and K_c, is the normal load stiffness of the contact, according to equation (3.31).

According to the model, the value of μ in equation (3.34) refers to the coefficient of static friction (μ_s) if no sliding takes place at the contact or the coefficient of dynamic friction (μ_d), if sliding does take place at the contact. The presence of sliding is considered when the value of $F_{\tau,e}^{t}$ exceeds the limit of Coulomb, established by $\mu_s F_n^t$.

3.4.2. Breakage modeling in DEM

The adoption of DEM in an attempt to optimize the operation of comminution equipment and to understand the breakage phenomena consisted of an important advance in the mineral processing industry. For some cases of simulations using the discrete element method, the stresses arising from particle contacts are not relevant as they do not affect the integrity of the particles. For these cases, the use of contact models, such as the Hertz-Mindlin model or the hysteretic linear spring model coupled with the linear spring Coulomb limit model, are sufficient to represent the behavior of the particulate flow in the system.

As discussed in section 3.3, in some cases, such as ball mills, for example, the information extracted in a DEM simulation can be used as input in a later processing stage to predict particle breakage (WEERASEKARA *et al.*, 2013, TAVARES, 2017), as in the works of DATTA & RAJAMANI (2002) and TAVARES & CARVALHO (2009). However, for several types of crushers the representation of particle breakage within the DEM environment is necessary to ensure flow through the compression chamber (WEERASEKARA *et al.*, 2013). In order to study the process of comminution, a model to describe the breakage phenomenon needs to be coupled to the contact models, enabling the fragmentation of particles when subjected to a critical stress.

Different approaches have been adopted to simulate particle breakage inside the DEM environment. Spherical shape elements are usually used for particle representation because of their reduced computational cost. However, work involving polyhedral particles has also shown good results, making it a feasible option due to the technological development that has occurred in the last decade. The following discussion regarding breakage description in DEM classifies the approaches in two groups, depending whether it describes progeny particles from a breakage event as a set of elements bonded together or by instantaneously replacing the parent particle by its progenies.

3.4.2.1. Breakage modeling adopting bonding elements

The first group is represented by techniques in which parent particles are represented as primary particles that are bonded together and that are fully resolved from the beginning of the simulation. It is possible to highlight some approaches concerning the use of bonding elements particles to represent breakage in DEM environment. The first approach consists of the bonded particle model (BPM) proposed by POTYONDY & CUNDALL (2004). In this model, the particles are represented by a cluster of spherical elements joined at their point of contact by bonds. Each bond provides resistance to different load modes, such as tension, shear and compression between each sphere in the contact. An irregularly shaped particle can be obtained by introducing elements of various sizes in the distribution, as shown in Figure 3.26. The adoption of a relatively large size distribution also contributes to a higher packing density of the particle (GROOT & STOYANOV, 2011), minimizing one of the problems of the model that refers to the conservation of volume after breakage, since a set of particles will not present the same density of a solid.

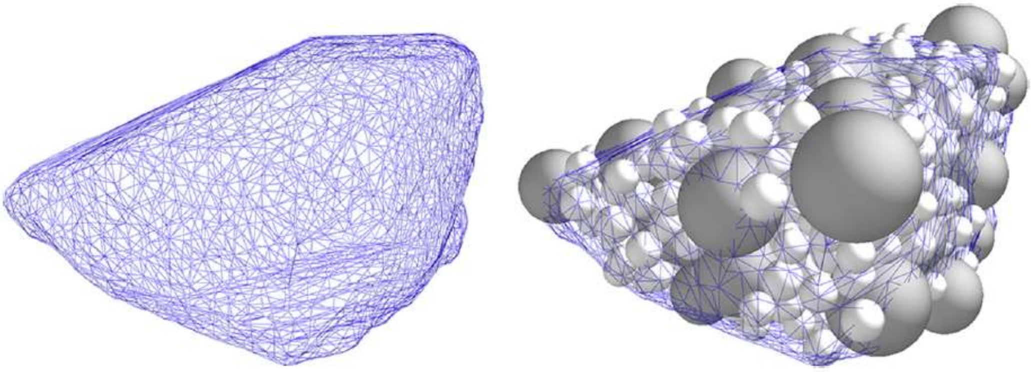

Figure 3.26 - Cluster of spherical particles representing a 3D scanned particle with realistic shape (QUIST & EVERTSSON, 2016)

The forces that act on a bonding element can be seen in Figure 3.27, where a bond of radius R_b and length L_b is subjected to the resultant force $\vec{F}_b$ and the normal M_b^n and tangential M_b^s components of the momentum. If the normal or tangential stresses exceed the critical limits established for the bonding elements, they will break (WEERASEKARA *et al.*, 2013) and the new particles begin to interact with each other according to the contact model established for simulation.

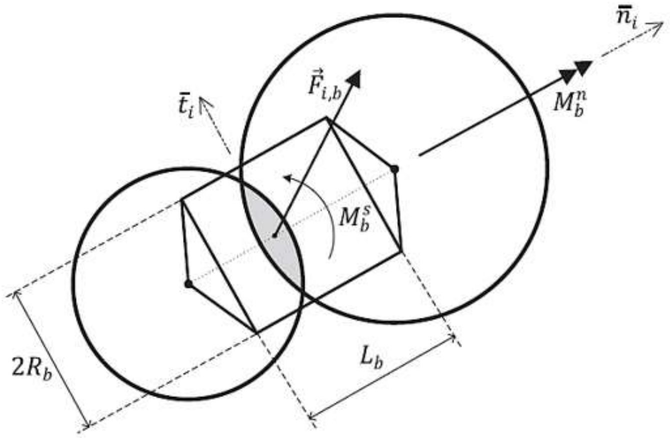

Figure 3.27 - Schematic representation of two particles bonded together with a cylindrical beam leading to different load modes (Adapted from POTYONDY & CUNDALL, 2004)

Several studies using the bonded particle model can be identified in the literature. However, due to its high computational cost, the BPM was initially appropriate to investigate and describe breakage phenomena involving only a few particles. Studies on slow compression of two-dimensional concrete spheres were performed by KHANAL *et al.* (2005), whose bonding elements were used to simulate the interaction between the aggregates and the cementitious paste. Subsequently, KHANAL *et al.* (2007) expanded these tests for slow particle bed compression by evaluating the effects of compression speed and the effect of bed confinement on particle fragmentation. In relation to impact tests, the work of SCHUBERT *et al.* (2005) can be cited, in which the projection of the same concrete spheres initially used by KHANAL *et al.* (2005) against surfaces in different configurations was simulated, obtaining good correlation between the real and simulated behavior of the material.

Simulations of comminution equipment using BPM were also performed. Among them, it is possible to mention the work of METZGER & GLASSER (2013), in which cubic particles were simulated in a ball mill, evaluating different variables in the process of breakage. The work of QUIST *et al.* (2011) correlating liner wear of a gyratory crusher and particle comminution and QUIST & EVERTSSON (2016) demonstrating BPM's potential to predict properties of a cone crusher, such as its flow, pressure and energy draw, can also be mentioned.

Although the BPM presents cases of success in its implementation, it is a very computationally costly model, since a single particle may be constituted of several spherical elements, increasing considerably the number of contacts throughout the simulation. Moreover, the characterization of breakage in the bonded particle model is quite complex, since several parameters are necessary for the creation of particles whose breakage matches some aspects found in experiments (JIMÉNEZ-HERRERA *et al.*, 2018). By adopting spherical primary particles, the model also fails to guarantee volume conservation after breaking (QUIST & EVERTSSON, 2016). Finally, PATWA *et al.* (2016) and JIMÉNEZ-HERRERA *et al.* (2018) reported great difficulty in predicting particle size distribution after breakage.

The use of non-spherical particles in DEM was possible by the introduction of an algorithm capable of detecting contact of elements with arbitrary shapes (CUNDALL, 1988). An approach that presents great resemblance to the working principles of the bonded particle model is the discrete grain breakage (DGB) (HERBST & POTAPOV, 2004). First introduced by POTAPOV & CAMPBELL (1994, 1996) for simulations in two dimensions and in three dimensions, respectively, this approach considers the existence of bonding joints between the various geometries constituting the particle in its contact surfaces, as shown in Figure 3.28. According to this approach, the particle is composed of several unbreakable solid elements and the bonding joints between them resist normal and shear forces to a certain extent. After rupture of the bonding joint, it becomes unable to withstand tensile stresses, allowing the propagation of cracks internally through the particle. A detailed operation for two-dimensional elements can be found in POTAPOV *et al.* (1995).

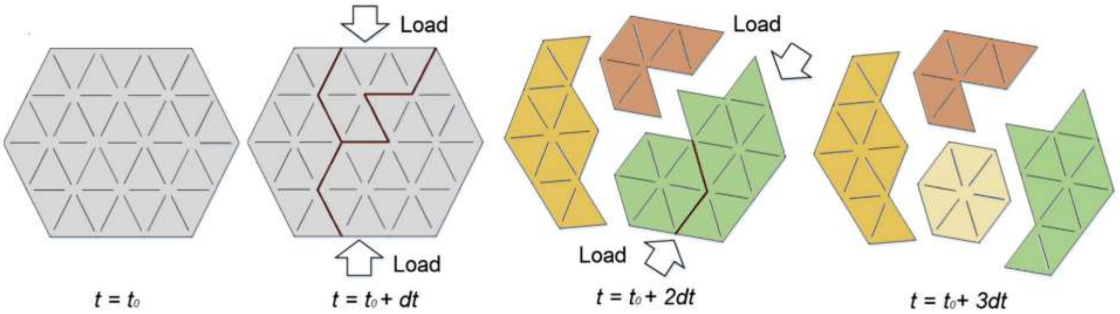

Figure 3.28 - Illustration of particle breakage in two dimensions adopting polyhedral particles with bonding joints between the elements (JIMÉNEZ-HERRERA *et al.*, 2018)

There are relatively few works in the literature that use this approach, especially in the case of simulation of comminution equipment, due to the high computational demand. Among the few, the work of POTAPOV & CAMPBELL (1994) in the simulation of circular discs formed by triangles can be cited, varying properties such as Young's modulus, Poisson's ratio and energy transfer for particles, and also the work of POTAPOV & CAMPBELL (1996) in simulation of single ball impacts against a surface. For the latter, it was possible to obtain a particle size distribution that was consistent with that from experiments, accurately predicting the size distribution for fragments larger than three element sizes.

POTAPOV & CAMPBELL (2000) also simulated breakage of an unconfined particle bed in two dimensions adopting a falling steel ball in an attempt to correlate breakage mechanisms found in ball mills, highlighting the great effect caused by the friction between particles in the energy dissipation of the contact and in the cohesion of the bed, impacting in a significant way the particle size distribution of the product. As for the application of the model in comminution equipment, the work of HERBST & POTAPOV (2004) can be cited, in which the simulations of a semi-autogenous mill and of a cone crusher were carried in an attempt to obtain a correlation between experimental and simulated particle size distributions.

More recently, OROZCO *et al.* (2019) studied the dynamic fracture of single particle impacts of elements discretized into polyhedral Voronoi cells, in an approach called bonded cell method (BCM), relating the amount of work to the loss of cohesion on the interface between cells. Damage and fragmentation efficiency were analyzed as a function of the impact energy and particle strength. It was found that breakage efficiency is related to the energy necessary to break the interface between cells and the impact energy, with stronger particles reaching maximum efficiency when subjected to higher impact energies. Figure 3.29 shows the evolution of a breakage event adopting a particle discretized into polyhedral cells.

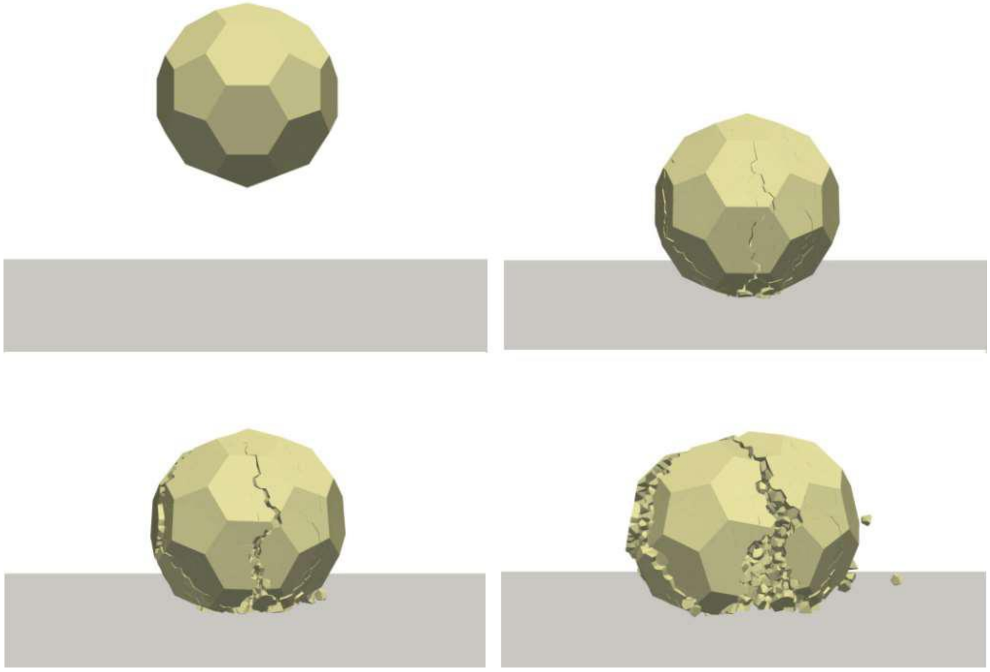

Figure 3.29 - Snapshots of a single particle impacting a surface using the model by OROZCO *et al.* (2019)

3.4.2.2. Breakage modeling adopting particle replacement scheme

The second group is represented by techniques in which the parent particle is replaced by its progenies that occupy geometrically the space of the parent particle every time a failure criterion is met. It is possible to highlight some approaches that use this particle replacement scheme to represent breakage in DEM. The approach that adopts spherical particles is named particle replacement model (PRM) and it was first proposed by CLEARY (2001). In this model, the particles, represented by spheres, are replaced by a set of progeny particles that occupy geometrically the space of the parent particle, as illustrated in Figure 3.30. The fragmentation of a particle will occur when it is subjected to stresses of magnitude higher than the critical tolerated limit by it and the particle size distribution will be determined based on the size distribution of the progeny particles. It is possible to note that, because it is a model that represents breakage instantaneously, if there is still energy remaining in the contact after the first breakage event, new fragmentation events may occur successively (CLEARY, 2001).

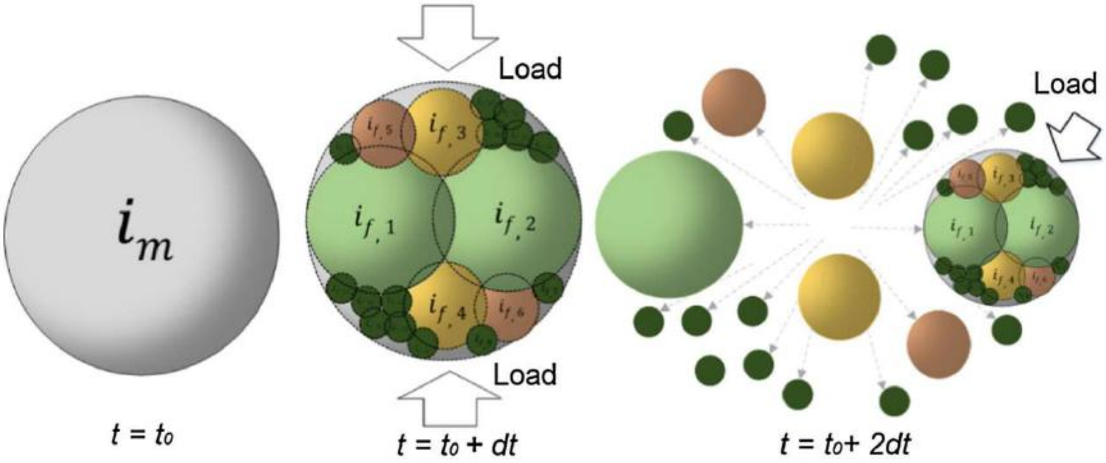

Figure 3.30 - Illustration of the particle replacement model (JIMÉNEZ-HERRERA *et al.*, 2018)

It is possible to find several works in the literature related to the use of PRM in comminution equipment, such as the recent works by CLEARY & SINNOTT (2015) and SINNOTT & CLEARY (2015), where crushers that work both through compressive stresses, such as jaw crusher, gyratory crusher, cone crusher and roll crusher, and through impact stresses, such as hammer crushers and vertical (VSI) and horizontal (HSI) shaft impact crushers, were simulated. The results demonstrated the feasibility of using this model to simulate the breakage with fairly good accuracy in predictions involving energy consumption, product size distribution, equipment flow and mantle and liner wear. In addition, BARRIOS & TAVARES (2016) simulated a high pressure grinding rolls (HPGR), obtaining a good relation between simulation results and flow prediction and energy performance models for the equipment.

The PRM can also adopt superquadric particles with rounded corners, as shown in Figure 3.31. This particle shape allows more realistic results to be obtained and minimization of mass loss after breakage due to better filling of the original particle volume. This approach was used in the works of DELANEY *et al.* (2015) and CLEARY *et al.* (2017) for simulations of industrial scale cone crushers and DELANEY *et al.* (2013) and CLEARY *et al.* (2018) for simulations involving autogenous and semi-autogenous mills, the latter incorporating models of damage accumulation, breakage probability and surface wear by abrasion in the predictions made using the PRM.

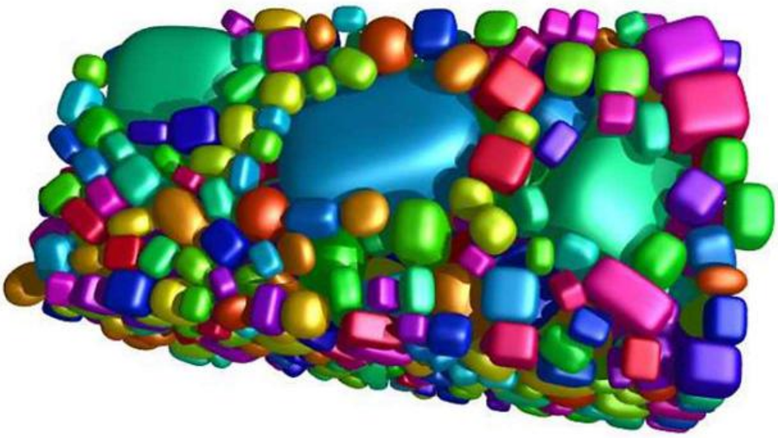

Figure 3.31 - Packing of progeny particles occupying the volume of a superquadric particle (DELANEY *et al.*, 2010)

As in BPM, the PRM presents as a limitation the inability to conserve volume after fragmentation of a particle. However, an artifice used in the PRM as a way to minimize volume loss consists of overlapping the progeny particles in the volume previously occupied by the parent particle or creating small progeny fragments and uniformly increase their size after being created.

Another approach using the particle replacement scheme but adopting polyhedral particles relates the intensity of the contact to the degree of particle fragmentation, as it occurs in the particle replacement model. In this approach, introduced by POTAPOV *et al.* (2007), the parent particles are replaced by a set of random polyhedral fragments when the stresses they undergo exceed a critical limit. As in DGB, the instantaneous breakage mechanism using polyhedral particles is able to conserve the mass and the volume of the parent particle, representing a great benefit when compared to the approaches that use spherical particles to represent breakage.

Regarding the use of the instantaneous breakage approach adopting polyhedral particles, it is possible to cite the work of LICHTER *et al.* (2009) in the simulation of different cone crushers, evaluating the values of flow, energy consumption and particle size distribution of the product. Another work that adopted this model was carried out by JIMÉNEZ-HERRERA *et al.* (2018), analyzing the results of breakage of a bed of particles obtained using the model implemented in version 3.11 of Rocky DEM software and comparing them with BPM and PRM models implemented in the EDEM software.

Unlike the approaches that adopt bonding elements, particle replacement schemes do not need to represent rigorously the internal mechanical properties of the particles, making it quite versatile in relation to the implementation of different breakage models available in the literature. JIMÉNEZ-HERRERA *et al.* (2018) state that this methodology allows the insertion of more complex models that take into account, for example, the variation of fracture energy of particle and the size distribution of the progeny particles according to the impact energy dissipated in the contact.

3.4.3. Rocky DEM

Rocky DEM is a discrete element method (DEM) modeling program for simulation of particles systems in three dimensions. Particle behavior and its interaction with other particles and boundaries can be set by adjusting simulation parameters. DEM simulators are useful for a wide range of applications in different areas. The software provides qualitative and quantitative results during and after processing a simulation on the basis of visual and numerical results of the simulated systems.

As a general purpose DEM software, Rocky DEM is useful to analyze particle flow and detect inefficiency on manufacturing design and processes, enhancing equipment life and capacity, reducing power draw, product degradation and minimizing dead zones and segregation. The software is also capable of predicting important information that may be useful in a post processing stage, including forces, torques and power consumption (ROCKY DEM, 2018). When describing particle breakage and weakening, Rocky DEM is able to predict particle flow more accurately, especially for equipment in which particle flow and particle size reduction cannot be decoupled.

The readily determination of the progeny size distribution allows the quick evaluation of a product and the fast improvement and optimization of the equipment. The size of each particle is determined instantly in Rocky DEM according to the largest size of the particle and its perpendicular size. Particle size will be based upon the dimensions of a square hole just big enough for the particle to pass through (ROCKY DEM, 2018).

Currently, two breakage models are available in Rocky DEM, each one with its own characteristics and formulas. Both models aim to predict particle breakage based on the stressing energy involved in particle collisions. Breakage is only available when adopting polyhedral particles, for that reason, no spherical, rounded or concave shapes can be used to simulate breakage in Rocky DEM (ROCKY DEM, 2018). The following sections of the present work will cover both breakage models in more details.

3.4.3.1. Ab-t_{10} model

The Ab-t_{10} model, based on equations proposed by the JKMRC to describe breakage, is able to represent body breakage of particles upon the stressing energy applied to them. This phenomenological approach can determine if breakage will occur based on parameters that govern the breakage probability of a material. The model also contains a description of particle weakening due to collisions that do not lead to particle breakage.

The model's equations were originally proposed by VOGEL & PEUKERT (2005) to describe breakage probability of particles of different materials and modified by SHI & KOJOVIC (2007) to predict the breakage index t_{10}. The original equation for breakage probability describes the variability of fracture energies of same size particles based on the Weibull distribution, according to the equation:

$$P(E) = 1 - \exp\{-f_{mat} d_i k (E - E_{\min})\} \tag{3.37}$$

where f_{mat} is a material breakage property, d_i is the representative initial particle size, k is the successive number of impacts with a single impact energy and E and E_{min} are, respectively, the specific impact energy of the contact and the specific threshold energy for a particle of size d_i, which has to be exceeded by E in order to cause particle breakage. E and E_{min} corresponds to the parameters $W_{m,kin}$ and $W_{m,min}$, respectively, originally proposed by VOGEL & PEUKERT (2005), while d_i corresponds to the parameter x of the original equation. According to the model, the value of the energy threshold $d_i E_{min}$ is size-independent and, alongside f_{mat}, comprise the only particle properties necessary to describe the material influence on the comminution result (VOGEL & PEUKERT, 2005).

The modification proposed by SHI & KOJOVIC (2007) to describe the breakage index t_{10} presents similarities in structure to the well-known equation proposed by the JKMRC to describe t_{10} as function of the specific impact energy, which is explained in more details in section 3.3.3. The model's equation is as follow:

$$t_{10}(E) = M\{1 - \exp[-f_{mat} d_i k (E - E_{\min})]\} \tag{3.38}$$

where M corresponds to the maximum t_{10} value in percentage of a material subject to breakage. A comparison between equations (3.38) and (3.22) reveals that M is equivalent to A, $f_{mat}d_i$ to b and $k(E - E_{\min})$ to E_{cs}.

The model as described by equations (3.37) (3.38) is able to predict breakage probability and t_{10} values for particles of a specific size d_i subjected to impacts of the same magnitude E. Few changes were necessary to adapt the model to a discrete environment, in which contacts can have different energies involved. Breakage probability and breakage index t_{10} can be determined using the Ab-t_{10} in Rocky DEM based on the following equations:

$$P(E) = 1 - \exp\left(-S(d_i/d_{i,ref})E_{cum}\right. \tag{3.39}$$

$$t_{10}(E) = M\left[1 - \exp\left(-S(d_i/d_{i,ref})E_{cum}\right]\right. \tag{3.40}$$

in which

$$E_{cum}^{new} = E_{cum}^{old} + \max\left(0, E - E_{min}\right) \tag{3.41}$$

$$E_{min} = E_{min,ref}\left(\frac{d_{i,ref}}{d_i}\right) \tag{3.42}$$

where $E_{min,ref}$ is the minimum specific energy for a reference particle size $d_{i,ref}$, S is the particle breakage strength parameter and E_{cum} is the cumulative energy of previous contacts. Just as in equations (3.37) and (3.38) , the product between $d_{i,ref}$ and $E_{min,ref}$ is a material constant. It is possible to notice that S is equivalent to $f_{mat}d_i$ and $k(E - E_{min})$ to E_{cum}.

The model has been tested in the description of breakage of particles in beds by impact using a falling steel ball (JIMÉNEZ-HERRERA *et al.*, 2018). The model described well the interaction of the ball and the particle bed but failed to predict the breakage probability and the progeny size distribution simultaneously. The equations implemented in the software lack degrees of freedom that allow the description of different properties using the same parameters.

3.4.3.2. Tavares breakage model

The Tavares breakage model, first implemented without validation in version 4.1 of Rocky DEM, comprises a set of equations also used to describe breakage in the UFRJ

Model, shown in more detail in section 3.3 of the present work. The model is able to describe body breakage of polyhedral particles when subjected to stresses of varied magnitudes. This phenomenological approach takes into account the energy dissipated in the contact between two elements to decide whether the particle will break or not. The model also considers the damage sustained by a particle subject to stresses of insufficient magnitude to promote particle breakage.

The model itself needed to be adjusted from a continuous to a discrete approach, where each particle will behave independently according to the stresses they are subject to. Few modifications in the models equations were necessary to adapt it to the discrete environment given by DEM. Regarding particles fracture energy, no further change was necessary and each new particle that is introduced in the simulation or is originated on a breakage event is assigned a random fracture energy based on the breakage probability distribution for that specific particle size, according to equations (3.7) and (3.8). The median value of the fracture energy distribution, E_{m50}, is determined based on equation (3.9), in which d_j can be interpreted as the size of the particle.

When the first contact that does not lead to breakage occurs and particles start to accumulate damage in a discretized environment, the fracture energy distribution of the original particles will no longer be represented by the lognormal distribution, since the fracture energy of each particle will vary based on the intensity of the contact they were subjected to. Due to that, equation (3.25) cannot be used to represent the distribution of fracture energy after particles start to accumulate damage. Besides that, equation (3.23) accounts for the total energy dissipated on a contact event before determining whether a particle will break or not. On a DEM simulation, however, the strain energy is detected at each timestep and breakage must occur instantaneously to ensure the correct reproduction of the motion of fragments, especially for particles subjected to longer contacts. Due to that, single particle breakage events must be described as a multiple-stage process and equation (3.23) becomes (CARVALHO, 2018)

$$t_{10} = A\left[1 - \exp\left(-b'\frac{E_{cs}}{E}\right)\right] \tag{3.43}$$

in which E is the specific fracture energy of a particle at the beginning of the contact and E_{cs} is the instantaneous loading energy, corresponding to a fraction of the kinetic energy of the elements ($E_{k,n}$), which is considered to be converted into strain energy. Every time E_{cs} reaches the value of E, the particle will break according to the equation:

$$t_{10} = A[1 - \exp(-b')] \tag{3.44}$$

The remaining energy of the contact will be used to promote breakage of the fragments originated on the first breakage event until its full dissipation. The corresponding t_n values will be estimated based on the incomplete beta function, described by equation (3.26). It is possible to observe, based on equation (3.44), that every breakage event of particles of the same material can be normalized into an identical progeny size distribution. As such, the model as adapted and implemented in Rock DEM uses the concept of primary normalized breakage function (SAEIDI *et al.*, 2016), which defines a constant material-specific size distribution resulting from each breakage event, as well as the concept of describing a single impact event as successive primary breakage events, as suggested by SAEIDI *et al.* (2016).

Numerical analysis of the proposed changes from equation (3.23) to equation (3.43) indicates that the adoption of the specific fracture energy of the particle as the denominator of the t_{10} equation instead of the median fracture energy of the broken particles results in a small overestimation of the values of t_{10}. Figure 3.32 compares the results for a population of 5,000 copper ore particles of 5.5 mm in size for both equations (3.23) and (3.43).

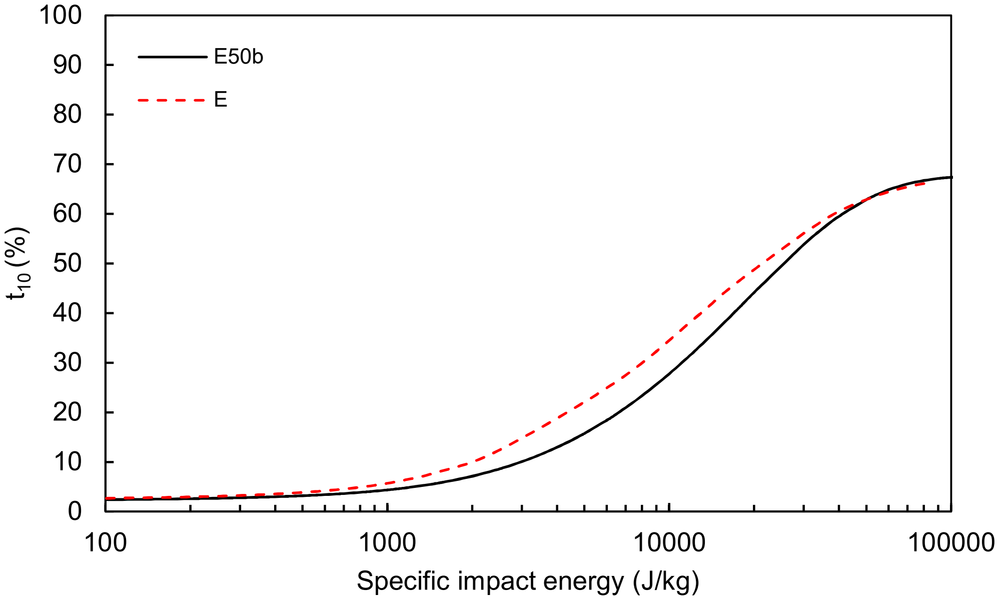

Figure 3.32 - Comparison between the analytical solutions of equations (3.23) and (3.43) for a population of 5,000 copper ore particles of 5.5 mm in size, presenting the tendency of overestimation when adopting the specific fracture energy of each particle to calculate the values of t_{10}

Low intensity impacts, on the other hand, are responsible for promoting changes in the internal structure of particles. The amount of damage sustained by a particle can be calculated after the contact ceases without breakage, which means that the instantaneous loading energy E_{cs} reached the value of the stressing energy $E_{k,n}$, based on equation (3.20). The new fracture energy will be calculated via equation (3.19). Figure 3.33 illustrates the calculation cycle of the Tavares breakage model on a DEM simulation.

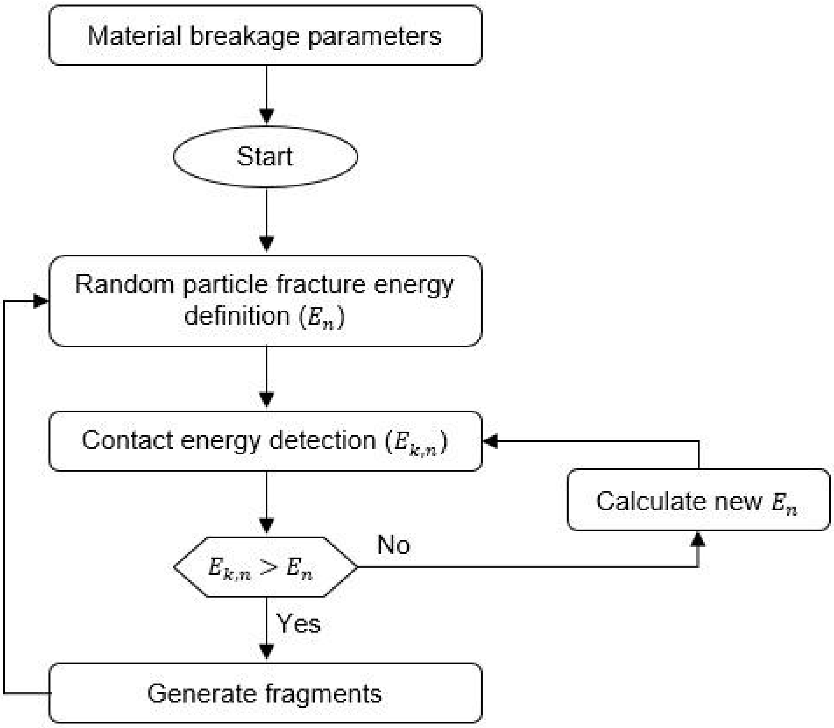

Figure 3.33 - Calculation cycle of the Tavares breakage model

The application of the model to mimic fracture energy distributions is quite straightforward in Rocky DEM. However, regarding damage prediction, a minimum specific energy parameter was necessary. This parameter is used to prevent the software from wasting time calculating damage for contact energies that are responsible for generating negligible damage and to indicate the end of a contact. When the contact energy drops below the minimum specific energy, the software understands that the contact has ceased, calculating the damage arising from the contact.

Regarding the progeny size distribution, two extra parameters were needed. The first one concerns the resolution of the final size distribution, which is the minimum size of particle that will be resolved in the simulation, hereinafter named minimum global size.

This parameter must be selected based on the computational power available and the necessary time to process a simulation. The second parameter is the minimum size of particle that will be generated in each breakage event, hereinafter named minimum breakage size and corresponding to a ratio of the original particle size. This parameter is used to guarantee that fine particles are only generated due to rebreakage of fragments, since the model represents particle breakage as a series of successive primary breakage events, avoiding overestimating fragmentation of a particle. At each breakage event, the fragmentation will follow the minimum breakage size only if its value is coarser than the minimum global size. Figure 3.34 illustrates how particle breakage is discretized into several breakage events on Rocky DEM. The time interval between the first and the last frame is of only 2 milliseconds.

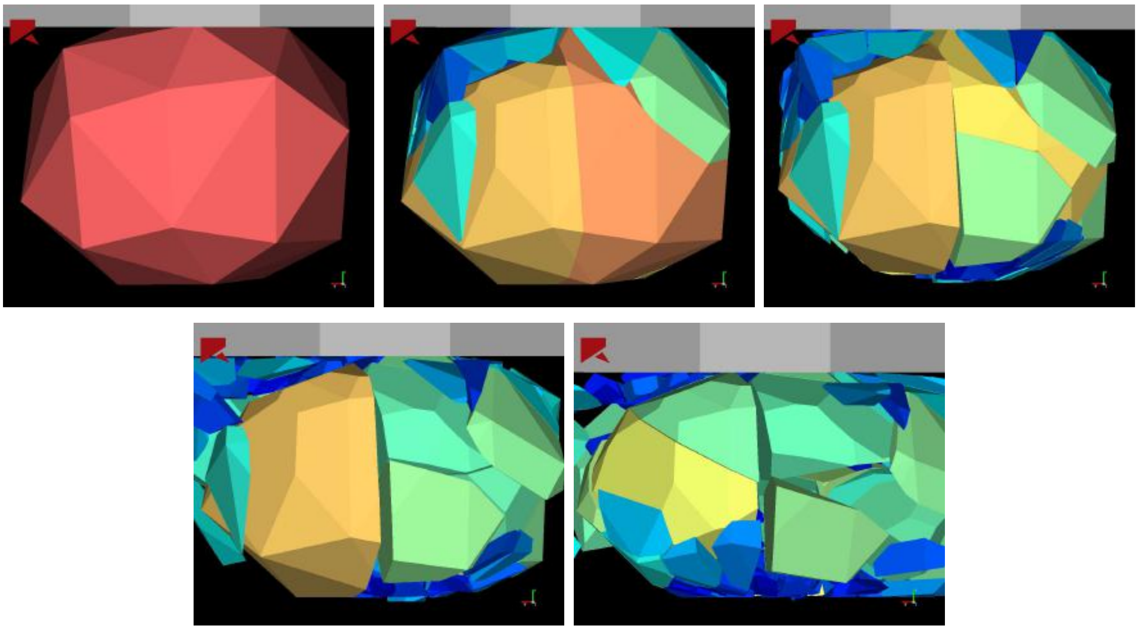

Figure 3.34 - Evolution of particle fragmentation in a drop weight test simulated in Rocky DEM, indicating that fine fragments are generated due to multiple rebreakage of particles being the time elapsed between the first and the last frame of 2e-03 s

The Tavares breakage model covers important rock behavior characteristics that are not considered in other breakage models available in the literature. The adoption of polyhedrons to represent particle shape in Rocky DEM also allows mass and volume conservation after a breakage event, overcoming many problems found in other breakage approaches available in the literature. Table 3.1 compares the Tavares breakage model to other existing breakage models, highlighting the benefits of using the model to describe breakage on a DEM environment. When the information concerning the characteristic was omitted in the publication, its presence was disregarded.

Table 3.1 - Comparison between the main DEM works adopting breakage on comminution equipment

Work	Variation of fracture energy among same size particles	Variation of specific fracture energy among different sizes	Damage accumulation	Representation of breakage as a multi-stage process	Description of progeny size directly related to impact energy	Adoption of non-spherical particles	Surface breakage due to abrasion	Mass conservation after breakage
LICHTER *et al.* (2009)				x	x	x		x
DELANEY *et al.* (2015)						x*		
CLEARY & SINNOTT (2015)		x	x					
BARRIOS & TAVARES (2016)		x						
CLEARY *et al.* (2017)						x*		
CLEARY *et al.* (2018)		x	x			x*	x	
Tavares breakage model	x	x	x	x	x	x		x

* Adopting super-quadric particle with smooth corners

3.4.3.3. Laguerre-Voronoi tessellation

When particles are subjected to impact energies that are intense enough to promote their breakage, the particle size distribution of the breakage event will be estimated based on the incomplete beta function to determine the passing proportions, i.e. t_n values, of different fractions of the original particle size accordingly with the value of t_{10} calculated via equation (3.44). The size of the fragments of the parent particle will be established using the Laguerre-Voronoi tessellation (ROCKY DEM, 2018).

The Laguerre-Voronoi tessellation is a tessellation method based on Voronoi diagrams (IMAI *et al.*, 1985). Voronoi tessellation techniques are widely used to represent cellular structures found in nature (WEJRZANOWSKI *et al.*, 2013), destructive environments in video games (GRÖNBERG, 2017), polycrystalline microstructures of metallurgical and ceramic materials (FALCO *et al.*, 2017), cellular coverage map (PORTELA & ALENCAR, 2008) and so on. The Voronoi diagram consists of a partitioning of a plane space into cells based on the distance between nuclei, in which the distance between each nucleus of consecutive cells to the border between them will be equal and all the points within a cell are closer to the generating nucleus than to any other nucleus (FALCO *et al.*, 2017). The method can be expressed mathematically as

$$\{C_{P_i}\} = \{x \in S^3 : \|P_i - x\| \leq \|P_j - x\|\} \quad \text{and} \quad j = 1, 2, \ldots, N : j \neq i \tag{3.45}$$

where S^3 is the metric space, P_j is the position of the nucleus, x is the position of a generic point in S^3 and C_{P_i} is the cell associated to the nucleus P_i, which is composed by the set of any point x whose distance to P_i is not greater than their distance to other nucleus P_j.

Voronoi tessellation techniques are useful to represent breakage because the generated cells are convex elements, which is recommended when used for collision detection (GRÖNBERG, 2017). However, most variations of the Voronoi tessellation algorithm does not provided the appropriate control over the size of the cells (FALCO *et al.*, 2017). The Laguerre-Voronoi tessellation, on the other hand, provides control over the size of the cells, allowing the reproduction of the grain structure of a wide range of materials (FALCO *et al.*, 2017). The Laguerre-Voronoi algorithm performs the tessellation based on a densely packed set of spheres of a pre-determined size distribution, allowing the generation of cells that are similar to the sphere size distribution (WEJRZANOWSKI *et al.*, 2013). It can be represented by a variation of equation (3.45), consisting of

$$\{C_{P_i}\} = \{x \in S^3 : \|P_i - x\| - r_i^2 \leq \|P_j - x\| - {r_j}^2\} \quad \text{and} \quad j = 1, 2, \ldots, N : j \neq i \tag{3.46}$$

in which r_i^2 is the weight associated to the nucleus P_i. It is possible to notice that if all the weights were equal, the Laguerre-Voronoi tessellation would behave like the original Voronoi tessellation. Figure 3.35 illustrates the subdivision of a cube into cells of different sizes based on the weight of each nucleus. In Rocky DEM, the diameter of the sphere used to generate the fragments using the Laguerre-Voronoi tessellation can be defined as twice the minimum distance between the particle center of gravity and the particle sides.

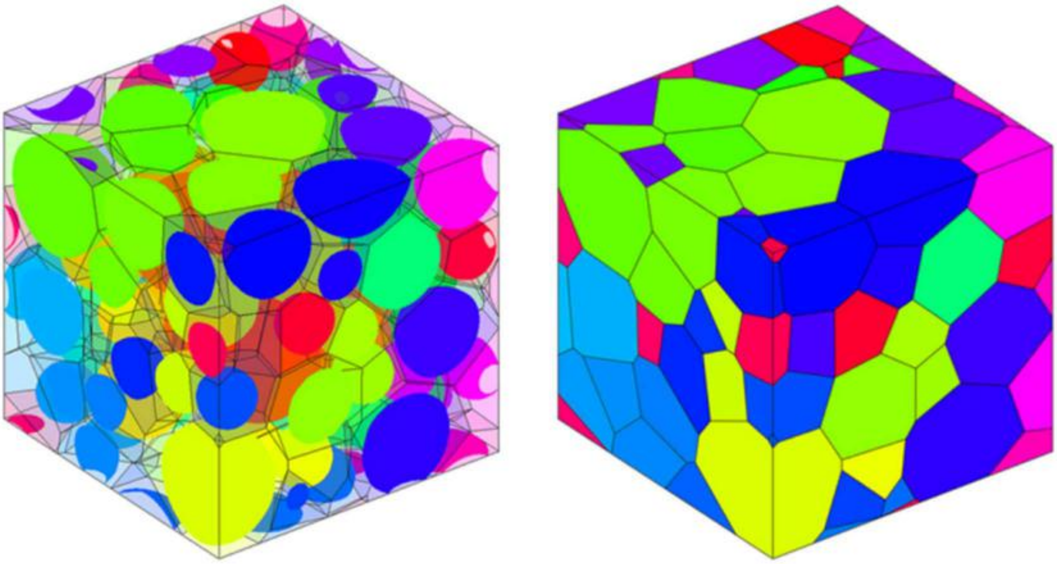

Figure 3.35 - Packing of spheres of different radii (left) and the Laguerre-Voronoi tessellation (right) (FALCO *et al.*, 2017)

The use of the Laguerre-Voronoi tessellation to represent breakage on DEM allows overcoming problems faced by other approaches that adopt the replacement of a parent particle by a set of progeny particles. The use of a cluster of overlapping particles to ensure mass conservation can lead to undesirable local pressure spikes, which may affect the contact force computation and the use of non-overlapping particles cannot guarantee mass conservation of the parent particle (COLA *et al.*, 2017). The Laguerre-Voronoi tessellation on polyhedral particles, differently, allows both mass conservation without the need of overlapping the fragments.

4. METHODOLOGY

This section will provide details concerning the materials adopted in the simulations and their parameters as well as the hardware and software specification used to run the simulations. The simulations were divided in three distinct stages: In the verification stage of the Tavares breakage model, simulations of single particle breakage tests were carried out to verify the fidelity of the DEM simulations in reproducing the results from the analytical model expressions. In the validation stage, the Tavares breakage model was used in simulations of more complex comminution systems and the results arising from simulations were compared to experimental data. Finally, the application stage proposes a useful utilization of the model in a comminution equipment.

4.1. Software and hardware

A developer version of the software Rocky DEM was used for all the simulations performed in the current work. During the verification stage, suggestions and modifications of the model's equations and operation were proposed in order to increase the fidelity in the breakage representation of the model. Different developer versions of the software Rocky DEM including the proposed modifications were released internally by the software developers for testing. Details of these changes are not the subject of this work and will not be presented. The validated version of the model is available in version 4.3 of the software Rocky DEM.

The hardware configuration used in the present work followed the recommended system requirements for using Rocky DEM software. An additional graphic processing unit (GPU) card was also used to process simulations due to the higher computational demand when adopting non-rounded shapes with breakage. Table 4.1 presents the configuration of the workstation used to perform the simulations.

Table 4.1 - Configuration of the workstation used to perform the simulations

Component	Specification
Operational system	Windows 10 Pro
Processor	Intel® Core™ i7-8700K CPU @ 3.70 GHz
RAM	32 GB DDR4 3200 MHz
Disk Space	480 GB SSD/4 TB HD
GPU card	Nvidia Titan V

4.2. Materials

Different materials were selected for both stages of this work according to their behavior when subjected to stresses. It was pre-determined that these materials should present different breakage responses, thus allowing to validate the model for a wide range of breakage strengths. The calibration of breakage parameters is not within the scope of this work and, because of that, parameters of four distinct ores that have been previously estimated on the basis of experimental data at the Laboratório de Tecnologia Mineral (LTM) were adopted. Table 4.2 presents the breakage parameters from the work of CARVALHO & TAVARES (2013) and BARRIOS *et al.* (2011) for the materials adopted in the simulations.

Table 4.2 - Summary of particles breakage parameters of the Tavares breakage model adopted in the simulations

Parameters	Copper ore	Granulite	Limestone #1	Limestone #2
E_∞ (J/kg)	213.5	130.7	7.0	150
d_o (mm)	8.073	1.10	100	0.79
φ	1.219	1.990	0.8	1.3
σ	0.799	0.903	0.801	0.600
$\alpha1.2/\beta1.2$	0.51/11.95	0.43/10.26	0.19/7.78	0.08/8.76
$\alpha1.5/\beta1.5$	1.07/13.87	0.92/10.74	0.56/7.51	0.56/7.48
$\alpha2/\beta2$	1.01/8.09	1.31/9.15	0.78/5.55	1.31/7.57
$\alpha4/\beta4$	1.08/3.03	1.18/2.97	1.12/3.01	1.21/3.03
$\alpha25/\beta25$	1.01/0.53	0.93/0.49	1.17/0.54	0.98/0.50
$\alpha50/\beta50$	1.03/0.36	0.92/0.39	1.43/0.40	0.98/0.31
$\alpha75/\beta75$	1.03/0.30	0.90/0.31	1.92/0.42	0.95/0.22
γ	5.0	5.4	5.4	5.0
A (%)	67.7	47.5	53.3	63.4
b'	0.029	0.027	0.033	0.033

According to equation (3.44) and parameters in Table 4.2, primary breakage of the four materials would result in values of t_{10} ranging from 1.3 to 2.1%. Applying the parameters of the incomplete beta function for each material based on the corresponding value of t_{10}, the primary breakage functions of the materials would have the appearance as presented in Figure 4.1, indicating that the incomplete beta function plays an important role in the determination of the particle size distribution, given the narrow range of t_{10} values.

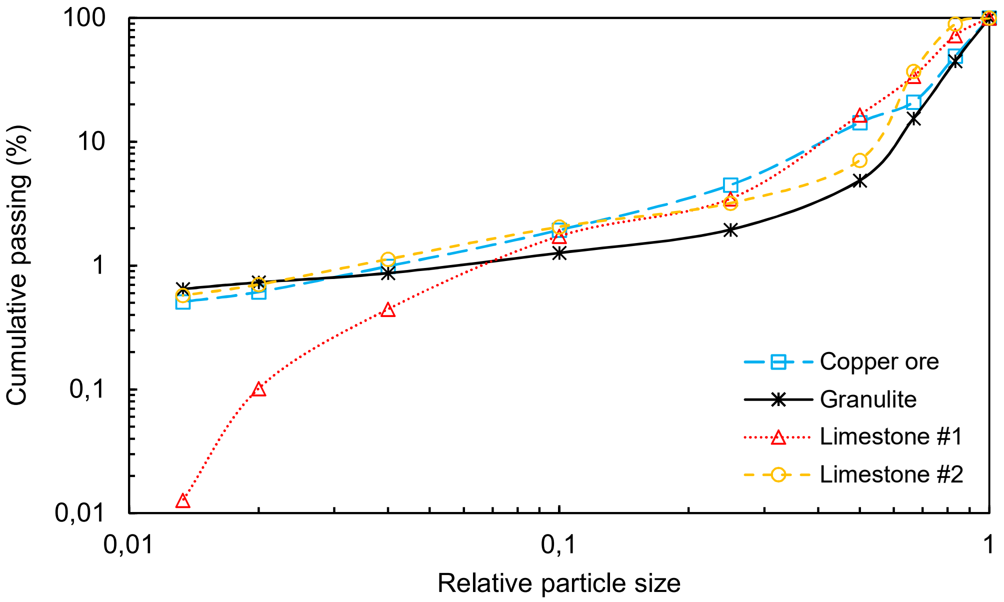

Figure 4.1 - Comparison of primary fragment size distributions given by the model for the four materials studied

It is important to highlight that the median fracture energy for each material will vary distinctively according to the size of the particles. Figure 4.2 compares the variations of median fracture energies for the different materials, demonstrating their significant differences. As expected, materials tend to present higher fracture energies at a finer particle size, however, the variation of fracture energy as a function of particle size will rely on the parameters of equation (3.9) listed in Table 4.2. Coarser particles of limestone #1, for example, tend to present an almost constant reduction rate on their fracture energy in the size interval studied, while for the other three materials the fracture energy of the particles reaches a minimum at a specific size.

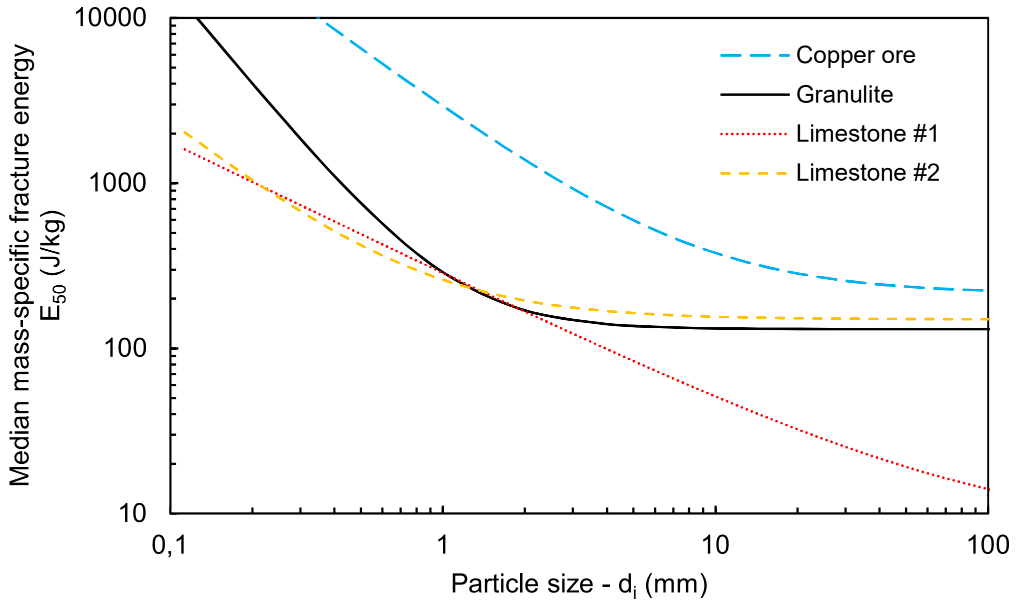

Figure 4.2 - Variation of median mass-specific fracture energies for the materials as a function of particle size

In section 3.4.3.2, the deviation between the predictions of the values of t_{10} of the original equation of the UFRJ model and the adapted equation for a discrete environment has been presented in Figure 3.32. This overestimation on the values of t_{10} when adopting the specific fracture energy of the particle can be further reduced by changing the value of the parameter b' after the calibration of the parameters of the model. Figure 4.3 presents the comparison of the predictions of t_{10} values for the equation (3.23) of the UFRJ model adopting the calibrated value of b' (0.0294) and different values of b' using the adapted equation (3.43) of the Tavares breakage model in Rocky DEM.

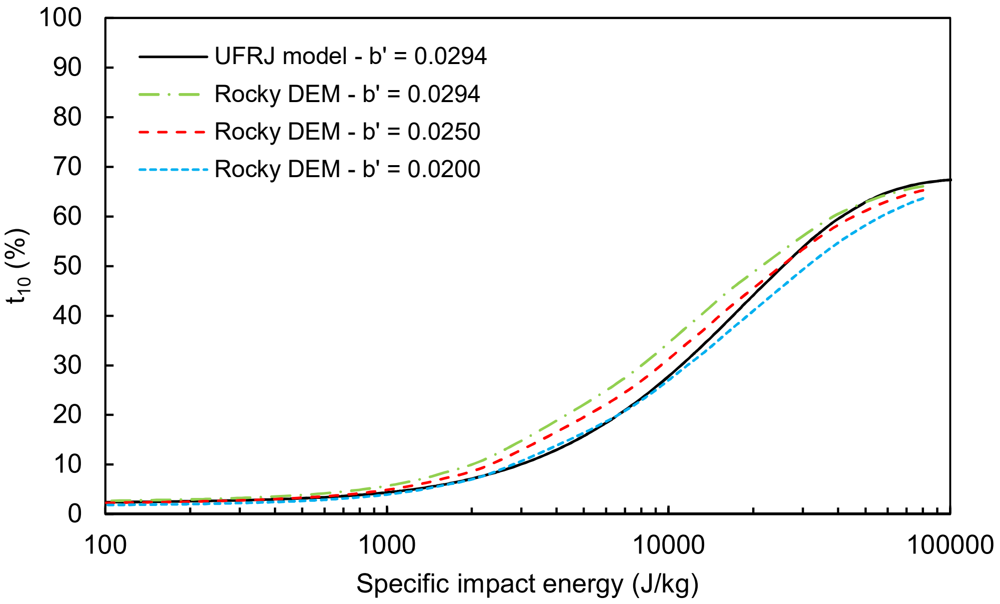

Figure 4.3 - Comparison between the predicted values of t_{10} using the original equation of the UFRJ model for a value of b' of 0.0294 and different values of b' using the adapted equation for a discrete approach in Rocky DEM

As it is possible to see, reducing the value of b' promoted a better agreement between analytical solutions of both equations (3.23) and (3.43) for the most common range of energy found in comminution equipment. Still, since the fineness of the progeny in Rocky DEM is highly influenced by the distribution of remaining energy of the contact on multiple breakage events, the effect of changing the value of b' presents low impact on the estimation of the values of t_{10}. For the present work, the parameter b' adopted in simulations will be the same as originally calibrated by CARVALHO & TAVARES (2013) and BARRIOS *et al.* (2011).

4.3. Simulation modeling

4.3.1. Verification stage

This section of the work will present the modeling of the simulations performed during the verification stage of the Tavares breakage model in a discrete environment using the software Rocky DEM. Simulations of several breakage tests and comparison between their results to analytical solutions of the model's equations adopting the same calibrated parameters were performed. Simulated materials were assessed based on their response to breakage probability, damage accumulation due to repeated impacts and particle fragmentation.

4.3.1.1. Single and double impact tests

Single impact tests were performed by propelling particles against a steel plate at different velocities to represent a wide range of collision energies. Double impact tests were simulated by using drop weight tests (DWT) with flat-ended cylindrical weights, so as to simulate the standard JKDWT (NAPIER-MUNN *et al.*, 1996). Different impact energies were achieved by changing the drop height and the mass of the falling cylinder. Figure 4.4 shows the setup adopted for the simulation of both tests, which illustrates batches of 48 particles subjected to simulations under each condition.

To verify the model's response to breakage probability of a population of particles, 576 and 288 particles were subjected to single and double impacts, respectively. In addition, the verification of particle fragment size distribution was performed using 96 particles under double impact conditions.

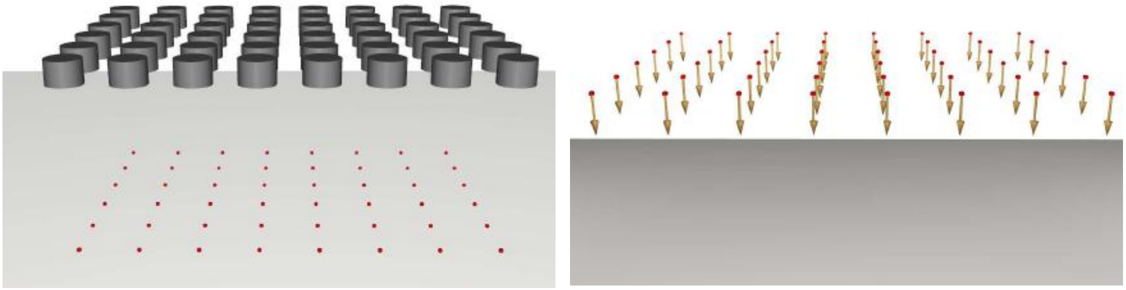

Figure 4.4 - Simulation setup for drop weight tests (left) and single impact tests (right). Particles are shown in red

Particle weakening by damage accrual was assessed in simulations of 20 repeated drops of 100 particles against a steel plate by counting the number of broken particles after each impact. Drops from a preselected height were simulated and, as soon as all particles were resting on the steel plate, this was removed from the simulation, allowing another identical drop being simulated. Enough time was given between each drop to ensure that all particles were resting on the surface, avoiding particles from falling from different heights. On a post processing stage, all contacts besides the first contact between the particle and the steel surface were considered negligible and were disregarded when evaluating the model's predictions. Figure 4.5 presents the apparatus adopted to perform the simulation of particle weakening and frames from different impacts. As it is possible to notice, the number of original size particles, which are represented in red, decreases after several impacts, indicating that more particles have broken after repeated impacts.

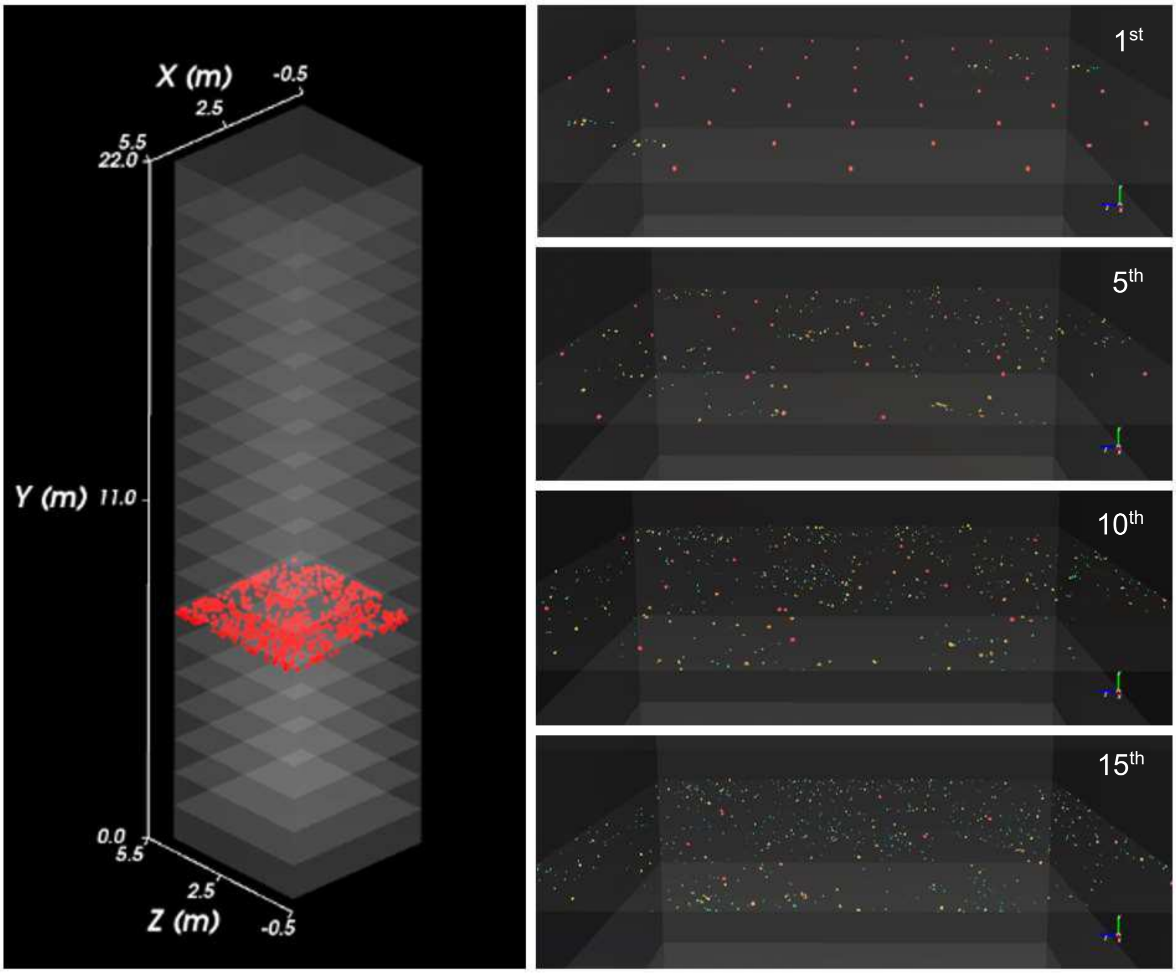

Figure 4.5 - Simulation setup for the damage accumulation test consisting of 20 consecutive drops of same height (left) and frames from different impacts (right). The corresponding impact number is presented in each frame

4.3.2. Validation stage

The validation stage of the Tavares breakage model in the discrete environment given by Rocky DEM proceed the verification stage of the model and had the purposed of validating data from simulations of comminution tests and equipment against experimental results. This section of the work will present the modeling of the simulations performed during the validation stage of the Tavares breakage model for different comminution tests and equipment.

4.3.2.1. Unconfined particle bed breakage tests

Unconfined particle bed breakage tests were performed adopting a steel ball with 88 mm in diameter and 2.78 kg in weight. Different configurations of the bed were tested by incrementing the number of circles around a central particle, according to 3.2.2, as well as different impact energies by varying the drop height and the mass of the falling ball. Simulations were run in quadruplicates and the average results were adopted in the comparison with experimental data. Results were assessed based on capture radius of the steel ball, broken mass of the bed and particle size distribution of the product. Figure 4.6 compares the simulation setup with the one adopted in experiments.

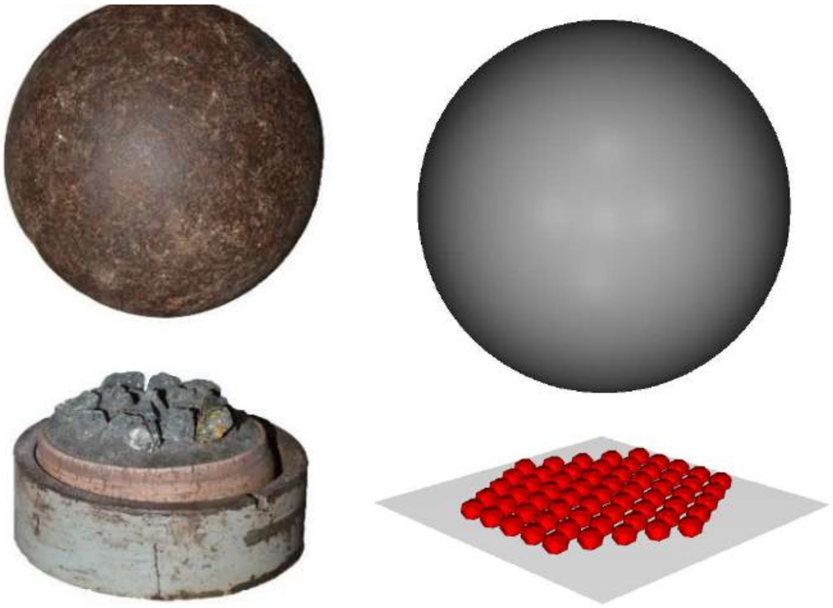

Figure 4.6 - Exemplification of the setups adopted in experiments (left) and simulations (right)

Same size particles were adopted in simulations of bed breakage. Particle sizes were chosen based on the average particle mass of the experiments for each material, respecting the size range of 6.3 to 4.75 mm and avoiding introducing discrepancies in the total mass of the bed from experiments. Particles were evenly distributed based on the size of beds observed experimentally to ensure repeatability of capture radii of experiments. The maximum radius observed in experiments was 65 mm for tests involving monolayers of particles. Bed arrangements using 1, 2, 3 and 4 (monolayer) rings were tested as well as three and five layers of particles, as show in Figure 4.7. In simulations involving three and five layers of particles, a hexagonal geometry was placed around the particles, so as to mimic the effect of the paper ribbon in experiments. This geometry was removed 0.005 s before the contact, granting the unconfined condition of the bed and causing no additional influence on the simulated results besides preventing the bed from falling apart.

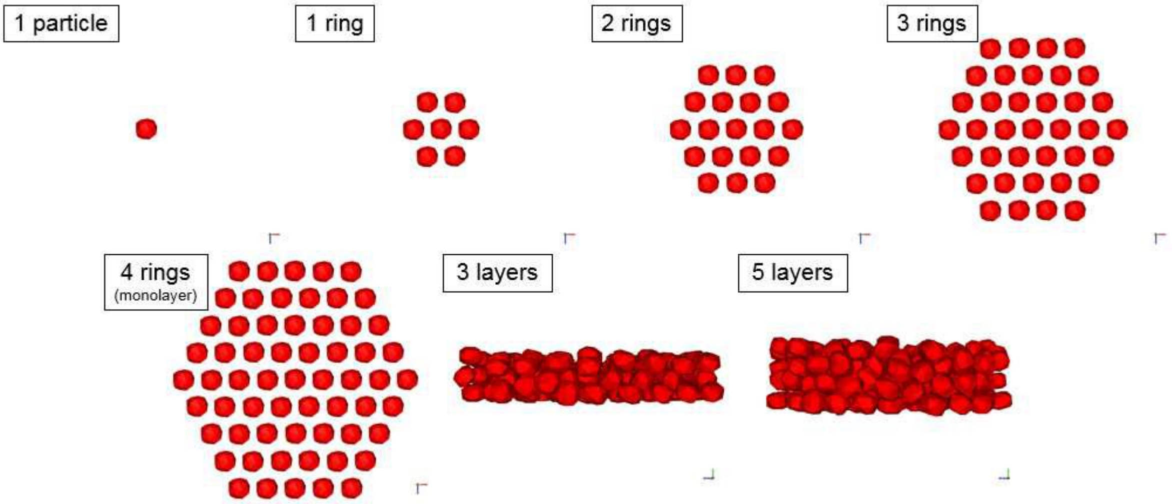

Figure 4.7 - Different bed arrangements of copper ore particles of 6.1 mm in size tested in unconfined bed breakage tests

4.3.2.2. Laboratory cone crusher

Crushing simulations were performed using a laboratory scale shorthead cone crusher (Denver No. 12). The crusher in question was modeled using the computer aided design tool AutoCAD and presents a feed opening gap of 25 mm, a stroke of 0.5 mm, a cone angle in relation to horizontal of 46º and a mantle length of 150 mm. Operating conditions for the crusher followed the ones adopted in experiments, with a closed-side setting of 5.0 mm and the frequency of the crusher bowl of 616 rpm. The throughput of the crusher was analyzed during the entire simulation to ensure the crusher was running in steady-state condition before sampling the results. Choke-feed conditions were achieved by filling the feeder of the crusher before starting its operation. Simulations were assessed based on the flow rate, particle size distribution of product, power draw and specific power consumption. Figure 4.8 compares the modeled crusher with the real laboratory cone crusher, while Figure 4.9 presents a cutaway view of the crusher.

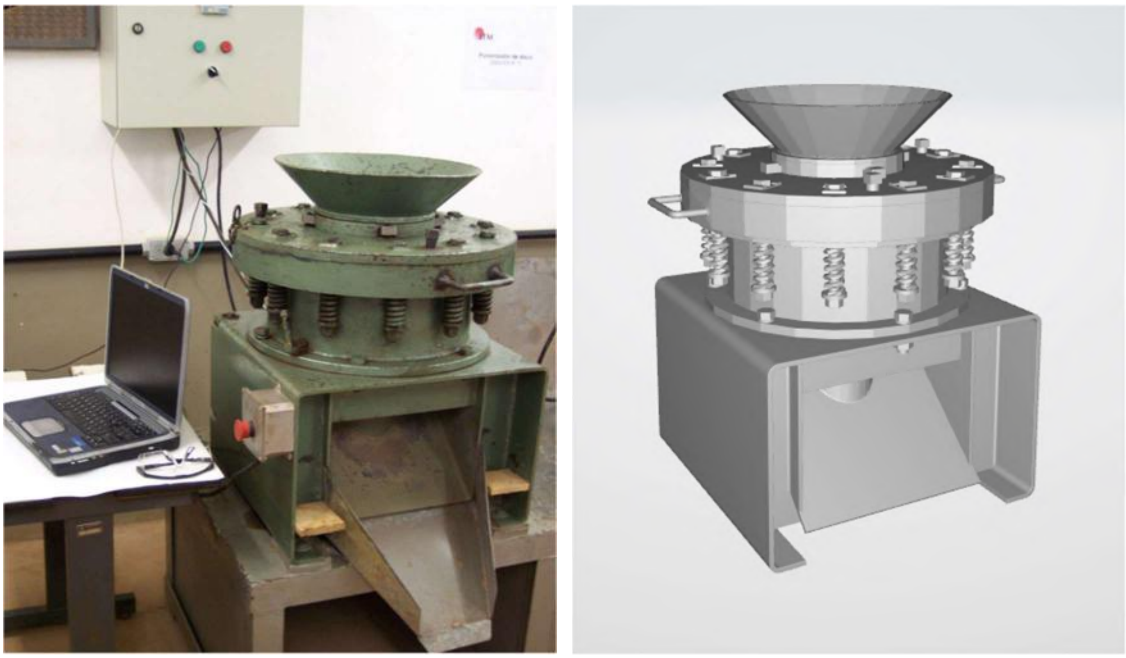

Figure 4.8 - Laboratory-scale cone crusher used in experiments (left) (MAGALHÃES & TAVARES, 2014) and modeled version adopted in simulations (right)

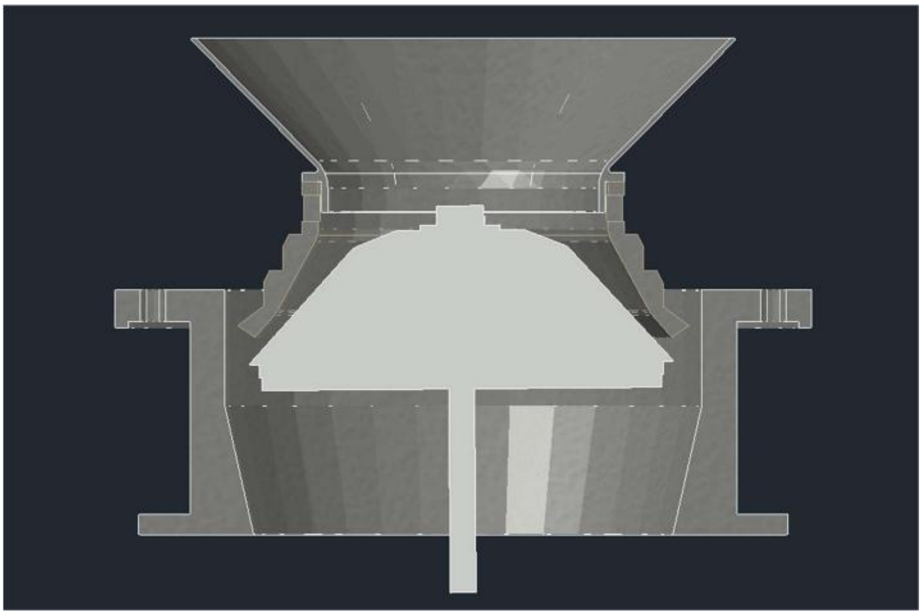

Figure 4.9 - Cutaway view of the laboratory-scale cone crusher adopted in simulations of the validation stage

Feed particle sizes evenly distributed and ranging from 16 mm to 22.4 mm were chosen to mimic the one used in all experiments. Choke-feed condition of the crusher was achieved by adopting a feed flow rate higher than the expected throughput.

The information required to represent the movement of the crusher mantle in simulations using Rocky DEM was not readily available. Therefore, it was necessary to perform measurement of the operating conditions of the crusher to get the appropriate data. Since the movement of the cone is repeated several times during the simulation, modeling of the crushing operation was carefully examined in order to avoid accumulating errors of any kind during the simulations, which could lead to biased results.

The eccentric throw of the cone in relation to a horizontal plane was measured using modeling clay and its inclination was achieved using a clinometer. The values of 1.5 mm and 0.5° were achieved, respectively. The pivot point, which corresponds to the point that the shaft of the cone will pivot around, was determined using trigonometry and it is positioned 171.8 mm below the base of the cone in the vertical axis. The measured values were validated against animations provided by the motion preview tool available in Rocky DEM, as presented in Figure 4.10. The same approach was adopted to identify if simulations were presenting the expected values of CSS and OSS, as illustrated in Figure 4.11.

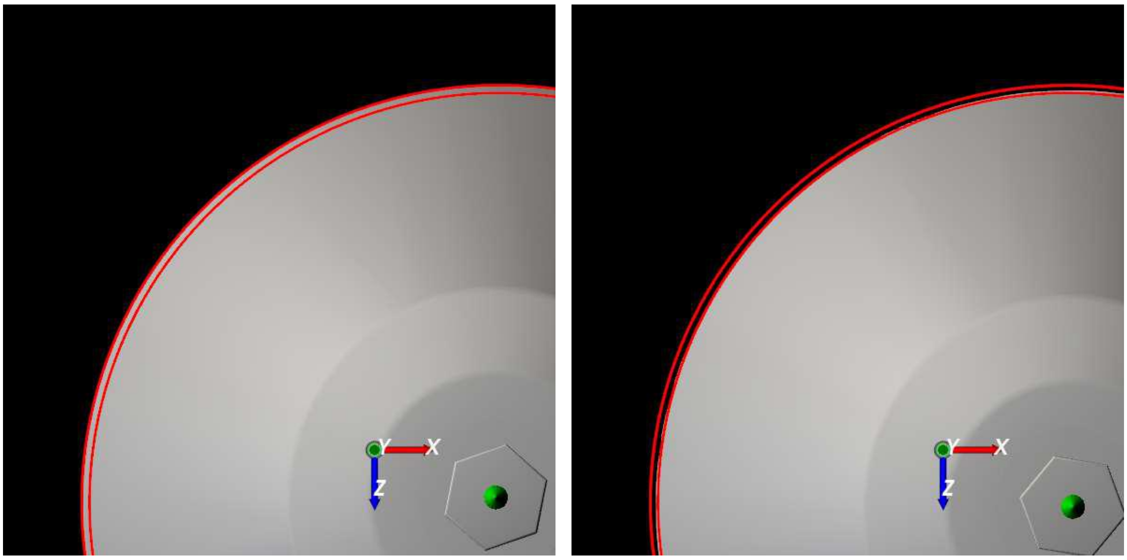

Figure 4.10 - Horizontal motion of the cone in simulations in parallel view. The red lines represents the maximum displacements measured in laboratory cone crusher (top view of the cone)

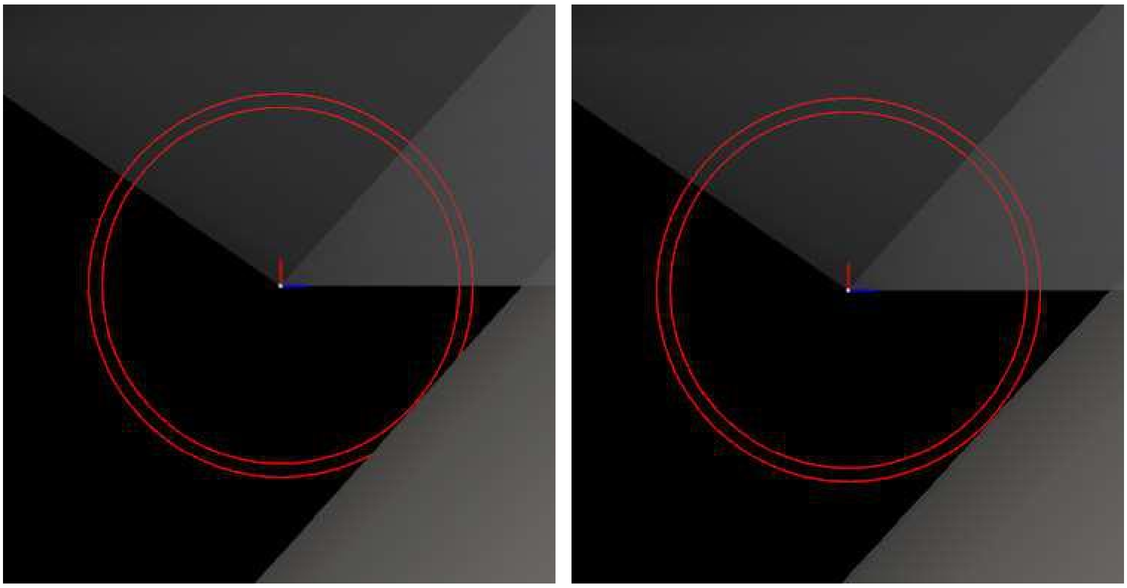

Figure 4.11 - Illustration of a parallel view of the closed-sized setting of 5.0 mm, represented by the internal red circle (left) and the open-sized setting of 5.5 mm, represented by the external red circle (right)

In order to create the motion frame of the cone crusher in Rocky DEM, the user must inform the coordinates of the pivot point from the origin, the rotation axis of the cone, the rotational velocity and the initial orientation of the cone, which corresponds to sine and the cosine of the inclination angle of the cone.

In Rocky DEM, the motion frame of the bowl crusher is defined as a free body rotation motion, which means that the cone is free to rotate around its axis but can be prevented from that due to torques arising from the contact between the mantle of the cone and particles, just as observed in reality. In order to get accurate results regarding the rotation motion of the cone, it is necessary to input in the simulator the mass of the cone, its center of gravity in relation to the origin and the moment of inertia for each axis. Default parameters available in Rocky DEM, which are meant to be used for industrial-scale crushers, to describe motion of a laboratory crusher will likely overestimate the moment of inertia, preventing the mantle from reaching a steady-state condition.

The volume of the cone and its center of gravity were determined using the software MeshLab whereas the mass of the cone was estimated based on its volume and considering it as a solid geometry made of steel. The moment of inertia for the vertical axis was achieved considering a cone radius of 163.9 mm. Table 4.3 shows the mass parameters of the cone geometry.

Table 4.3 - Mass parameters of the cone geometry

Parameter	Units	Values
Volume	cm³	6222
Mass	kg	48.53
Moment of inertia	kg.m²	1.304

4.3.3. Application stage

The application stage of the Tavares breakage model using Rocky DEM platform has the purpose of presenting another potential application of the model. In this section, simulated results were not compared to experimental data and more focus was given in providing a clear understanding of the benefits of using the Tavares breakage model to simulate comminution processes. This section of the work will present the modeling of the simulations performed to outline a process optimization solely by adopting characteristics of the ore described by the model.

4.3.3.1. Pilot horizontal shaft impact crusher

Crushing simulations were performed in a pilot scale horizontal shaft impact (HSI) crusher. The crusher was modeled using the 3D modeling software SketchUp® (TRIMBLE, 2016) and presents a width of 0.52 m, a crushing chamber of 0.84 m in diameter, a rectangular feed opening of 0.25 m by 0.33 m and a rotor of 0.70 m in diameter with four hollow blow bars. Particles capture by the gyratory bars are projected against five aprons positioned at different heights. The discharge of the crusher is made through a grate positioned at its bottom. The feed particle size distribution ranged from 16 mm to 22.4 mm and 5 t/h of ore was fed through an inlet positioned at the feed opening of the crusher. Figure 4.12 illustrates the modeled crusher adopted in the simulations.

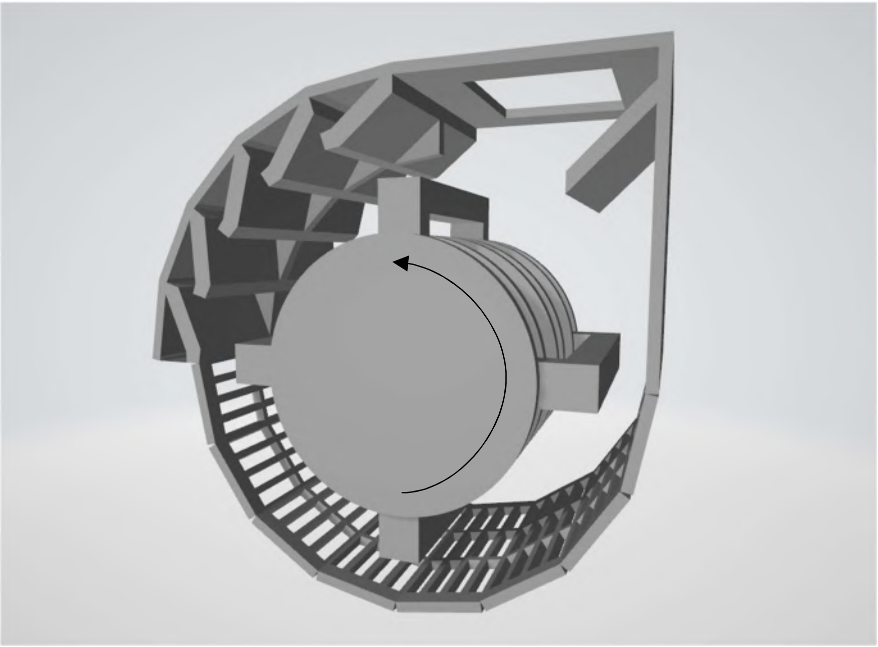

Figure 4.12 - Modeled horizontal shaft impact crusher used in simulations. The black arrow indicates the direction of rotation

Simulations performed during the application stage had the main purpose of describing selective crushing at different rotational velocities of the rotor when feeding the crusher with two distinct materials. Due to that, the grate at the bottom of the crusher did not have the function of classifying the fines and retaining oversize particles for further impacts. Instead an opening large enough to pass the coarsest size in the feed was needed. To reduce the processing time, the geometry of the grate was deactivated during the simulation, being presented only for illustrative purposes.

4.3.4. Contact modeling

The contact models adopted in all simulations were the hysteretic linear spring model for the normal component of the force and the linear spring Coulomb limit for the tangential component of the force. Table 4.4 presents the contact parameters adopted. Since this work is more focused in presenting the Tavares breakage model and perform its preliminary validation, no special attention was given to calibrating these parameters, so that default and recommended parameters were used. This was considered a valid approximation, in spite of their different characteristics.

Table 4.4 - Contact parameters adopted in the simulations to verify the Tavares breakage model

Parameter	Type of contact		
	Ore/Ore	Ore/Steel	Steel/Steel
Static friction	0.8	0.5	0.3
Dynamic friction	0.8	0.5	0.3
Tangential stiffness ratio	1	1	1
Restitution coefficient	0.3	0.3	0.3

4.3.5. Particle parameters

Particle parameters were chosen based on the real properties of the selected materials as well as previous observations based on calibration tests. Table 4.5 presents the values adopted for density and bulk Young's modulus for different materials used in the simulations. The Young's modulus of 5e+08 N/m² for different types of ores was the minimum necessary to achieve optimal accuracy in breakage probability results. Still, results adopting the Young's modulus of 1e+08 N/m² for ore particles returned fairly reasonable results, especially considering the faster processing time of the simulations. During the validation stage, different Young's modulus were used according to the scenario being simulated.

Table 4.5 - Particles parameters adopted in the simulations to verify the Tavares breakage model

Parameters	Values				
	Copper ore	Granulite	Limestone #1	Limestone #2	Steel
Density (kg/m³)	2930	2790	2710	2980	7800
Bulk Young's modulus (N/m²)	5e+08	5e+08	5e+08	5e+08	1e+11

To ensure proper division of energy among the elements involved in a contact, according to equation (3.31), the bulk Young's modulus of steel must be at least 10 times higher than the bulk Young's modulus of the ore. The adoption of the same Young's modulus for both ore and steel would split the energy involved in a collision equally, severely underestimating the energy absorbed by the particle (TAVARES & CARVALHO, 2012). The bulk Young's modulus of 1e+11 N/m² for steel was set to avoid rearranging of particle during the verification stage of this work using single particle breakage tests, enhancing breakage probability. However, the Young's modulus of 5e+09 N/m² for the steel was used throughout the validation stage of the model. For crushing simulations adopting the laboratory scale cone crusher, the Young's modulus of 1e+08 N/m² was adopted for ore particles, whereas the Young's modulus of 1e+09 N/m² was used for the steel boundaries, whereas for simulations of the HIS, the Young's moduli adopted followed the ones adopted in simulations of unconfined breakage bed tests.

4.3.6. Particle shape

The geometry of the particle was chosen in order to mimic the shape of a real particle. To avoid introducing discrepancy beyond material properties, the same particle shape were used for different materials. Table 4.6 presents the parameters adopted to define the particle one type of particle shape used in all the simulations of the present work, while Figure 4.13 illustrates the modeled particle.

Table 4.6 - Parameters adopted to model the particle shape used in simulations

Parameter	Particle #1
Vertical aspect ratio	0.8
Horizontal aspect ratio	1.0
Number of corners	25
Superquadric degree	3.0

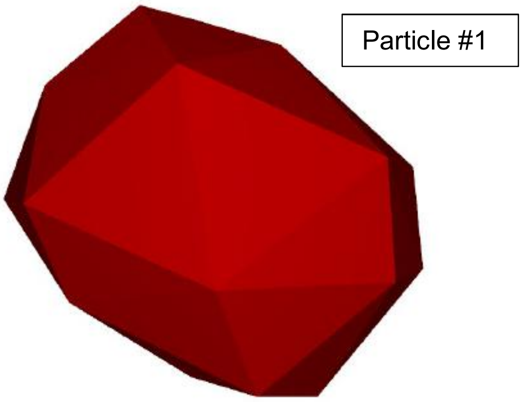

Figure 4.13 - Particle shape adopted throughout the simulations

However, adopting only one particle shape in crushing simulations using the laboratory cone crusher would not provide appropriate packing of particles inside the chamber of the crusher. Due to that, three other particles shapes ranging from a very spherical shape to a very angular shape were used in simulations. The parameters adopted to define the additional particle shapes used in crushing simulations are presented in Table 4.7. Figure 4.14 illustrates the additional particle shapes used in cone crusher simulations.

Table 4.7 - Additional particle shapes adopted in crushing simulations

Parameter	Particle #2	Particle #3	Particle #4
Vertical aspect ratio	0.5	0.7	1.0
Horizontal aspect ratio	0.8	1.2	1.0
Number of corners	20	25	20
Superquadric degree	4.0	2.3	2.0

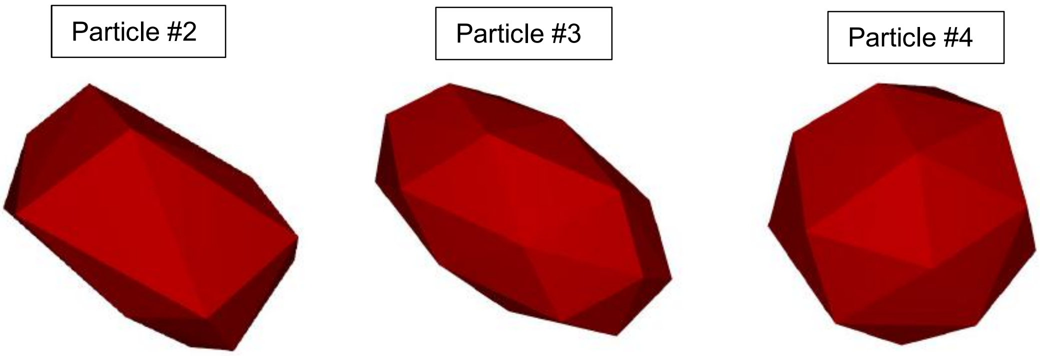

Figure 4.14 - Additional particle shapes adopted for crushing simulations

4.3.7. Rocky DEM solver parameters

Selecting the appropriate solver parameters is an important part of preparation of a simulation as they will directly influence the desired output. In Rocky DEM, the timestep duration is defined by the particle size, density, Young’s modulus and restitution coefficients chosen for each material and also the solver parameter “Loading N-Steps”, which corresponds to the amount of timestep intervals during the loading phase of a contact (ROCKY DEM, 2018). Lower values of the “Loading N-Steps” will increase the timestep duration at a cost of generating more unstable results. For all the simulations performed, the default value of 15 was adopted for this parameter. It is important to highlight that the duration of each timestep is calculated automatically by the software and that, after a breakage event, the software dynamically adjusts the timestep duration so as to consider the generation of finer particles. Therefore, all the timestep durations reported in the present work correspond to the value before any breakage event. Changes on the duration of the timestep are not available for users at the current version of Rocky DEM.

The “Breakage Overlap Factor” located in the advanced tab of the solver parameter determines that particles will break when their overlap with the contacting boundary reaches the value of this factor multiplied by the minimum particle size assigned for the material of the corresponding particle, even if the current energy is not enough for the particle to break (ROCKY DEM, 2018). This parameter is useful to avoid fragment generation on the other side of a boundary due to the low stiffness of a contact associated with a large overlap between the elements. The “Breakage Overlap Factor” parameter was disabled for all the simulations performed, allowing particles to break at their corresponding fracture energy.

5. RESULTS AND DISCUSSION

5.1. Verification stage

5.1.1. Simulations of breakage probability

The model's response to breakage probability of particles of different materials when subjected to single and double impact collisions was evaluated. The simulations also included different particle sizes of the same material in order to verify if the model was able to predict correctly the variation of fracture energy according to the size of the particle. Simulations of both impact tests for five different contacts energies adopting particles of 5.5 mm in size, comprising the size range of 4.75 to 6.30 mm, were performed for the four materials listed on Table 4.2. To verify the model's response to the variation in particle size, additional testing of 2 mm copper ore particles, comprising the sizes between 1.70 to 2.36 mm, and 28.9 mm, which corresponds to particles retained in a size class of 26.5 to 31.5 mm, were also simulated for both stressing conditions.

The minimum global size allowed in simulations was 1/10th of the original particle size, which corresponded to 0.2 mm for simulations involving particles of 2 mm in size, 0.55 mm for simulation of particles of 5.5 mm and 2.89 mm for the simulations fed with particles of 28.9 mm. As discussed in 4.3.1, in order to ensure representativeness of the results, 576 particles and 288 particles were simulated for single impact tests and double impact tests, respectively. Table 5.1 presents the timestep duration for each simulated scenario. As expected, shorter timesteps are necessary when processing finer particles. Besides that, changing the Young's modulus from 5e+09 to 1e+11 N/m² did not affect the duration of the timestep for single impact tests but slightly reduced the duration of the timestep for all the simulations of DWT, except for the ones with copper ore particles of 2 mm and 5.5 mm.

Table 5.1 - Timestep duration for each simulation performed during the verification stage

Material	Particle Size (mm)	Timestep duration (s)	
		Single Impact	DWT
Copper ore	2.0	3.03e-07	3.03e-07
	5.5	8.29e-07	8.29e-07
	28.9	4.38e-06	3.47e-06
Granulite	5.5	8.09e-07	6.35e-07
Limestone #1	5.5	7.98e-07	6.35e-07
Limestone #2	5.5	8.36e-07	6.35e-07

The ability of the model to discriminate different materials is illustrated in Figure 5.1, which shows that both the analytical model and simulations were sensitive to changes in median fracture energies and variances in the distribution.

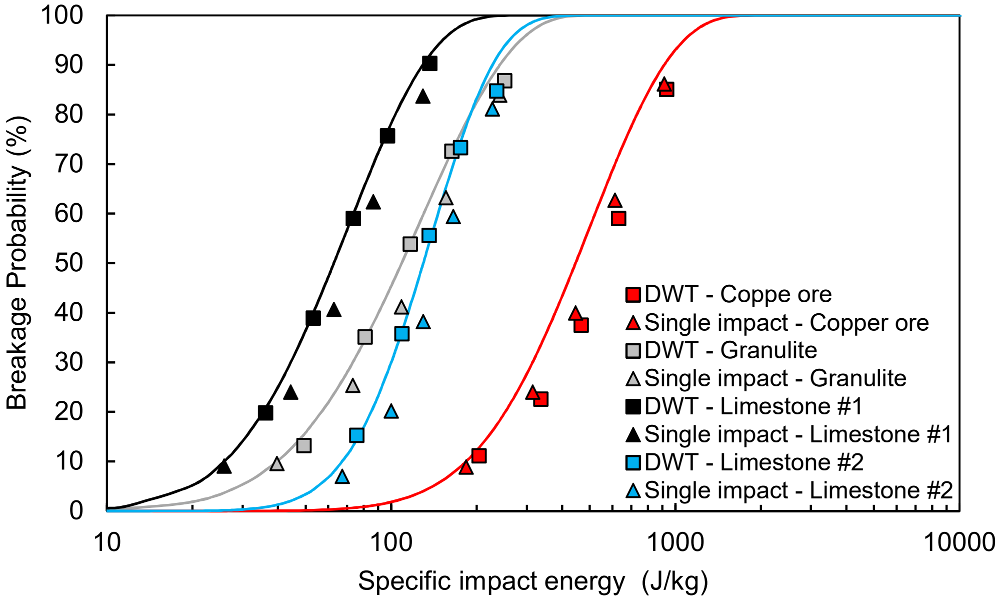

Figure 5.1 - Comparison between the modeled (lines) and simulated (symbols) breakage probabilities for drop weight tests and single impact tests of 5.5 mm particles of different materials

Additional tests using copper ore particles of different sizes were also simulated. Figure 5.2 presents the breakage probability results for these tests. It is noticeable from the results of Figure 5.1 and Figure 5.2 that DEM simulations captured well the variation of breakage probability distributions among the materials and particle sizes studied, presenting a small underestimation in comparison to the analytical model. It is also evident that simulations did not discriminate between single and double (DWT) impacts. The fact that simulations do not discriminate between these two modes of stressing, however, does not mean that differences do not exist in practice. In the review by TAVARES (2007) it was observed that differences can appear in breakage probability distributions associated to the number of points of application of stresses, but no clear understanding yet exists that would allow incorporating this effect in the model and simulations. As such, the breakage model as simulated in DEM assumes that the mode of stresses simulated is the same as the one used in fitting the various parameters in the model.

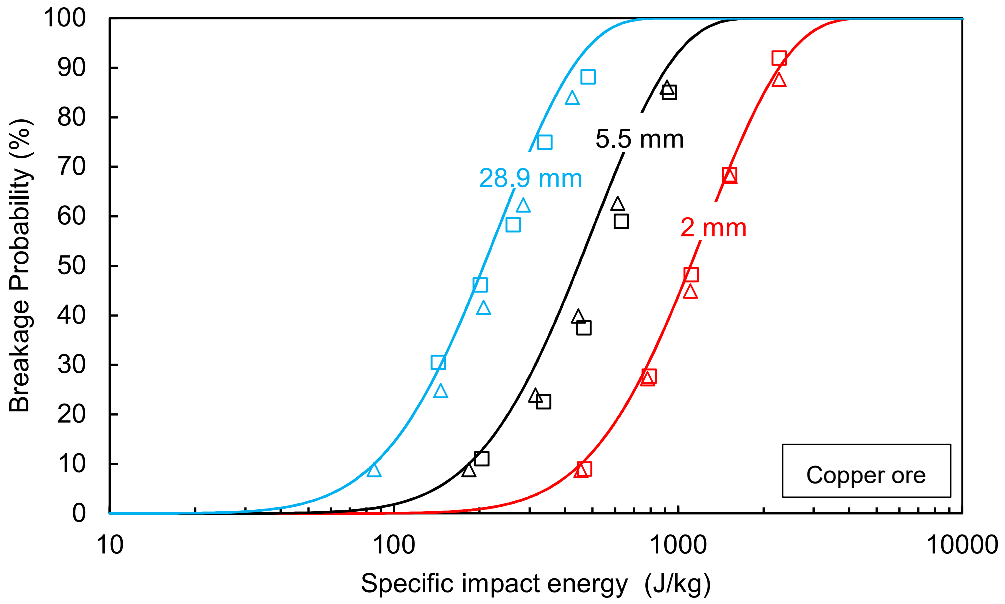

Figure 5.2 - Comparison between the modeled (lines) and simulated (symbols) breakage probabilities for drop weight tests and single impact tests of copper ore particles of different sizes (triangles are single impact and squares, drop weight test simulations)

5.1.2. Simulations of particle fragmentation

The drop weight test setup was adopted to assess the model's response to particle fragmentation. The materials were tested for different contact energies based on the drop height of the weight. Simulations of a set of 96 particles subjected to nine different contact energies varying from low to high magnitudes were performed for each material. The simulations adopted particles of 5.5 mm in size of the four materials listed in Table 4.2 and copper ore particles of 28.9 mm. The minimum global size adopted for simulations, as well as for individual breakage events, involving particles of 5.5 mm in size was of 0.250 mm while the minimum size of 1.32 mm was adopted when simulating particles of 28.9 mm. These values correspond to approximately 1/22nd of the original particle size. Since no changes were made in the properties of the materials tested, the timestep duration for these simulations were the same as listed in Table 5.1.

Although the fineness of the distribution according to the model is primarily based on the value of t_{10}, the values of t_4 and t_2 were able to better illustrate the accuracy of the software in predicting the size distribution of the progeny. This is due to limitations regarding the minimum global size selected and the challenges associated in representing the finer fractions of the distribution in DEM. Figure 5.3 and Figure 5.4 compare the simulations outcomes with expect values of t_4 and t_2 parameters for copper ore particles of different sizes, respectively.

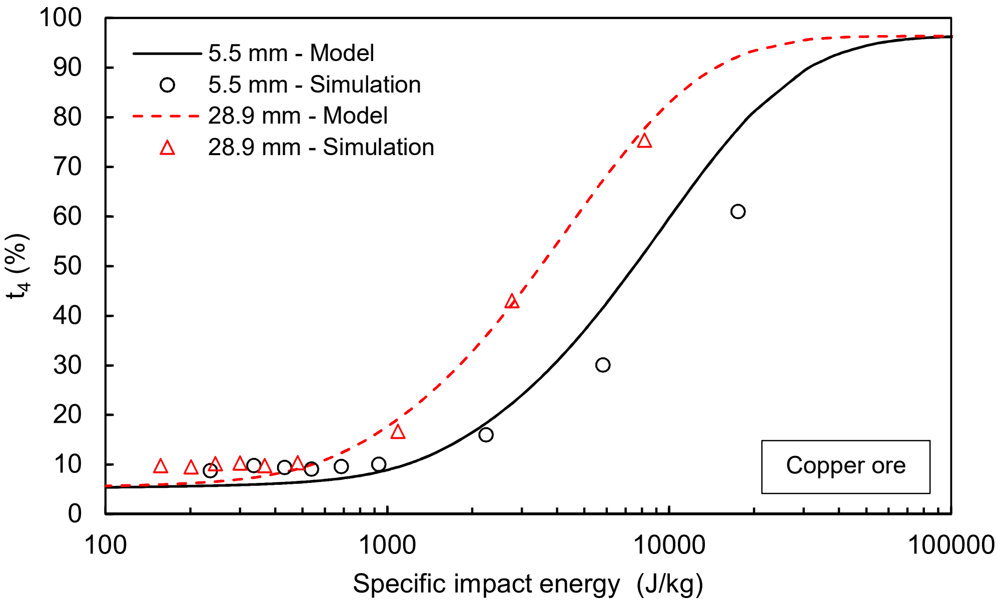

Figure 5.3 - Comparison between the modeled (lines) and simulated (symbols) t_4 values for drop weight tests of 5.5 mm particles (solid lines and hollow symbols) and 28.9 mm particles (dashed lines and filled symbols) of copper ore

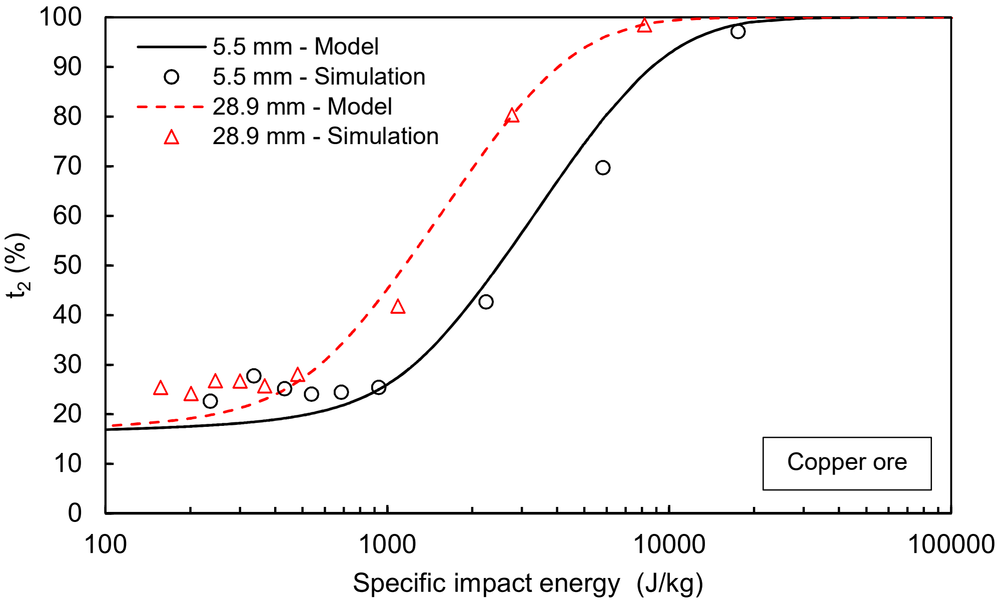

Figure 5.4 - Comparison between the modeled (lines) and simulated (symbols) t_2 values for drop weight tests of 5.5 mm particles (solid lines and hollow symbols) and 28.9 mm particles (dashed lines and filled symbols) of copper ore

The simulations involving copper ore particles of different sizes presented very good agreement with the analytical model. A minor overestimation of the simulated values appeared at low specific impact energies and a small underestimation for the 5.5

mm copper ore particle was detected, but still presenting the appropriate behavior when compared to the expected fineness curves. It is important to highlight that the progeny size distributions that result from the simulations account for the effect of specific impact energy through repetitive primary breakage events following the primary distribution given in Figure 4.1, rather than by representing the relationship between the fineness in the product as a function of stressing energy.

The comparison between simulations and the analytical model presented in Figure 5.3 and Figure 5.4 can also be interpreted as a normalized function based on the median specific energy E_{50}. The ratio between the impact energy and E_{50} can be referred to as the relative impact energy. Figure 5.5 shows the fit between the analytical model and the simulations for the values of t_4 and t_2 and the relative impact energy for the particles sizes of copper ore tested.

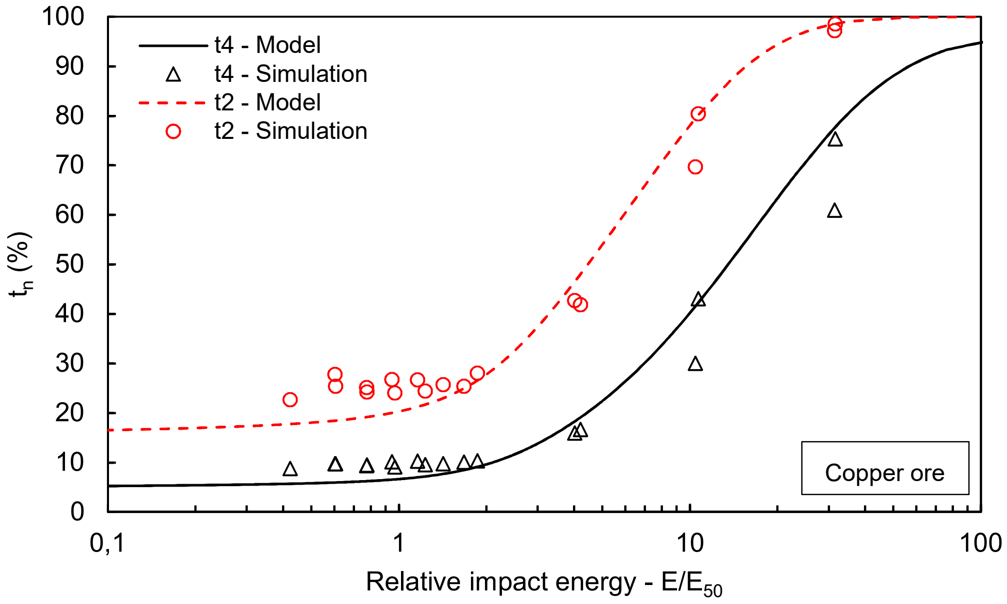

Figure 5.5 – Comparison between the relative impact energy and the fragmentation data for drop weight tests of 5.5 mm particles and 28.9 mm particles of copper ore

The fragmentation of granulite and limestone particles was also assessed based on the corresponding values of t_4 and t_2 (Figure 5.6 and Figure 5.7) for different energies. The comparison between the behaviors of the three materials tested when subjected to breakage is a good example of how the parameters of the incomplete beta function are important in determining the size distribution of the product. Yet, for these materials, a minor overestimation of the simulated results appeared in all situations, indicating that when simulating weaker materials, such as the granulite and the two types of limestone (Figure 5.1) the model overestimate the amount of re-breakage, generating a finer size distribution of the progeny.

In particular, the results involving particles of limestone #2 presented the higher deviation from the analytical model. This may be explained partially by the inability of the Laguerre-Voronoi tessellation to generate a size distribution compatible with such a distinct primary breakage function, as seen in Figure 4.1, presenting a coarser size distribution than the rest of the materials at around half the original particle size but a finer tail, comparable with the other materials tested. Better results were achieved for the materials that presented a well distributed primary breakage size distribution, indicating an inability of the tessellation technique adopted in generate same size fragments after breakage, which can partially explain the overestimation of the fineness at low specific impact energies

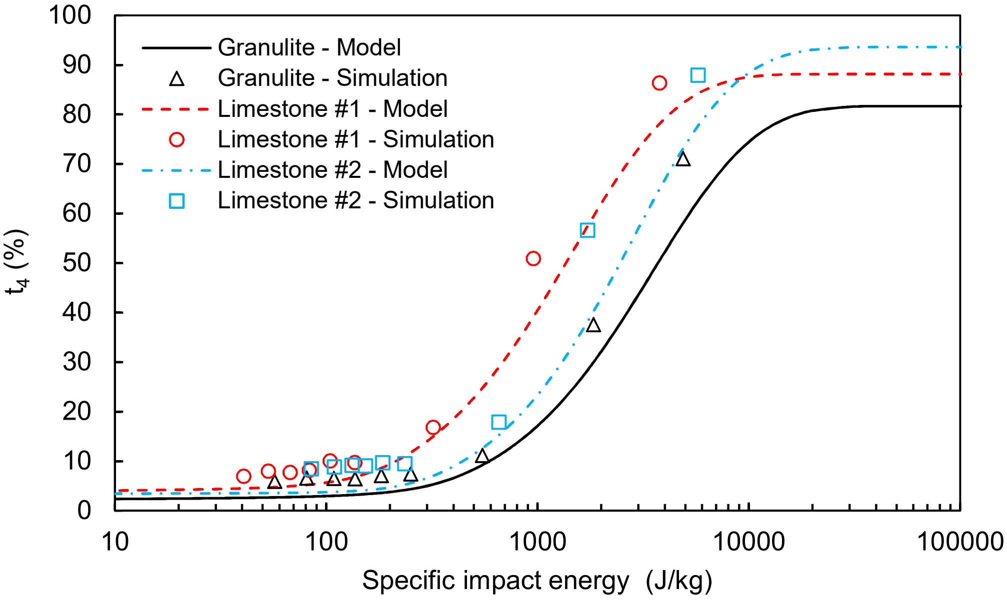

Figure 5.6 - Comparison between the modeled (lines) and simulated (symbols) t_4 values for drop weight tests of 5.5 mm particles of granulite, limestone #1 and limestone #2

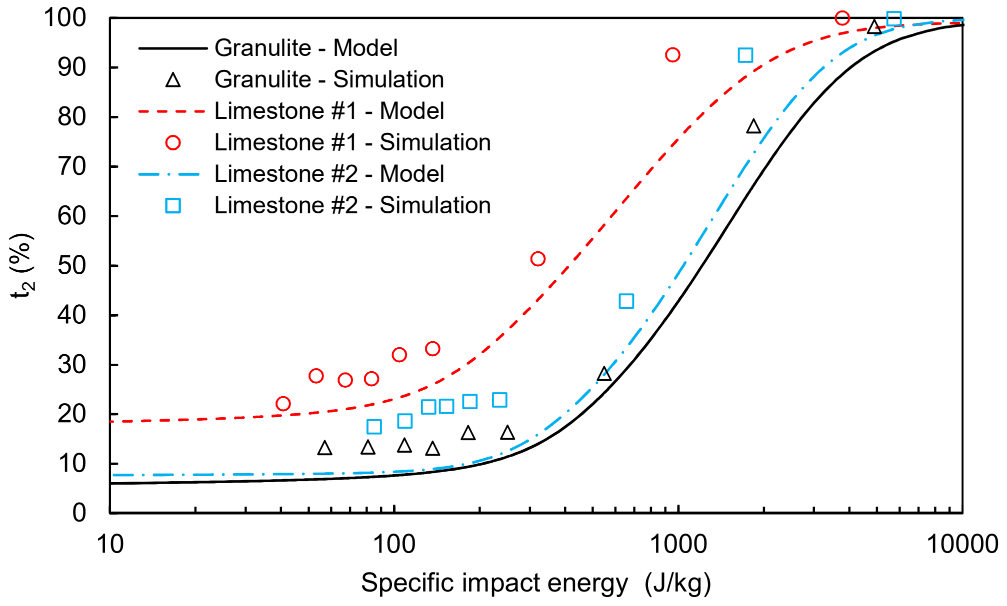

Figure 5.7 - Comparison between the modeled (lines) and simulated (symbols) t_2 values for drop weight tests of 5.5 mm particles of granulite, limestone #1 and limestone #2

Figure 5.8 presents the progeny size distributions of limestone #2 particles for a low, intermediate and high impact energy. The model overestimate breakage for low impact energies, which corresponds majorly to the primary breakage of the particle, leading to an overestimation of the fineness of the fragments for higher energies. On the other hand, Figure 5.9 presents the good agreement between the analytical model and the simulations for the progeny size distributions of copper ore particles of 28.9 mm. As previously explained, due to the minimum size selected, the model underestimates values below around 1/10th of the initial particle size (t_{10}) for all impact energies.

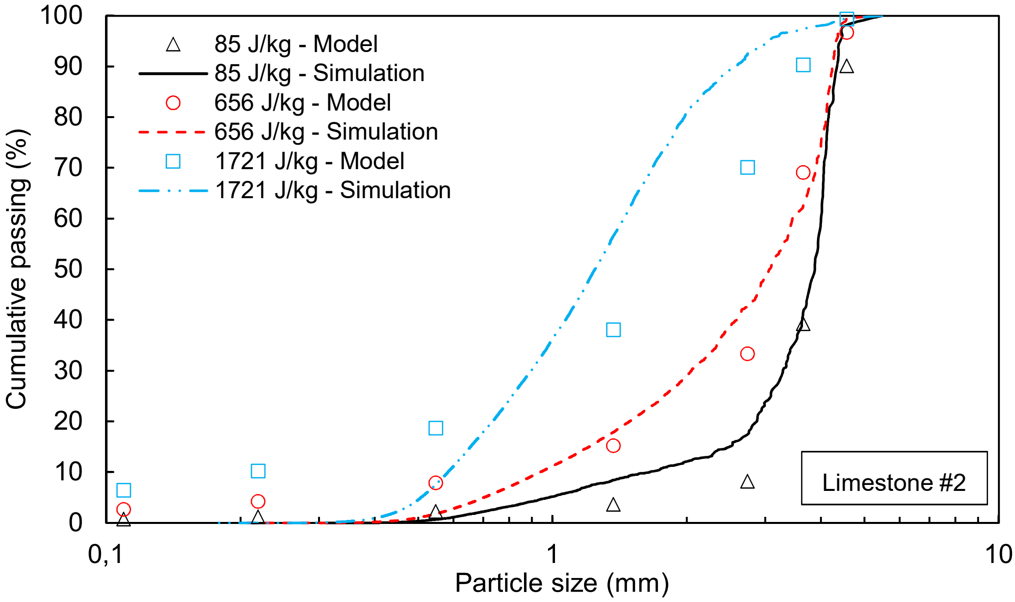

Figure 5.8 - Comparison between modeled (symbols) and simulated (lines) progeny size distributions for drop weight tests of 5.5 mm limestone #2 particles for different impact energies

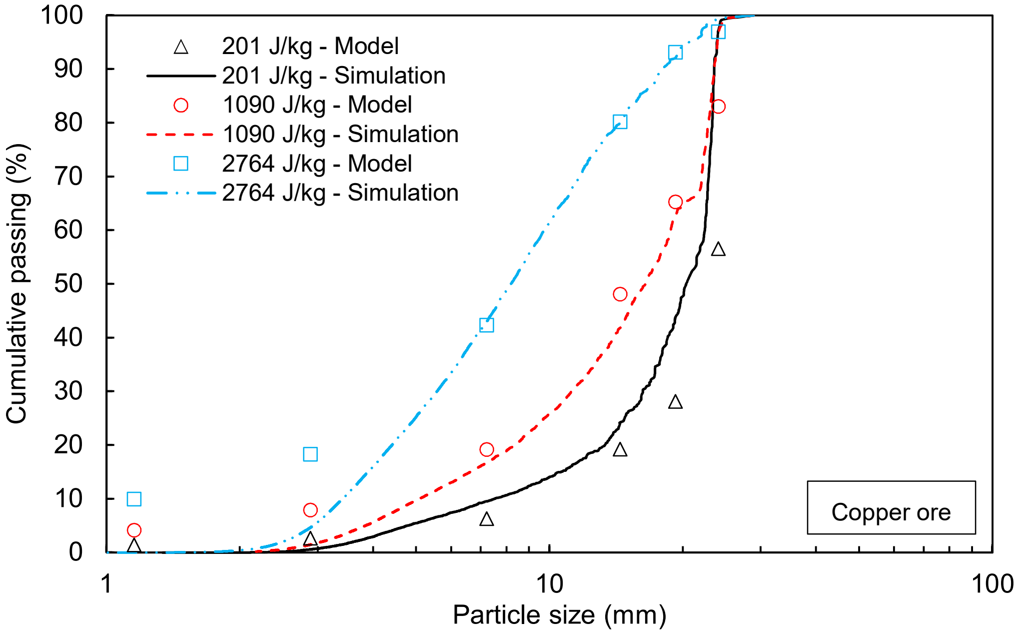

Figure 5.9 - Comparison between modeled (symbols) and simulated (lines) progeny size distributions for drop weight tests of 28.9 mm copper ore particles for different impact energies

5.1.3. Simulation of damage accumulation

The response of the model to damage accumulation due to repeated impacts was assessed in simulations of repeated drops of 100 particles of 37.5 mm in size. The minimum global size adopted in these simulations was 5.0 mm, corresponding to approximately 1/7th of the original particle size. Simulations were performed for both copper ore and limestone #1 particles and the given timestep durations were 5.68e-06 s and 5.47e-06 s, respectively. As already observed in Figure 5.1 and Figure 5.2, it is evident that simulations slightly underestimates the breakage probability for single impact tests. For that reason, numerical analyses were conducted with the expected impact energy, but also with a reduced impact energy, so as to match exactly the breakage probability in the first impact. Table 5.2 presents the values for the specific impact energy and the breakage probability for both the numerical analyses and the simulations. Results for both materials are presented in Figure 5.10, which shows good agreement between the simulated results and the adjusted solution of the analytical model.

Table 5.2 - Predicted and adjusted values of specific impact energy and breakage probability for copper ore and limestone #1 particles subjected to repeated impacts of the same magnitude

	Copper ore		Limestone #1	
	Modeled	Adjusted	Modeled	Adjusted
Specific impact energy (J/kg)	94.7	85.6	10.5	9.4
Breakage probability (%)	10.0	7.3	20.0	15.5

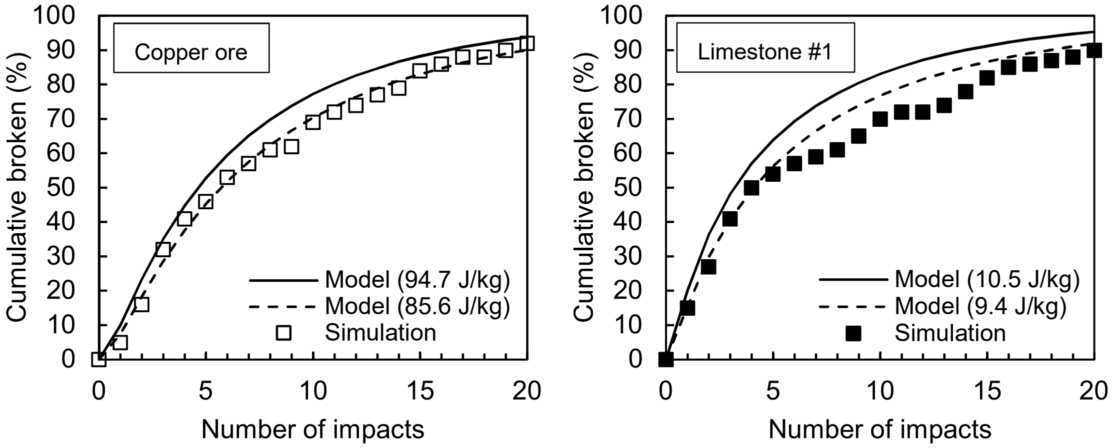

Figure 5.10 - Comparison between the modeled (lines) and simulated (symbols) values of cumulative broken for consecutives single impacts. The solid lines are the expected values for cumulative broken and the dashed line the values of cumulative broken for the adjusted impact energy to match the breakage probability

The sensitivity of both model and simulations to the value of the damage accumulation constant γ was also studied. Small values of γ corresponds to materials in which damage is significant at low deformations while large values of γ correspond to materials that do not accumulate damage until the imposed deformation approaches the deformation required to fracture a particle. γ values of 2.5 and 10 were tested for limestone #1 particles under the adjusted stress conditions listed on Table 5.2. The results are presented in Figure 5.11, which shows that both the analytical model and the simulation respond properly to this variable.

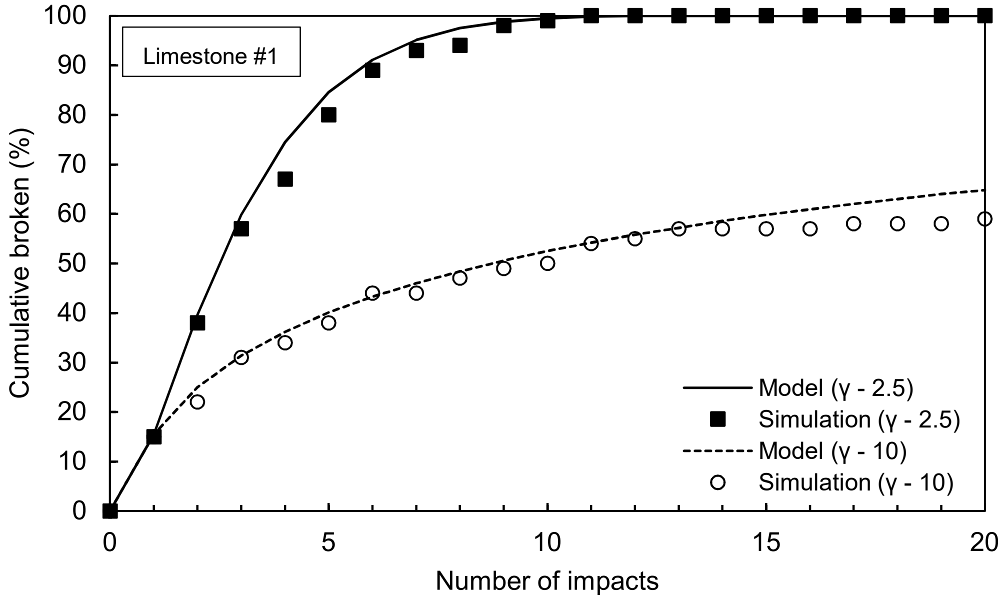

Figure 5.11 - Comparison between the modeled (lines) and simulated (symbols) values of cumulative broken of limestone #1 particles for consecutives single impacts of 10.5 J/kg and different values of γ.

5.1.4. Effects of minimum size variation

The selected minimum particle size of the simulation will directly impact the computational power needed to perform the simulations. Dealing with fine particles in DEM is still challenging due to the large number of particles associated with it. However, the minimum size can also affect the breakage probability and the progeny size distribution, especially due to the use of the Laguerre-Voronoi tessellation to promote particle fragmentation. When a contact reaches the threshold energy of a particle, fragmentation will occur only if the Voronoi algorithm is able to produce a proper particle size distribution respecting the minimum size assigned. This can lead to an underestimation of breakage probability of particles whose size are close from the minimum size as well as influencing the particle size distribution of the fragments.

Breakage tests using the drop weight test and the single impact test apparatus were used to measure the impact of the minimum size assigned for a simulation in the breakage probability and the particle size distribution of the progeny. The simulations were performed for copper particles of 28.9 mm in size and minimum global sizes of 5.78 mm and 1.32 mm. Results of breakage probability presented in section 5.1.1 for minimum particle size of 2.89 mm were also compared in this section. Figure 5.12 presents the results of breakage probability for drop weight tests of simulations adopting different minimum particle sizes. No influence was detected on single impact tests. As it is possible to see, particle sizes that are closer to the minimum particle size assigned for the simulation tend to present a higher deviation from the analytical model, underestimating the amount of breakage. Instead, a finer minimum size will result in better accuracy of the simulations. In both scenarios the breakage probabilities are within a reasonable range from the expected values.

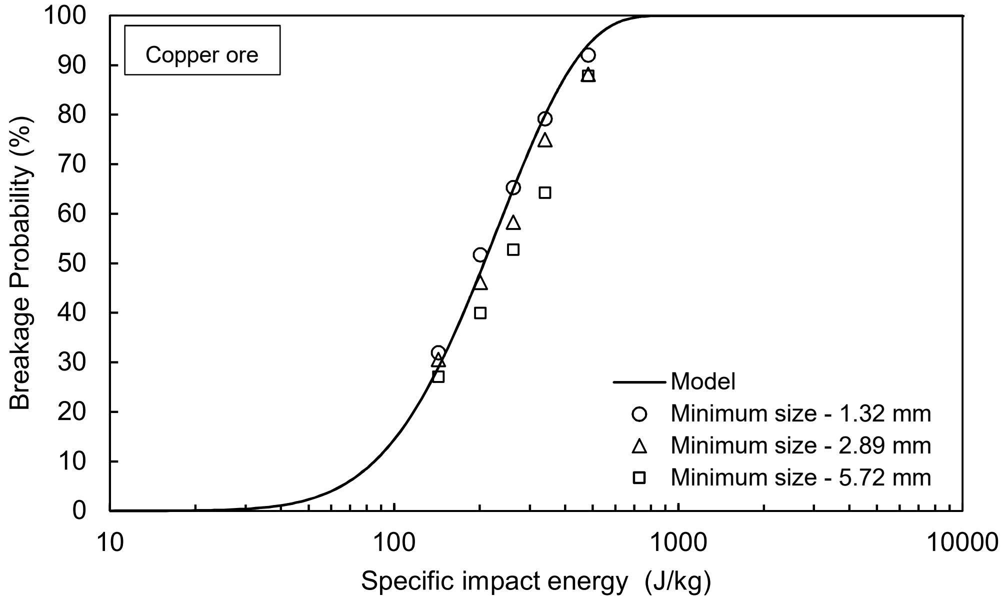

Figure 5.12 - Comparison between the modeled (line) and simulated (symbols) breakage probabilities for drop weight tests of 28.9 mm particles of copper ore for different minimum particle sizes

The impact of the minimum global size on the particle size distribution was also evaluated for the minimum sizes of 0.72 mm, 2.89 mm and 5.72 mm, comparing the results to the ones achieved in section 5.1.2 using the drop weight test apparatus for minimum size of 1.32 mm. For all these tests, the ratio that determines the minimum breakage size was set as to match the minimum global size. Figure 5.13 shows the results for particle fragmentation from an impact at low impact energy, while Figure 5.14 compares the outcomes for contacts involving higher energies. When assessing progeny size distribution, the model starts to lose accuracy when breakage involves particles whose sizes are near the minimum global specified size, especially for high energies. The use of a finer minimum breakage size will also result in a finer progeny size distribution that does not match the expected the predictions from the analytical model. The use of a minimum breakage size of approximately 1/20th of the original particle size resulted in better agreement between the simulations and the model. Therefore, even though the minimum global size can be set to a larger fraction of the original particle size, care must be taken when selecting the minimum breakage size.

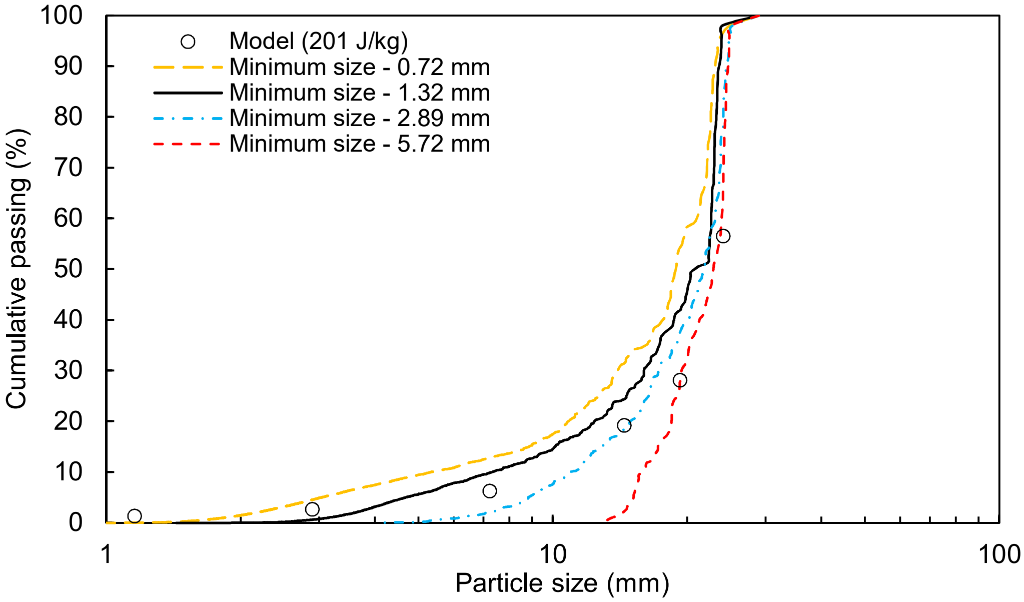

Figure 5.13 - Comparison between modeled (symbols) and simulated (lines) progeny size distributions for drop weight tests of 28.9 mm copper ore particles for different minimum particle size adopting an impact energy of 201 J/kg

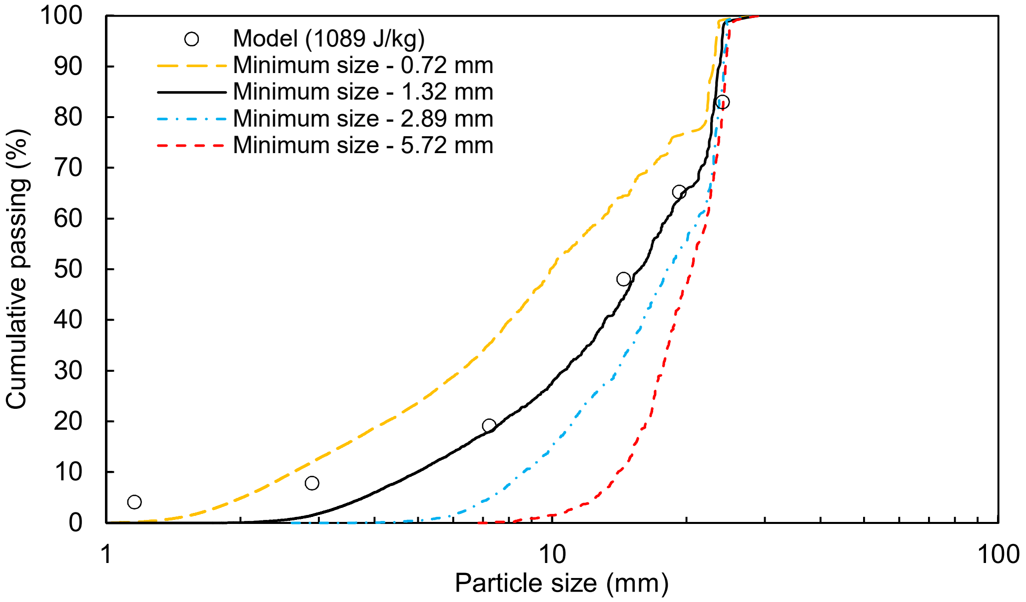

Figure 5.14 - Comparison between modeled (symbols) and simulated (lines) progeny size distributions for drop weight tests of 28.9 mm copper ore particles for different minimum particle size adopting an impact energy of 1089 J/kg

5.1.5. Effects of Young's modulus variation

Different bulk Young's moduli were assessed based on the expected breakage probability for 5.5 mm particles of copper ore and limestone #1. As discussed in section 4.3.5, the Young's modulus of steel, used in both the target and the anvils, must be at least 10 times greater than the Young's modulus of the ore to ensure proper energy split between the parts involved in a collision. Simulations adopting the Young's modulus of the ores as 1e+08 N/m² and 5e+08 N/m² and the Young's modulus of steel 10 times greater than the value adopted for ore particles were performed. Table 5.3 presents the duration of the timesteps for the simulations performed. As expected, increasing the Young's modulus of the ore will reduce the duration of the timestep, demanding more time to process the same simulation. Figure 5.15 presents the results for the breakage probabilities of ore particles adopting the Young's modulus of 1e+08 N/m² while Figure 5.16 shows the results when adopting 5e+08 N/m².

Table 5.3 - Timestep duration for each simulation performed varying the Young's modulus of the materials

Material	Young's modulus (N/m²)	Timestep duration (s)	
		Single Impact	DWT
Copper ore	1.00E-08	1.85E-06	1.85E-06
	5.00E-08	8.29E-07	8.29E-07
Limestone	1.00E-08	1.78E-06	1.78E-06
	5.00E-08	7.98E-07	7.98E-07

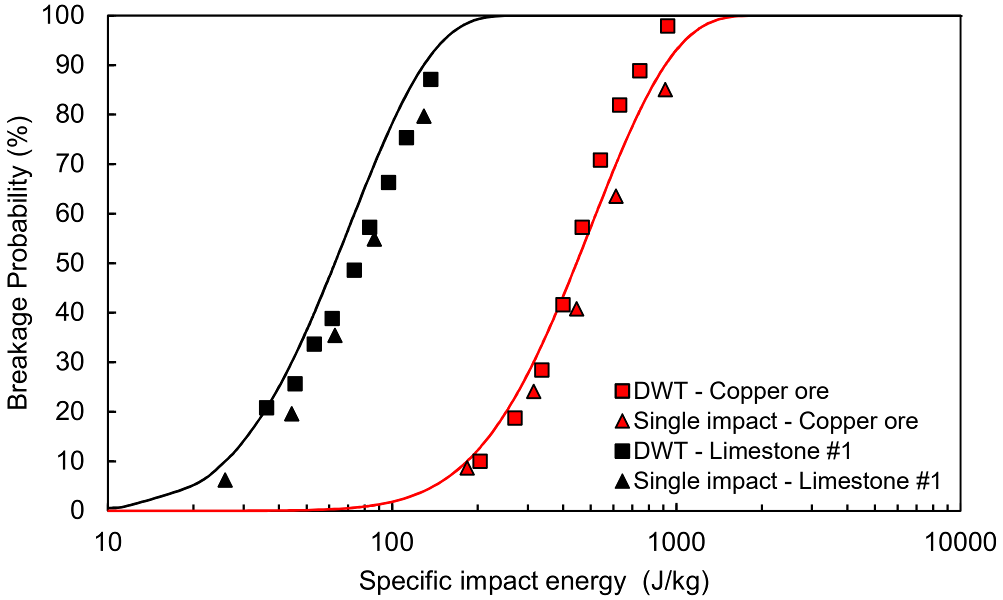

Figure 5.15 - Comparison between the modeled (lines) and simulated (symbols) breakage probabilities for drop weight tests and single impact tests of 5.5 mm particles of copper ore and limestone #1 adopting a Young's modulus of 1e+08 N/m² for ore particles and 1e+09 N/m² for the steel

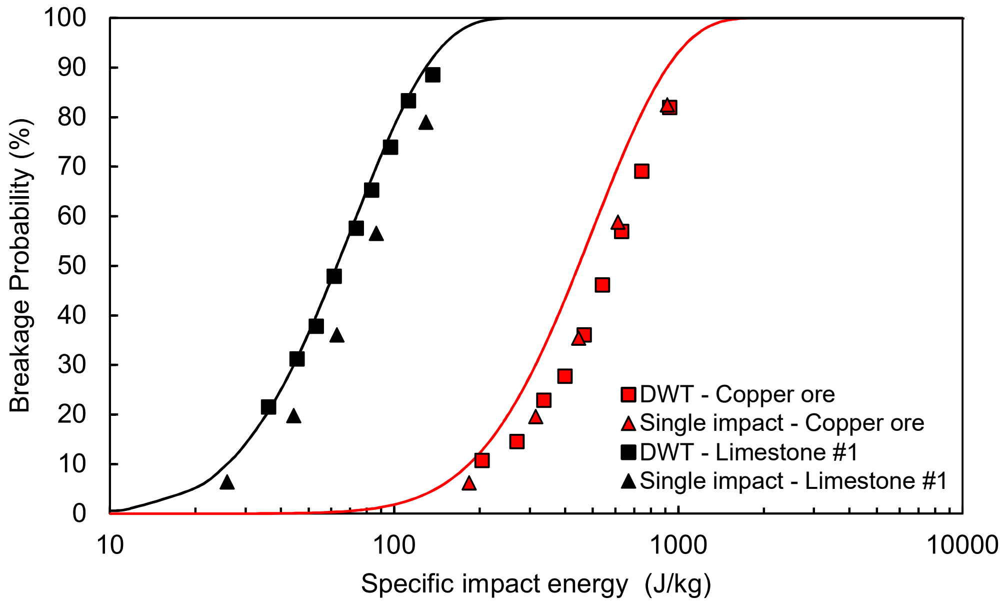

Figure 5.16 - Comparison between the modeled (lines) and simulated (symbols) breakage probabilities for drop weight tests and single impact tests of 5.5 mm particles of copper ore and limestone #1 adopting a Young's modulus of 5e+08 N/m² for ore particles and 5e+09 N/m² for the steel

Comparing the results of Figure 5.1 with the results of Figure 5.15 and Figure 5.16, it is noticeable that the adoption of a Young's Modulus of 5e+08 N/m² for ore particles resulted in a better match to the breakage probability of the analytical model on double impact simulations, however this change did not affect substantially single impact stresses. The adoption of greater Young's moduli for ore particles results in shorter timestep durations, reducing the appearance of small fragments outside the boundaries due to overlap between the particle and the boundary elements, however, demanded at a cost of a greater processing time. The adoption of a Young's modulus of 1e+11 N/m² for the boundaries materials was beneficial for single impact tests, reducing the energy dissipation due to rearranging of particles when in contact with the surface. Still, this change did not affect the timestep duration for single impact condition. For double impact collisions, since the weight is added as a particle in the simulations, the timestep duration became shorter for some materials, as demonstrated in Table 5.1, increasing the processing time. No significant benefits in the breakage probability were detected from this change.

5.1.6. Effect of restitution coefficient variation

The sensitivity of the simulated probability of breakage in respect to the coefficient of restitution has been analyzed for copper ore particles of 5.5 mm in size. Values of 0.1 and 0.6 for the coefficient of restitution were tested in single impact tests and compared to results for the same material adopting the coefficient of restitution of 0.3, as presented in Figure 5.2. The reduction of the coefficient resulted in the need to adopt shorter timesteps, from 8.29e-07 s to 3.12e-07 s. However, the timestep duration did not change after increasing the coefficient of restitution. As expected, smaller coefficient of restitution increased the dissipated energy of the impact, resulting in higher breakage probabilities, as shown in Figure 5.17. Adopting the value of coefficient of restitution of 0.6 did not affect the breakage probability in comparison to the coefficient of 0.3. Still, the results are within a good range from the analytical model and can also be used to calibrate the breakage probability according to the model.

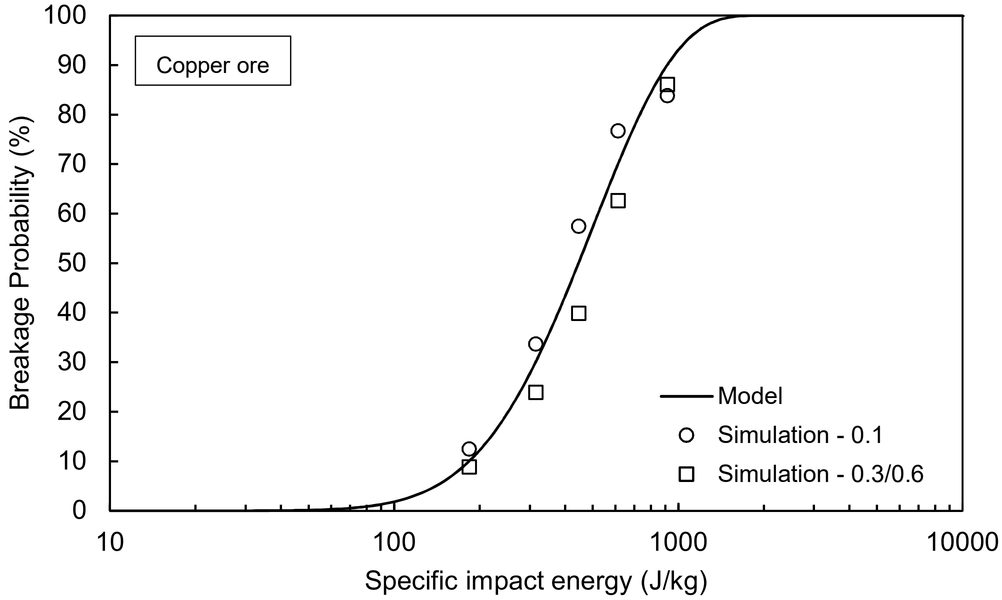

Figure 5.17 - Comparison between the modeled (line) and simulated (symbols) breakage probabilities for single impact tests of 5.5 mm particles of copper ore for different restitution coefficients

5.2. Validation stage

5.2.1. Unconfined particle bed breakage tests

Simulations of breakage of particles contained in different arrangements were compared to experimental results in order to illustrate the ability of the Tavares breakage model to describe not only breakage of individual particles but also progressively more complex systems, involving the interactions of particles as well as of particles and the boundaries of the equipment. The experimental data for validating the model in impacts of unconfined particle beds were collected from the work of BARRIOS (2010), partially reported by BARRIOS *et al.* (2011) and JIMÉNEZ-HERRERA *et al.* (2018).

Copper ore and granulite particles of 6.1 mm and limestone #1 particles of 6.3 mm in size were initially tested in different beds configuration, as illustrated in Figure 4.7, for impacts of 3.05 J, corresponding to a drop height of approximately 0.11 m. Additional testing involved impacting copper ore particles arranged in a monolayer configuration at impact energies of 1.52 J, 6.10 J and 9.15 J. The size of particles for each material was chosen based on the average particle mass observed in experiments. The minimum global size assigned for simulations, as well as the minimum breakage size introduced as a ratio of the parent particle, was 0.250 mm for all the materials, which corresponds to approximately 1/25th of the original particle size. The timestep durations for the three materials tested are presented in Table 5.4 for all the materials tested. As mentioned in section 4.3.5, the Young's modulus adopted for the steel in simulations of unconfined particle bed tests was 5e+09 N/m².

Table 5.4 - Timestep duration for simulations of unconfined particle bed breakage

Material	Particle Size (mm)	Timestep duration (s)
Copper ore	6.1	9.25e-07
Granulite	6.1	9.04e-07
Limestone #1	6.3	9.22e-07

The assessment of the ability of the model to describe breakage of particles resting on a particle bed is possible through the comparison of different materials stressed at constant impact energy. Figure 5.18 compares the broken mass of the bed (mass passing the 4.75 mm size) for the three materials studied for both simulations and experiments. It is quite noticeable that results are in nearly perfect agreement until a ring of particles (7 particles). Beyond this point, differences between experiments and simulations appear, in particular for the granulite and limestone #1 particles. Nevertheless, the general effect of material and number of particles making up the bed becomes evident.

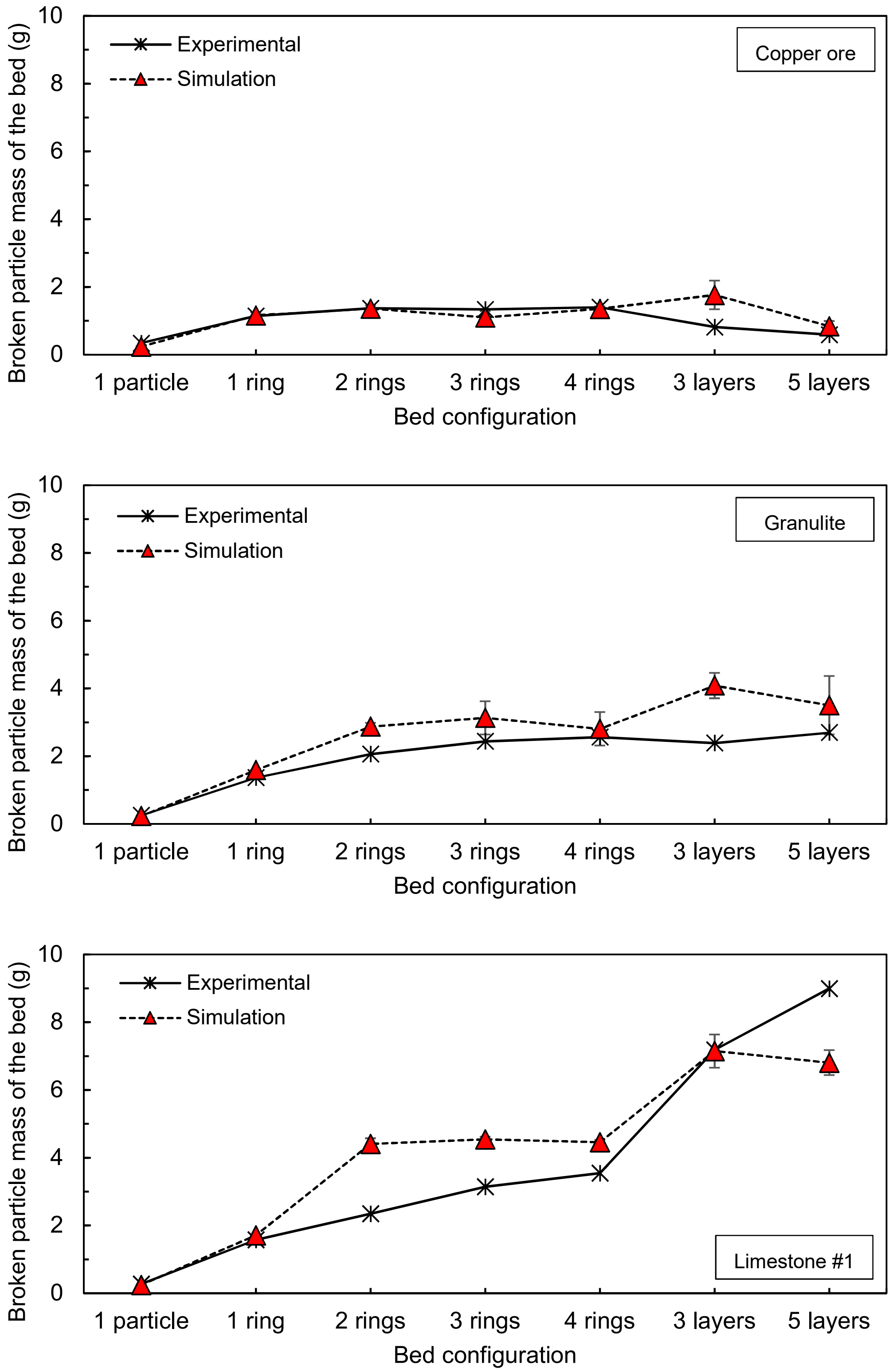

Figure 5.18 - Comparison of the broken mass of particles (passing a 4.75 mm sieve) in experiments and simulations of impact with an 88 mm diameter ball in beds under different arrangements for the materials studied at 3.05 J

It is clear from the experiments and simulations that increasing the number of layers of particles for the copper ore, which is the toughest material among those studied, resulted in a drop in the proportion of material broken, which can be explained by the loss of momentum of the ball as it pushes most of the material away until the final layer of particles is nipped. In the case of the brittle limestone #1, the proportion of material broken increased while increasing the amount of layers whereas for the granulite, this amount was kept constant throughout the tests.

The differences involving the dynamics of the contact between the ball and particle beds composed of different materials become clearer when comparing the penetration of the ball in the bed. Figure 5.19 shows the cutaway view of the drop ball penetrating both the bed of copper ore and limestone #1 particles for the same timestep. It shows that the steel ball penetrated further in the bed and generated more fragments in the case of limestone, given the little resistance offered by the particles during breakage. In contrast, the tougher copper ore particle was more capable of resisting the downwards motion of the ball since its kinetic energy was mostly used to eject particles contained in the upper layers of the bed, rather than breaking them. The observation from both Figure 5.18 and Figure 5.19 indicates that the brittle nature of the limestone contributes in the increasing of the broken mass of the bed to as much as five layers. This is explained by the very low strength of the particles and to the fact that the stressing energy of the ball as soon as it penetrates the upper layers of the bed are high enough to break the particles. While this effect seemed to reach saturation when the bed is made up of three layers in the case of the simulations, adopting a five-layer bed in experiments presented more benefits.

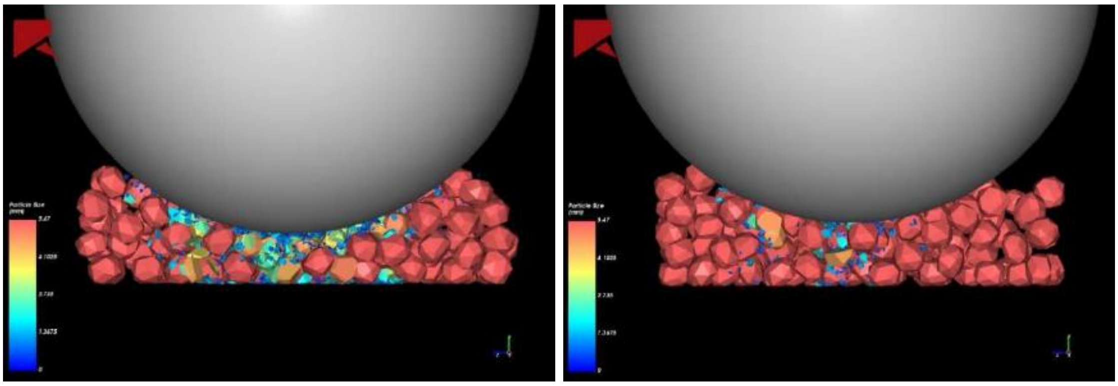

Figure 5.19 - Comparison of cutaway views of the 5-layer beds of limestone #1 (left) and copper ore (right) particles from impacts at 3.05 J with an 88 mm diameter ball at the exact time elapsed from simulation. Particles colored as a function of their size

Figure 5.20 illustrates the position of the bottom of the dropping ball for experiments and simulations. The analysis of the descending motion of the impact ball against the five-layer copper ore bed in experiments using a high-speed camera shows that the ball moves in a free fall condition for nearly 16 mm after penetrating the bed, considering a total height of about 22-26 mm for beds. Similar analysis for the simulations indicates that the ball start to decelerate 6 mm after reaching the top layer, considering a total height of 16-20 mm for beds in simulations. The results also indicates that the impact ball in experiments penetrated further in the bed, reaching its lowest position at approximately one layer and half of particles, while for the simulations the ball reaches its minimum at approximately three layers of particles.

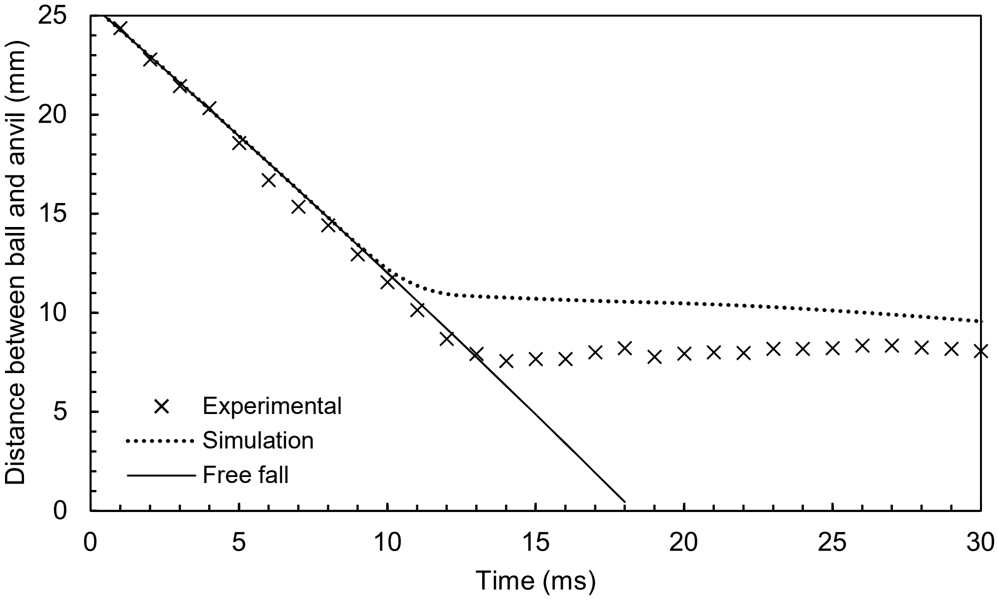

Figure 5.20 - Distance between the bottom of the dropping ball and the anvil during impact test of the 88 mm ball against a five-layer copper ore bed for energies of 3.05 J

An additional analysis of the results is possible by comparing the size analyzes of the tested material after impact. These results, shown in Figure 5.21, Figure 5.22 and Figure 5.23 for copper ore, granulite and limestone #1 particles, respectively, demonstrate that simulations were able to capture in great detail the effect of the bed configuration on the size distribution after the impact, discriminating between the different materials as well. Size distributions of the product for the distinct materials presented equivalent behavior to the results for single particle breakage tests and, while the simulations of copper ore bed presented the best agreement among the materials, granulite and limestone #1 bed overestimated breakage, presented finer size distributions for the products. The results from simulations were truncated at the 0.85 mm size, which is 3.4 times the minimum size of 0.250 mm adopted in the simulations. Beyond this point, no agreement between the simulated and experimental results were achieved due to the limitations imposed by the selected minimum global size.

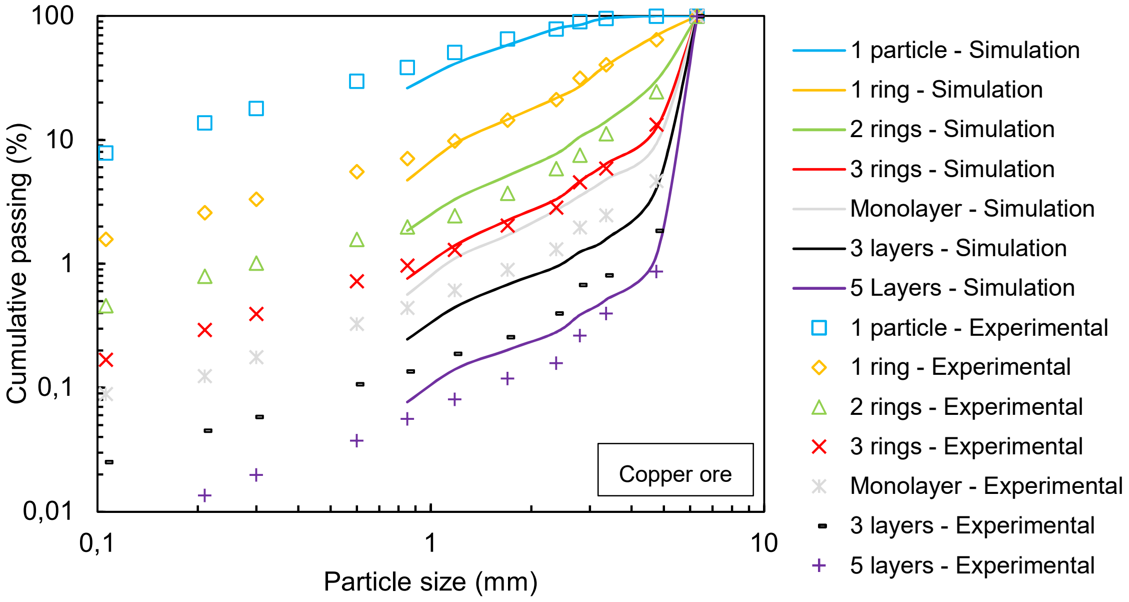

Figure 5.21 - Comparison between size distributions of the bed material after impact at 3.05 J with an 88 mm diameter steel ball for copper ore particles. Symbols represent experimental data and lines simulations

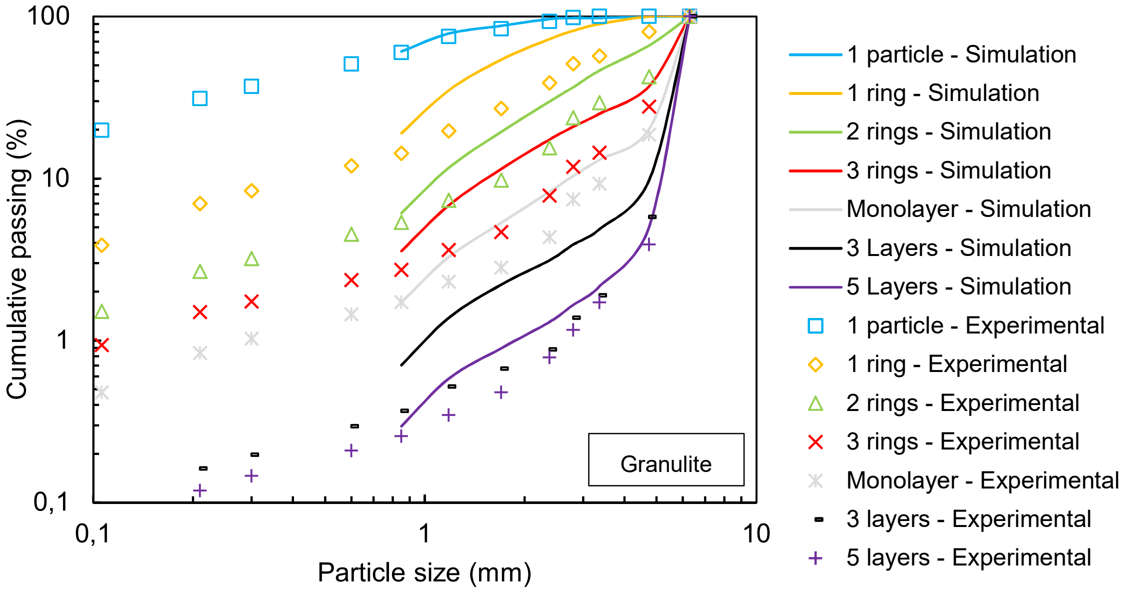

Figure 5.22 - Comparison between size distributions of the bed material after impact at 3.05 J with an 88 mm diameter steel ball for granulite particles. Symbols represent experimental data and lines simulations

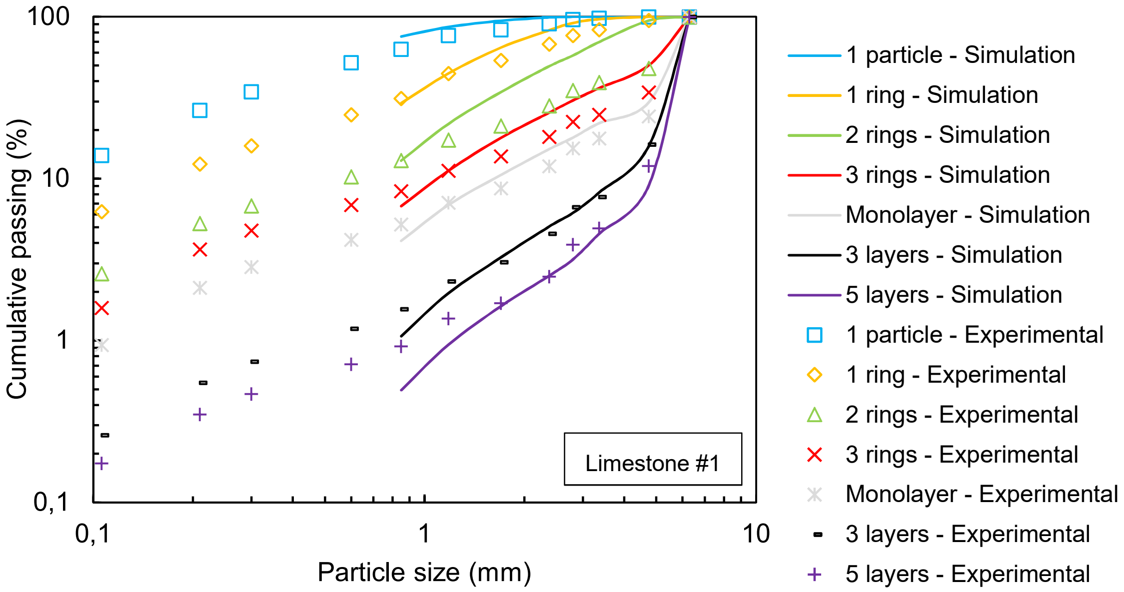

Figure 5.23 - Comparison between size distributions of the bed material after impact at 3.05 J with an 88 mm diameter steel ball for limestone #1 particles. Symbols represent experimental data and lines simulations

A more detailed analysis of the effect of the impact energy in breakage of particle beds was done by comparing the simulated results of monolayer beds at different impact energies with experimental data. Figure 5.24 presents the broken mass of particles, i.e. the proportion of material leaving the original size range of the particles (4.75 to 6.3 mm), for both simulations and experiments. The results show a nearly perfect agreement between them. The size distributions of the tested material after the impact is presented in Figure 5.25, which show fairly good agreement with experiments.

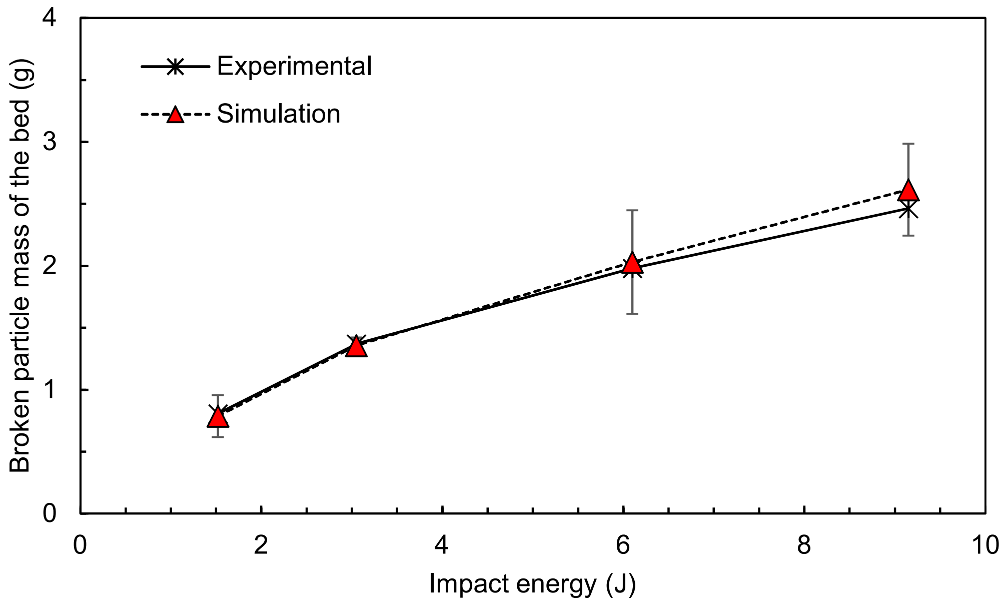

Figure 5.24 - Comparison of the broken mass of particles (passing a 4.75 mm sieve) in experiments and simulations of impact with an 88 mm diameter ball in a monolayer bed of 6.1 mm copper ore particles

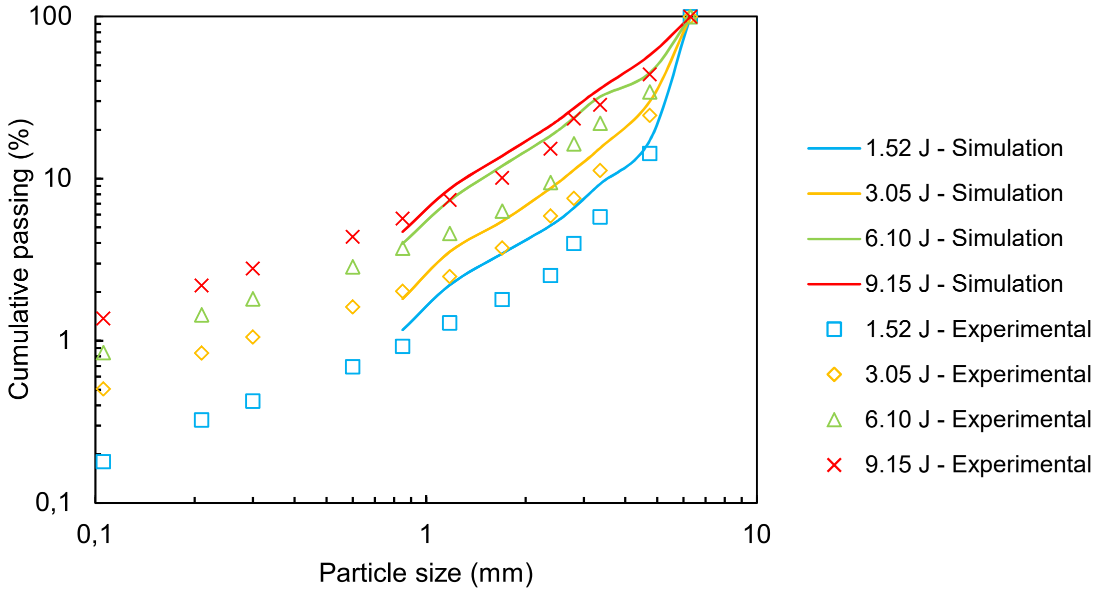

Figure 5.25 - Comparison between the size distributions of the material from impact of an 88 mm diameter ball in a monolayer bed of 6.1 mm copper ore particles at different impact energies

An additional comparison between the simulated results and the experiments is possible by inspecting the radius of capture measured using the experiments and the estimated one from the simulations. The experimental capture radius in the bed of particle was estimated by placing carbon paper and a white paper sheet underneath the bed and then using image analysis to analyze the area and radius of the impressions (BARRIOS *et al.*, 2011). On the other hand, the simulated captured radius was achieved based on the observation of the area nipped by the steel ball. Figure 5.26 illustrates how the estimation of both experimental and simulated capture radius were performed, while Figure 5.27 compares both results for the different impact energies tested. The results show that the simulations properly predicted the increase in the radius with the increase in the impact energy, marginally underestimating the measured values in experiments. Such comparison shows that both simulations and experiments accounted for the fact that, as the impact energy increases, the steel ball has more energy to travel further downwards in the bed of particles, nipping particles on the outer rings.

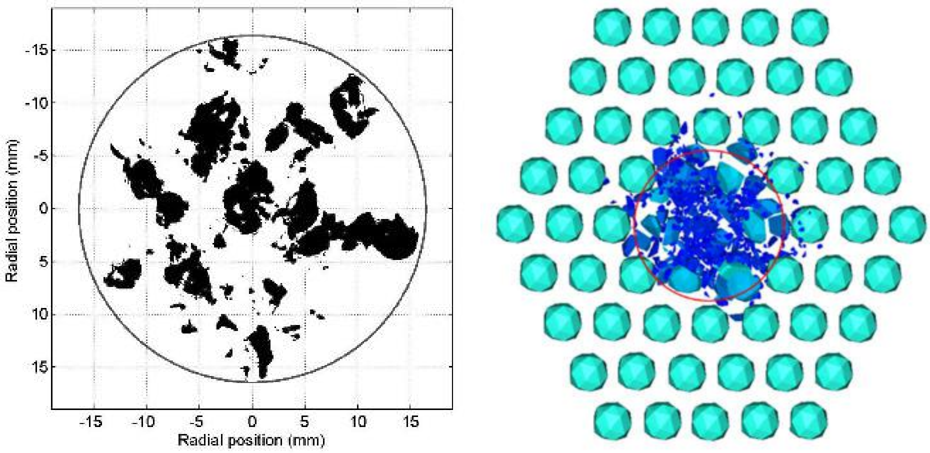

Figure 5.26 - Exemplification of the technique adopted to measure the radii of capture of particles in experiments (left) and simulations (right) for an impact of 3.05 J with an 88 mm diameter steel ball on copper ore particles. The capture radii are represented by the circles in both illustrations

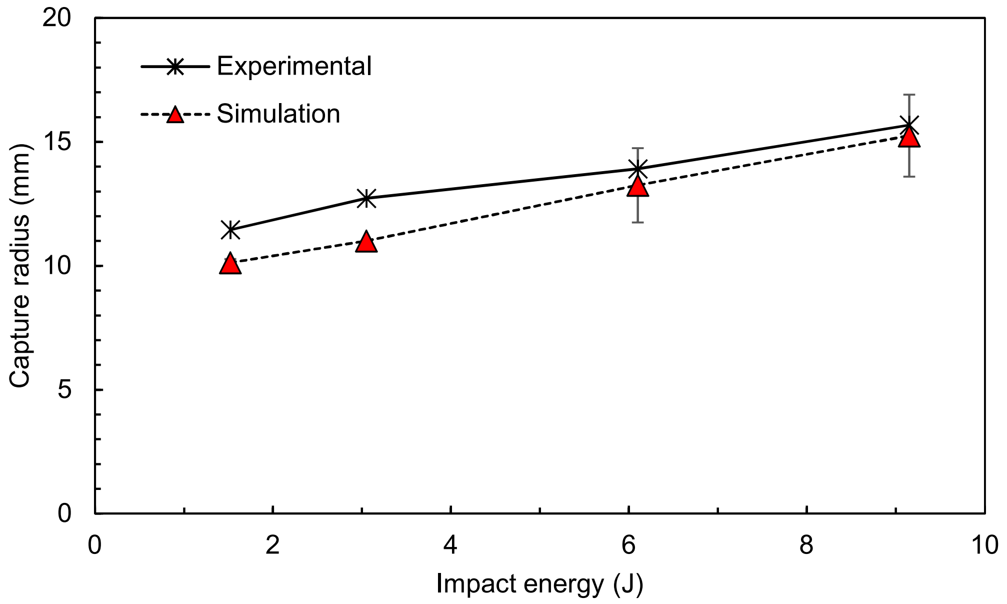

Figure 5.27 - Comparison of the radii of capture of particles in experiments and simulations as a function of impact energy for an 88 mm diameter steel ball dropping on a monolayer bed of 6.1 mm copper ore particles

5.2.2. Laboratory cone crusher

Crushing simulations of different materials in a laboratory-scale cone crusher (Denver No. 12) were performed and the results were compared to experiments. Cone crushers are complex systems in which the understanding of the internal mechanics and flow behavior are not easily assessable. Thus, the use of the Tavares breakage model to describe breakage in a cone crusher is an important step in the process of validating the model in a more complex systems in which not only the breakage must be described properly but also the interaction between particles and boundaries. Experimental data was used for comparison was partially reported by MAGALHÃES & TAVARES (2014).

Simulations involved three distinct materials. Copper ore, granulite and limestone #1 particles sized from 16 mm to 22.4 mm were tested. Different feed flow rates were used according to the material tested in order to achieve choke-feed condition of the crusher. Feed flow rates of 2.0 t/h, 2.5 t/h and 3.0 t/h were used for simulations of copper ore, granulite and limestone #1, respectively. These values of feed flow rates are higher than the expected throughput of the simulations, allowing the filling of the feeder and granting a choke feed condition. As stated in section 4.3.6, four different particle shapes were used in simulations in order to reach an appropriate filling of the crushing chamber. It was observed that using only one particle shape would affect particle flow due to the appearance of void spaces between the particles. Minimum global particle size assigned for the simulations corresponded to 1/10th of the representative size (1.9 mm). Figure 5.28 illustrates the simulation of a crushing experiment adopting granulite particles. It is possible to notice that the simulation presents adequate packing of material inside the crusher chamber and that level of material in the feeder of the crusher indicates that the crusher is operating under choke-fed conditions.

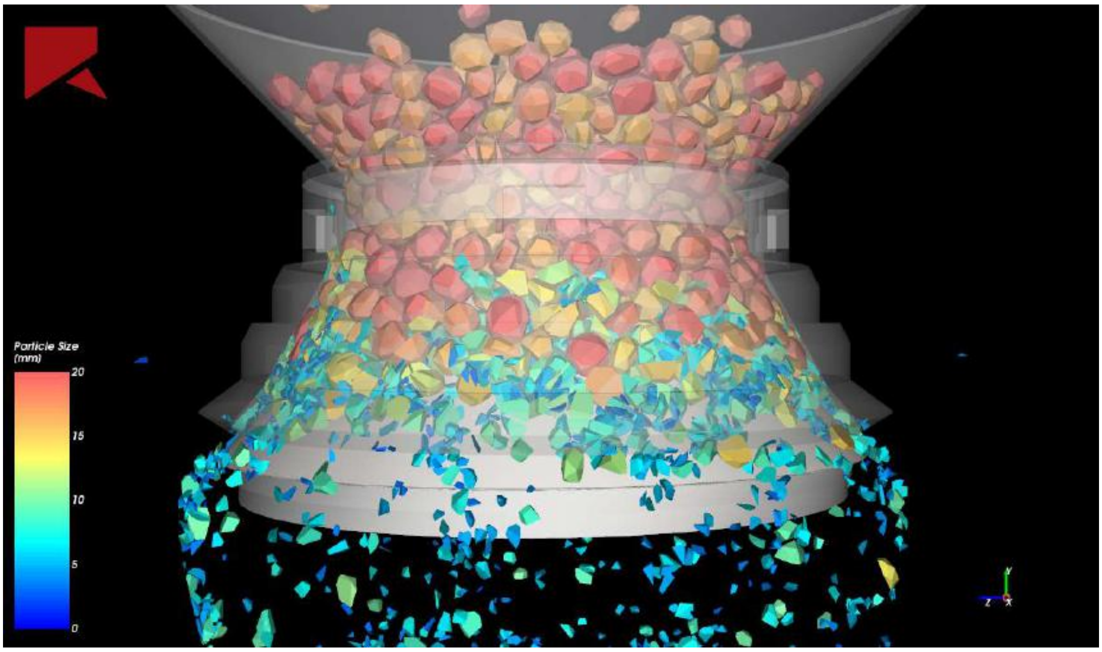

Figure 5.28 - Frame of a simulation of the laboratory cone crusher with a CSS of 5.0 mm being fed with granulite particles sized from 16 mm to 22.4 mm

Simulations using values of Young's modulus of 5e+08 N/m² for ore particles and 5e+09 N/m² for steel were initially carried out but only poor agreement between experimental and simulated results in respect to throughput were found. No obvious reasons were found that could explain such unusual behavior on particles fracture energy. However, due to the small stroke of only 0.5 mm of the laboratory cone crusher, particles are less prone to suffer larger deformations and the effect of the surface of the particles becomes significant. Owing to that, and taking advantage of the fact that a reduction in the Young's modulus was not found to affect significantly breakage probability, as demonstrated in section 5.1.5, values of Young's modulus of 1e+08 N/m² for ore particles and of 1e+09 N/m² for steel were set for the cone crusher simulations. Table 5.5 presents the timestep durations for each simulation adopting the Young's modulus described.

Table 5.5 - Timestep duration for cone crusher simulations

Material	Timestep duration (s)
Copper ore	4.84e-06
Granulite	4.72e-06
Limestone #1	4.65e-06

Figure 5.29 illustrates the throughput of simulations adopting different materials. As simulations involved three distinguishable materials according to their breakage strength, varying from the tough copper ore to the soft limestone #1, it becomes clear that the model was able to capture the effect of the fracture energy of the materials on the throughput. The first two seconds of simulations are only dedicated to fill the feeder of the crusher as the movement of the cone only starts after two seconds of simulation have already elapsed. The three simulations tended to reach a steady-state condition between five to seven seconds of operation and, beyond this moment, the measured throughputs reached an approximately constant rate. Differences between the flow rates of materials that leave the crusher are quite clear, indicating that the model described well the influence of material strength in crusher throughput.

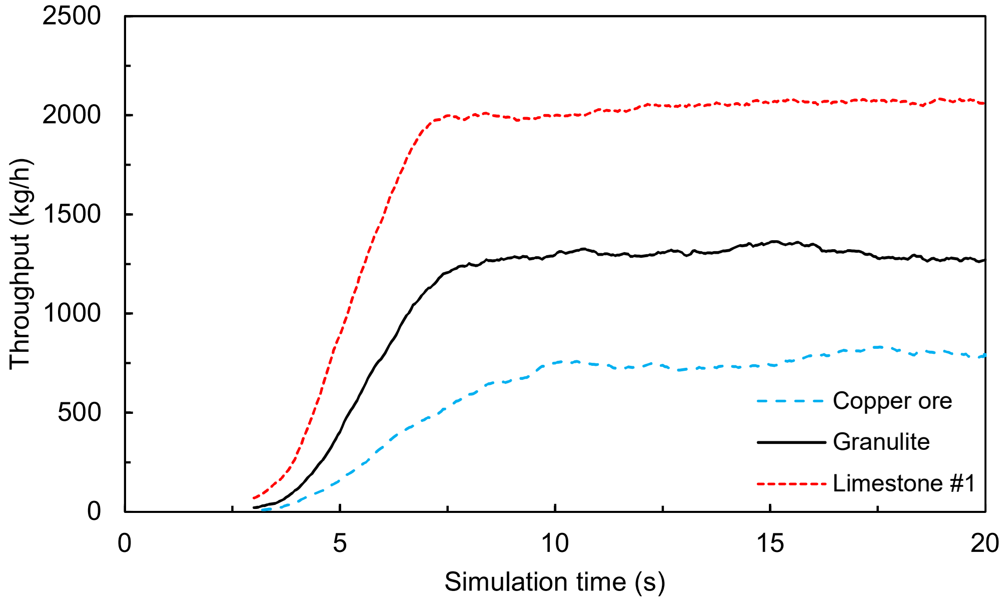

Figure 5.29 - Simulated discharge rate in crushing tests involving copper ore, granulite and limestone #1 particles. Throughput analysis starts at 3 seconds of simulation

The measured power draw in simulations was also investigated. This value corresponds to the power required to move the geometry at a specified speed given the particle mass applied to the surface. While soft materials, such as the limestone #1, tends to break at lower energy, imposing less resistance to the movement of the cone, copper ore particles will break at higher energies, demanding more from the crusher to perform the movement. Figure 5.30 compares the power draw for the three materials tested. It is possible to see that during the first two seconds of operation, simulations returned values of power draw that are higher than the readings from the rest of the simulation. This occurs due to the fact that, in Rocky DEM, the cone is free to rotate around its axis until reaching an equilibrium condition in which the forces acting on its surfaces prevent it from rotating, as observed in reality. Beyond that, the power draw stabilizes at three different levels according to the material being simulated, demanding more power in crushing simulations of copper ore and less power in simulations of limestone #1, as expected.

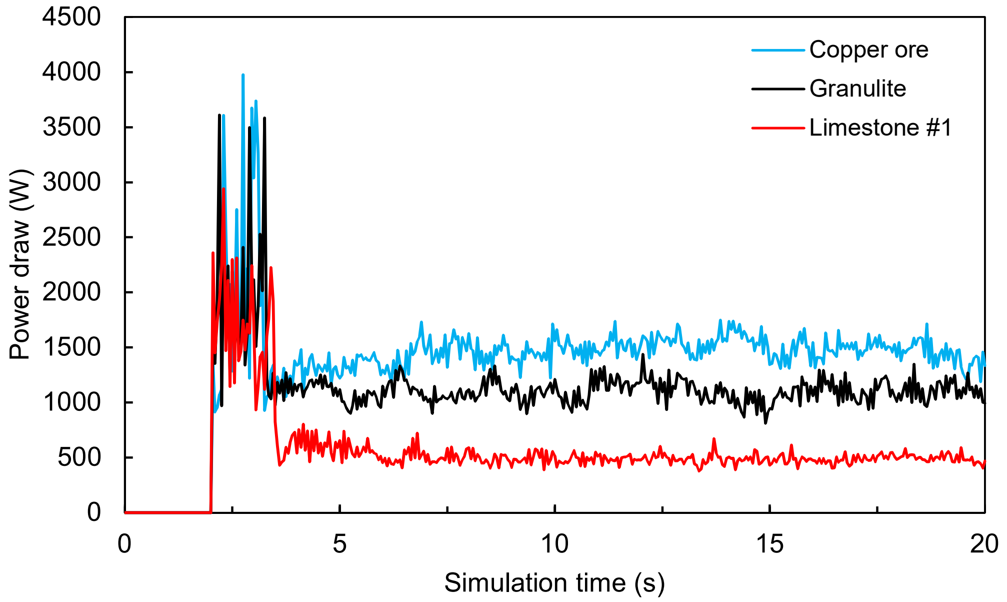

Figure 5.30 - Simulated power draw of crushing tests involving copper ore, granulite and limestone #1 particles

The comparison between simulated and experimental results for the three materials has also been performed and it is presented in Table 5.6. Simulation results presented fairly good agreement to experiments. An average of 20% more throughput was detected in simulations when compared to experimental data. Moreover, comparisons between the simulated power draw and the experimental net power measured using a power meter attached to the cone crusher presented low correlation. Lower values of simulated power draw, in addition to the overestimation of throughput, underestimated the specific energy consumption of the simulations. Still, lower values of power draw in simulations were expected due to the fact that these results do not take into account the existing power dissipation in experimental tests, which can account for almost 50% of the power draw of an equipment of this size.

Table 5.6 - Comparison between simulated and experimental results for throughput, power draw and specific energy of cone crusher tests

	Material	Coper ore	Granulite	Limestone #1
Throughput (t/h)	Simulation	0.77	1.31	2.05
	Experimental	0.69	0.95	1.87
Power draw (kW)	Simulation	1.50	1.10	0.49
	Experimental	2.71	2.29	0.65
Specific energy (kWh/t)	Simulation	1.95	0.84	0.24
	Experimental	3.93	2.41	0.35

A deviation of the simulated product size distribution was also detected. On the coarse size of the curve, the size distribution was mainly affected by the tendency of the Laguerre-Voronoi tessellation scheme in generating flaky fragments on a breakage event, preventing them from rebreakage as they move downwards in the crushing chamber. Figure 5.31 illustrates particles coarser than 9 mm (represented in red), which matches the top size found in experiments, leaving the crusher due to their lamellar appearance. On the finer tail of the curve, low agreement was found due to the minimum size of only 1/10th of the representative size of the feed. As presented in section 5.1.4, this ratio is responsible for providing low accuracy of the fines of the distribution. Figure 5.32 presents the comparison between simulated and experimental particle size distributions for crushing experiments of the three materials, illustrating the deviation found in simulations.

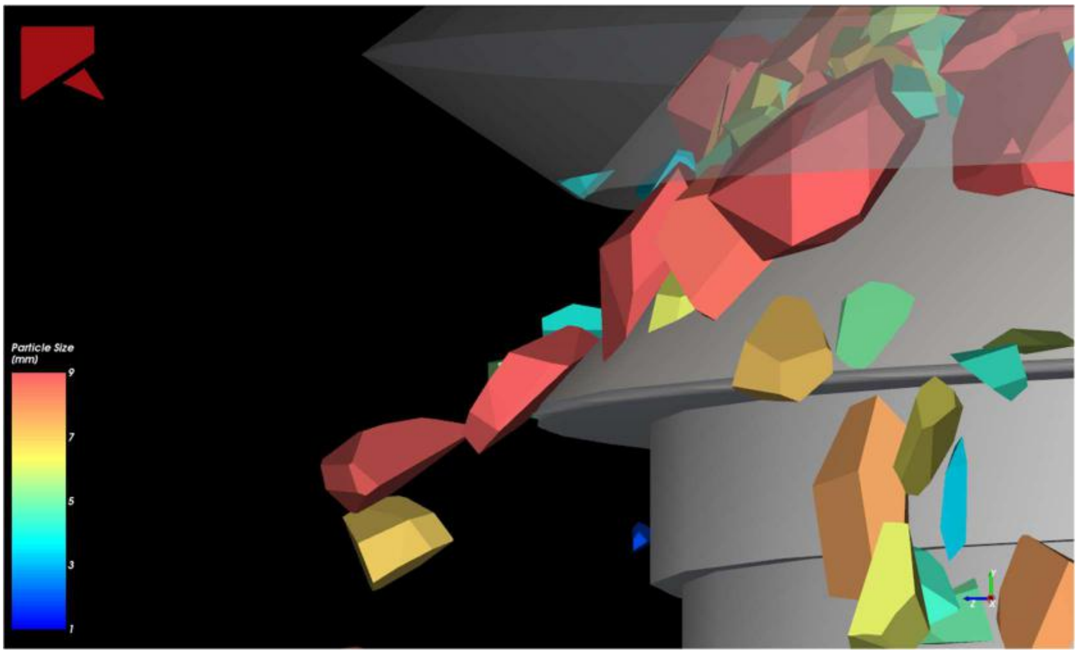

Figure 5.31 - Illustration of material leaving the crusher without undergoing further rebreakage due to the elongated shape of the fragments

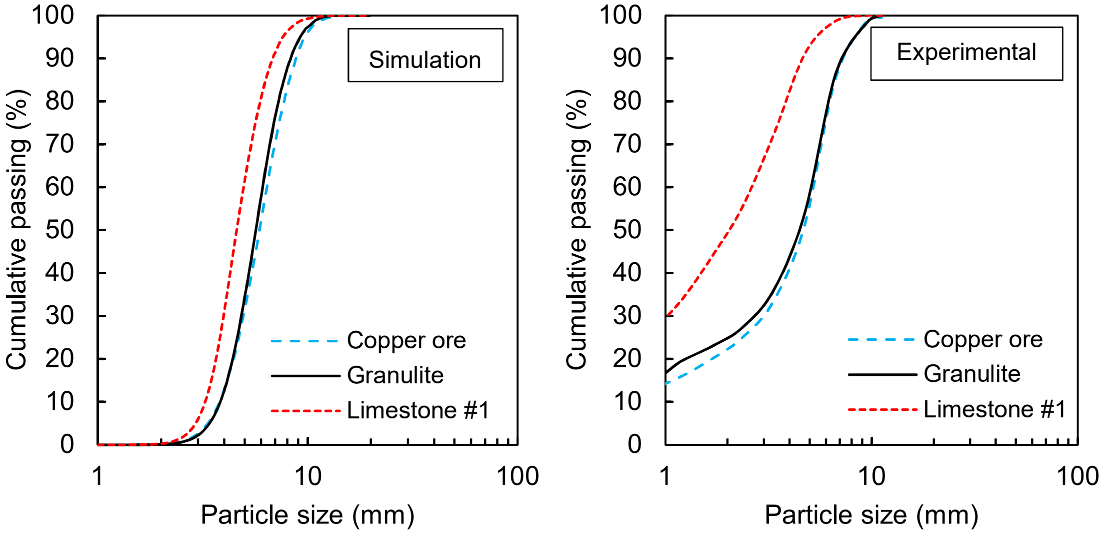

Figure 5.32 - Comparison between simulated (left) and experimental (right) particle sizes distributions of crushing tests involving copper ore, granulite and limestone #1 particles

Still, as it is possible to see, the model correctly predicted the difference between the three materials and, although crushing experiments of granulite presented a throughput around 40% greater in experiments and 70% greater in simulations in comparison to copper ore particles, results of the granulite presented similar particle size distribution for both experiments and simulations, whereas limestone #1 particles suffer greater rebreakage, reporting at finer fractions on the product.

5.3. Application stage

5.3.1. Pilot horizontal shaft impact crusher

A model that is able to describe particle breakage with fidelity in a DEM environment can be used for several purposes. Simulations using a pilot-scale horizontal shaft impact (HSI) crusher were performed with the aim of presenting a use of the model in optimizing a comminution process. In this case, selective breakage of two different materials fed into an impact crusher was investigated. With a proper calibration of the breakage parameters and the operating conditions of the crusher the separation between different types of ores could be carried out simply with a screening process downstream.

For simulations of the pilot HSI crusher, the Young's modulus of 5e+08 N/m² was adopted for ore particles, whereas for steel it was adopted the Young's modulus of 5e+08 N/m². The timestep duration for all the simulations was of 2.33e-06 s, while the minimum global size chosen was 1/10th of the representative particle size of the feed distribution (1.9 mm).

Simulations involved a blended feed of copper ore and limestone #1 particles ranging from 16 mm to 22.4 mm. Minimum global size assigned for the simulations was of 1.5 mm which corresponds to approximately 1/13th of the representative size of the feed. Two rotational velocities were tested. The first one of 1098 rpm, generating a tip speed of 40.1 m/s and the second one of 281 rpm, corresponding to a tip speed of 10.3 m/s. A scenario that presents such distinct materials as the one simulated using the HSI crusher, allows the possibility of selective breaking ore particles based on their fracture energies. Figure 5.33 illustrates the difference between fracture energies of copper ore and limestone #1 particles for the feed size in question, indicating the corresponding impact energy applied to ore particles when using different rotational velocities of the rotor.

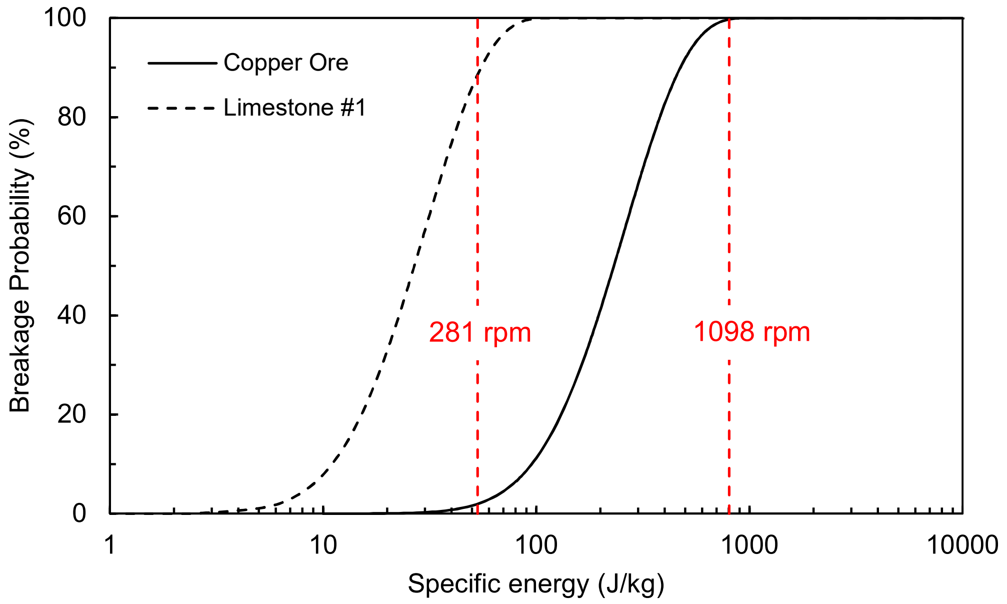

Figure 5.33 - Distribution of breakage probability for copper ore and limestone #1 particles of 16 mm to 22.4 mm in size. Vertical lines indicate the impact energy of a collision between a particle and the blow bar for the different rotational velocities tested

As it is possible to notice in Figure 5.33, the highest rotational velocity will apply impacts of approximately 800 J/kg, which almost match the required energy to break all particles of copper ore being fed into the impact crusher. This energy is significantly higher than the maximum required to break limestone #1 particles in single particle breakage tests. In this case, no selective crushing would occur, as most of the feed material will undergo a breakage event before leaving the crusher. Indeed, very few particles are able to escape the HSI crusher without suffering a size reduction process. Figure 5.34 illustrates the particle size distribution of the feed and the product, as well as the individual analysis of each material that compose the blended product. No selective crushing took place as only 8.5% of the blended feed left the crusher without breaking and further classification based on the size of the particles would not be possible.

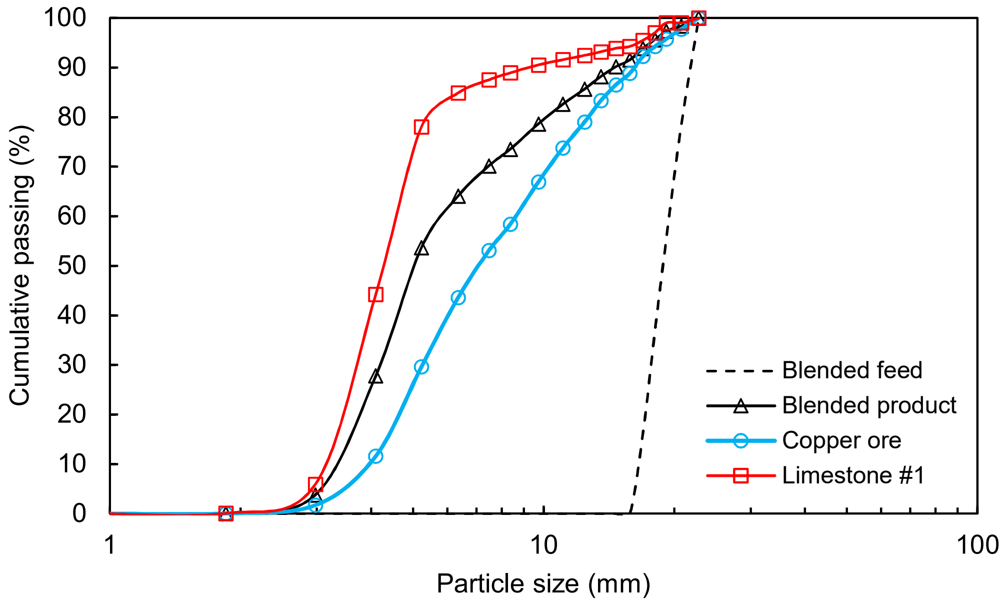

Figure 5.34 - Feed and product size distributions from simulation using a HSI crusher. Particle size distributions of the blended feed (black dashed line) and product (black continuous line) for a rotational velocity of 1089 rpm. Blue and red continuous lines represent the individual analysis of the copper ore and the limestone products that composes the blended product, respectively

On the other hand, the use of a reduced rotational velocity, such as in the case of 281 rpm, will allow most of the copper ore particles to survive the crusher without breaking due to the low energy (only 53 J/kg) applied to the particles. Limestone #1 particles, however, will break almost completely due to their lower particle fracture energies. Figure 5.35 illustrates the differential breakage between copper ore and limestone #1 particles. Results show that only 4.2% of the copper ore of the feed is reduced to particle sizes finer than 16 mm whereas 19.2% of limestone particles will not be comminuted. Table 5.7 presents the composition of the products finer and coarser than 16.0 mm based on the proportion of broken mass for both materials.

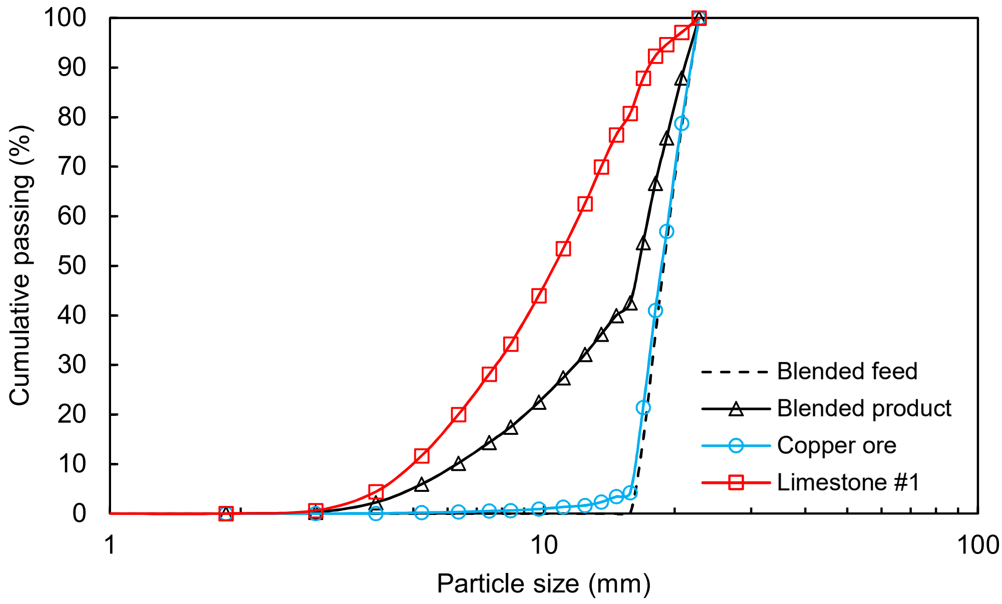

Figure 5.35 - Feed and product size distributions from simulation using a HSI crusher. Particle size distributions of the blended feed (black dashed line) and product (black continuous line) for a rotational velocity of 281 rpm. Blue and red continuous lines represent the individual analysis of the copper ore and the limestone products that composes the blended product, respectively

Table 5.7 - Composition of the products finer and coarser than 16.0 mm based on the proportion of broken mass for a rotational velocity of 281 rpm

Material	Unit	< 16.0 mm	> 16.0 mm
Copper ore	%	4.9	83.3
Limestone #1	%	95.1	16.7

In this case, it is quite clear that changing the operating conditions of the HSI crusher made it possible to further classify two different materials based only on their particle sizes due to the differences of breakage strengths. When adopting the rotational speed of 281 rpm for the impact crusher, 95.1% of the product under 16 mm will be composed of limestone #1 particles only, whereas the retained material on a 16 mm screen will be composed of 83.3% of copper ore particles. Success on selective crushing using impact crushers, however, relies on the energy distribution of a population of particles. If two materials tend to break at similar energies, then no differential breakage will occur as they will probably present the same fraction of broken particles reporting to the final product. Still, this case illustrates clearly how the Tavares breakage model is useful as a tool to optimize varied comminution processes.

6. CONCLUSIONS

Breakage description in DEM using a particle replacement scheme presents several advantages regarding the computational power needed to perform the simulations when compared to other breakage approaches. More important than that, however, is the versatility of coupling complex models to describe several properties related to breakage of ore particles. The Tavares breakage model implemented in the commercial DEM platform Rocky DEM takes advantage of this versatility by considering the intrinsic variation of fracture energy of a population of particles, the damage sustained by a particle subject to stresses of insufficient magnitude to promote particle breakage and the degree of fragmentation of a particle according to the energy applied.

The model has been tested in several comminutions systems ranging from single particle experiment tests to pilot-scale crushers in order to first verify the model response against the analytical resolutions of the model to then validate it on a basis of comparison to experimental data of different comminution tests. The various comparisons against the analytical resolutions demonstrated that the model as implemented in Rocky DEM simulation platform describes with great fidelity the response of single particles to different properties covered by the model. Sensitivity analyses of the simulations to the variation of different simulation parameters, such as the bulk Young's modulus, the coefficient of restitution and minimum size of particles, demonstrated the robustness of the model under varied conditions.

The application of the model to describe particle breakage in unconfined beds presented good agreement between simulations and experiments, being able to capture the effects of varying the impact energy, bed arrangement and material on several aspects of the tests, such as the radius of capture, the broken mass of the bed and the particle size distribution of the bed after the impact. Moreover, the model successfully described the discrepancies found in experiments regarding the broken mass of the bed composed of more than one layer according to the toughness of the material, in which the increase in the number of layers from a monolayer did not result in greater broken mass in the case of the tough copper ore, whereas more fragmentation was achieved as the number of layers was increased in the case of the soft limestone studied.

Simulations of a laboratory-scale cone crusher described properly the effect of the material strength on throughput. A small overestimation of the throughput was detected for all the materials simulated. Moreover, the model underestimated the power draw of the crusher as well as the specific energy consumption. The simulated product size distribution presented a reasonably large deviation on the coarse side of the curve due to the tendency of the Laguerre-Voronoi tessellation scheme in generating flaky fragments on a breakage event, preventing them from rebreakage as they move downwards in the crushing chamber. Nevertheless, simulations were able to properly account for the different materials.

Finally, simulations of a horizontal shaft impact (HSI) crusher illustrated the ability of the model to describe particle breakage of different materials, providing a good example of use of the model as a tool to optimize crushing circuits through the prediction of selective crushing of ores of different strengths by changing simple operating conditions of the equipment.

7. FUTURE WORK

Different comminution tests ranging from individual particles characterization tests to pilot scale tests were performed and validated in the present work. Future work using this version of the model must be performed in industrial scale comminution equipment to completely validate the model and evaluate the performance of the software when simulating a large amount of particles

Moreover, the model as implemented in version 4.3 of Rocky DEM is able to represent body breakage of ore particles. However, in some comminution situations, such as grinding, particle abrasion plays an important role in determining the size distribution of the fragments. Therefore, the implementation of a model to describe this singularity should be considered in future versions of Rocky DEM.

BIBLIOGRAPHY

BARRIOS, G. K. P., 2010, *Estudo da quebra de leitos de partículas visando a aplicação na modelagem generalizada da cominuição*. Master's Dissertation, COPPE/UFRJ, Rio de Janeiro, RJ, Brazil.

BARRIOS, G. K. P., CARVALHO, R. M., TAVARES, L. M., 2011, "Modeling breakage of monodispersed particles in unconfined beds". *Minerals Engineering*, v. 24, pp. 308–318.

BARRIOS, G. K. P., TAVARES, L. M., 2016, "A preliminary model of high pressure roll grinding using the discrete element method and multi-body dynamics coupling". *International Journal of Mineral Processing*, v. 156, pp. 32–42.

BORG, G., SCHARFE, F., KAMRADT, A., 2015, "Improved Particle Liberation by High-Velocity Comminution – the new VeRo Liberator®". *Czasopismo Naukowo-Techniczne Górnictwa Rud*, v. 2, pp. 5–14.

BRACEY, R. J., WEERASEKARA, N. S., POWELL, M. S., 2016, "Performance evaluation of the novel multi-shaft mill using DEM modelling". *Minerals Engineering*, v. 98, pp. 251–260.

CARVALHO, R. M., 2009, *Desenvolvimento de modelo matemático generalizado da cominuição*. Master's Thesis, COPPE/UFRJ, Rio de Janeiro, RJ, Brazil.

CARVALHO, R. M., 2013, *Mechanistic modelling of semi-autogenous grinding*. Doctoral thesis, COPPE/UFRJ, Rio de Janeiro, RJ, Brazil.

CARVALHO, R. M., 2018, "Modeling the mechanical degradation of coke and fines generation during handling". In: *10th Japan-Brazil Symposium on Dust Processing-Energy-Environment in Metallurgical Industries*, Sendai, September.

CARVALHO, R. M., TAVARES, L. M., 2011, "Leaping forward in SAG and AG mill simulation using a mechanistic model framework". In: *Proceedings of SAG 2011*, pp. 1–26, Vancouver, September.

CARVALHO, R. M., TAVARES, L. M., 2013, "Predicting the effect of operating and design variables on breakage rates using the mechanistic ball mill model". *Minerals Engineering*, v. 43–44, pp. 91–101.

CEPURITIS, R., JACOBSEN, S., ONNELA, T., 2015, "Sand production with VSI crushing and air classification: Optimising fines grading for concrete production with micro-proportioning". *Minerals Engineering*, v. 78, pp. 1–14.

CLEARY, P. W., 1998, "Predicting charge motion, power draw, segregation and wear in ball mills using discrete element methods". *Minerals Engineering*, v. 11, pp. 1061–1080.

CLEARY, P. W., 2001, "Recent advances in DEM modelling of tumbling mills". *Minerals Engineering*, v. 14, pp. 1295–1319.

CLEARY, P. W., MORRISON, R. D., DELANEY, G. W., 2018, "Incremental damage and particle size reduction in a pilot SAG mill: DEM breakage method extension and validation". *Minerals Engineering*, v. 128, pp. 56–68.

CLEARY, P. W., SINNOTT, M. D., 2015, "Simulation of particle flows and breakage in crushers using DEM: Part 1 - Compression crushers". *Minerals Engineering*, v. 74, pp. 178–197.

CLEARY, P. W., SINNOTT, M. D., MORRISON, R. D., *et al.*, 2017, "Analysis of cone crusher performance with changes in material properties and operating conditions using DEM". *Minerals Engineering*, v. 100, pp. 49–70.

COLA, F., BOMBACE, N., FALCO, S., *et al.*, 2017, "Concurrent adaptive mass-conserving comminution of granular materials using rigid elements". In: *Proceedings of the 7th International Conference on Discrete Element Methods*, pp. 1143–1152, Dalian, August.

CONCHA, F. A., 1995, "Value of first principles and phenomenological modeling in mineral processing". In: *XIX International Mineral Processing Congress*, pp. 9–15, São Francisco, September.

CUNDALL, P. A., 1971, "A Computer Model for Simulating Progressive, Large-scale Movement in Blocky Rock System". In: *Proceedings of the International Symposium on Rock Mechanics*, pp. 129–136, Nancy, October.

CUNDALL, P. A., 1988, "Formulation of a three-dimensional Distinct Element Method - Part I: A scheme to detect and represent contacts in a system composed of many polyhedral blocks". *International Journal of Rock Mechanics and Mining Sciences & Geomechanics Abstracts*, v. 25, pp. 107–116.

CUNDALL, P. A., STRACK, O. D. L., 1979, "A discrete numerical model for granular assemblies". *Géotechnique*, v. 29, pp. 47–65.

CUNHA, E. R., 2014, *Modelagem Mecanicista de Britadores de Impacto de Eixo Vertical*. Doctoral Thesis, COPPE/UFRJ, Rio de Janeiro, RJ, Brazil.

CUNHA, E. R., CARVALHO, R. M., TAVARES, L. M., 2014, "A predictive model of the Vertical Shaft Impact (VSI) Crusher". In: *Comminution '14*, pp. 1–12, Cape Town, April.

CUNHA, E. R., CAVALCANTI, P. P. S., SAEIDI, F., *et al.*, 2018, "On the limitation of using the JKRBT in investigating incremental breakage". *Minerals Engineering*, v. 118, pp. 33–36.

DATTA, A., RAJAMANI, R. K., 2002, "A direct approach of modeling batch grinding in ball mills using population balance principles and impact energy distribution". *International Journal of Mineral Processing*, v. 64, pp. 181–200.

DELANEY, G. W., CLEARY, P. W., MORRISON, R. D., *et al.*, 2013, "Predicting breakage and the evolution of rock size and shape distributions in AG and SAG mills using DEM". *Minerals Engineering*, v. 50–51, pp. 132–139.

DELANEY, G. W., CLEARY, P. W., SINNOTT, M. D., *et al.*, 2010, "Novel application of DEM to modelling comminution processes". In: *9th World Congress on Computational Mechanics and 4th Asian Pacific Congress on Computational Mechanics*, pp. 1–9, Sydney, July.

DELANEY, G. W., MORRISON, R. D., SINNOTT, M. D., *et al.*, 2015, "DEM modelling of non-spherical particle breakage and flow in an industrial scale cone crusher". *Minerals Engineering*, v. 74, pp. 112–122.

DEM SOLUTIONS, 2018, *EDEM 2019 Documentation*.

ECKHARDT, R., 1987, "Stan Ulam, John Von Neumann, and the Monte Carlo Method". *Los Alamos Science Special Issue*, v. 15, pp. 131–141.

FALCO, S., JIANG, J., COLA, F., *et al.*, 2017, "Generation of 3D polycrystalline microstructures with a conditioned Laguerre-Voronoi tessellation technique". *Computational Materials Science*, v. 136, pp. 20–28.

FUERSTENAU, D. W., ABOUZEID, A. Z., 2002, "The energy efficiency of ball milling in comminution". *International Journal of Mineral Processing*, v. 67, pp. 161–185.

FUERSTENAU, D. W., GUTSCHE, O., KAPUR, P. C., 1996, "Confined particle bed comminution under compressive loads". *International Journal of Mineral Processing*, v. 44–45, pp. 521–537.

FUERSTENAU, D. W., SHUKLA, A., KAPUR, P. C., 1991, "Energy consumption and product size distributions in choke-fed, high-compression roll mills". *International Journal of Mineral Processing*, v. 32, pp. 59–79.

GRÖNBERG, A., 2017, *Real-time Mesh Destruction System for a Video Game*. Bachelor’s thesis, Luleå University of Technology.

GROOT, R. D., STOYANOV, S. D., 2011, "Close packing density and fracture strength of adsorbed polydisperse particle layers". *Soft Matter*, v. 7, pp. 4750–4761.

GUPTA, A., YAN, D., 2016, *Mineral processing design and operations*.

HERBST, J. A., POTAPOV, A. V., 2004, "Making a discrete grain breakage model practical for comminution equipment performance simulation". *Powder Technology*, v. 143–144, pp. 144–150.

HERTZ, H., 1882, "On the contact of elastic solids". *J. reine angewandte Mathematik*, v. 92, pp. 156–171.

IMAI, H., IRI, M., MUROTA, K., 1985, "Voronoi Diagram in the Laguerre Geometry and Its Applications". *SIAM Journal on Computing*, v. 14, pp. 93–105.

JESWIET, J., SZEKERES, A., 2016, "Energy Consumption in Mining Comminution". In: *Procedia CIRP*, pp. 140–145, Berlim, May.

JIMÉNEZ-HERRERA, N., BARRIOS, G. K. P., TAVARES, L. M., 2018, "Comparison of breakage models in DEM in simulating impact on particle beds". *Advanced Powder Technology*, v. 29, pp. 692–706.

KHANAL, M., SCHUBERT, W., TOMAS, J., 2005, "DEM simulation of diametrical compression test on particle compounds". *Granular Matter*, v. 7, pp. 83–90.

KHANAL, M., SCHUBERT, W., TOMAS, J., 2007, "Discrete element method simulation of bed comminution". *Minerals Engineering*, v. 20, pp. 179–187.

KING, R. P., 2001, *Modeling and Simulation of Mineral Processing Systems*.

LICHTER, J., LIM, K., POTAPOV, A., *et al.*, 2009, "New developments in cone crusher performance optimization". *Minerals Engineering*, v. 22, pp. 613–617.

LIU, J., SCHÖNERT, K., 1996, "Modelling of interparticle breakage". *International Journal of Mineral Processing*, v. 44–45, pp. 101–115.

LUZ, A. B., SAMPAIO, J. A., ALMEIDA, S. L. M., 2004, *Tratamento de minérios*.

MAGALHÃES, F. N., TAVARES, L. M., 2014, "Rapid ore breakage parameter estimation from a laboratory crushing test". *International Journal of Mineral Processing*, v. 126, pp. 49–54.

METZGER, M. J., GLASSER, B. J., 2013, "Simulation of the breakage of bonded agglomerates in a ball mill". *Powder Technology*, v. 237, pp. 286–302.

MINDLIN, R., 1949, "Compliance of elastic bodies in contact". *Journal of Applied Mechanics*, v. 16, pp. 259–268.

MINDLIN, R., DERESIEWICZ, H., 1953, "Elastic spheres in contact under varying oblique forces". *Journal of Applied Mechanics*, v. 20, pp. 237–344.

MORRELL, S., NAPIER-MUNN, T. J., ANDERSEN, J., 1992, "The prediction of power dram in comminution machines". In: *Comminution: Theory and Practice. Proceedings*, pp. 233–247, Phoenix, February.

MORRISON, R. D., CLEARY, P. W., 2004, "Using DEM to model ore breakage within a pilot scale SAG mill". *Minerals Engineering*, v. 17, pp. 1117–1124.

MWANGA, A., ROSENKRANZ, J., LAMBERG, P., 2015, "Testing of Ore Comminution Behavior in the Geometallurgical Context—A Review". *Minerals*, v. 5, pp. 276–297.

NAPIER-MUNN, T., 2015, "Is progress in energy-efficient comminution doomed?". *Minerals Engineering*, v. 73, pp. 1–6.

NAPIER-MUNN, T. J., MORRELL, S., MORRISON, R. D., *et al.*, 1996, *Mineral Comminution Circuits - Their Operation and Optimisation*.

NARAYANAN, S. S., WHITEN, W. J., 1988, "Determination of comminution characteristics from single-particle breakage tests and its application to ball-mill scale-up". *Transactions of the Institute of Mining and Metallurgy*, v. 97, pp. C115–C124.

OROZCO, L. F., DELENNE, J.-Y., SORNAY, P., *et al.*, 2019, "Discrete-element model for dynamic fracture of a single particle". *International Journal of Solids and Structures*, v. 166, pp. 47–56.

PATWA, A., AMBROSE, R. P. K., CASADA, M. E., 2016, "Discrete element method as an approach to model the wheat milling process". *Powder Technology*, v. 302, pp. 350–356.

PAUW, O. G., MARÉ, M. S., 1988, "The determination of optimum impact-breakage routes for an ore". *Powder Technology*, v. 54, pp. 3–13.

PORTELA, J. N., ALENCAR, M. S., 2008, "Cellular Coverage Map as a Voronoi Diagram". *Journal of Communication and Information Systems*, v. 23, pp. 22–31.

POTAPOV, A. V., CAMPBELL, C. S., 1994, "Computer simulation of impact-induced particle breakage". *Powder Technology*, v. 81, pp. 207–216.

POTAPOV, A. V., CAMPBELL, C. S., 1996, "a Three-Dimensional Simulation of Brittle Solid Fracture". *International Journal of Modern Physics C*, v. 7, pp. 717–729.

POTAPOV, A. V., HERBST, J. A., SONG, M., *et al.*, 2007, "A DEM-PBM fast breakage model for simulation of comminution processes". In: *Proceedings of Discrete Element Methods*, Brisbane, August.

POTAPOV, A. V., HOPKINS, M. A., CAMPBELL, C. S., 1995, "a Two-Dimensional Dynamic Simulation of Solid Fracture Part I: Description of the Model". *International Journal of Modern Physics C*, v. 06, pp. 371–398.

POTAPOV, A. V, CAMPBELL, C. S., 2000, "The breakage induced by a single grinding ball dropped onto a randomly packed particle bed". *Powder Technology*, v. 107, pp. 108–117.

POTYONDY, D. O., CUNDALL, P. A., 2004, "A bonded-particle model for rock". *International Journal of Rock Mechanics and Mining Sciences*, v. 41, pp. 1329–1364.

QUIST, J., EVERTSSON, C. M., 2016, "Cone crusher modelling and simulation using DEM". *Minerals Engineering*, v. 85, pp. 92–105.

QUIST, J., EVERTSSON, M., FRANKE, J., 2011, "The Effect of Liner Wear on Gyratory Crushing – A DEM Case Study". In: *3rd International Computational Modelling Symposium by MEI*, Falmouth, June.

ROCKY DEM, 2018, *DEM Technical Manual 4.2*.

RUMPF, H., 1973, "Physical aspects of comminution and new formulation of a law of comminution". *Powder Technology*, v. 7, pp. 145–159.

SAEIDI, F., TAVARES, L. M., YAHYAEI, M., *et al.*, 2016, "A phenomenological model of single particle breakage as a multi-stage process". *Minerals Engineering*, v. 98, pp. 90–100.

SCHÖNERT, K., 1972, "Role of Fracture Physics in Understanding Comminution Phenomena". *AIME Transactions*, v. 252, pp. 21–26.

SCHUBERT, W., KHANAL, M., TOMAS, J., 2005, "Impact crushing of particle-particle compounds - Experiment and simulation". *International Journal of Mineral Processing*, v. 75, pp. 41–52.

SEVILLE, J., WU, C. Y., 2016. "Chapter 9 - Discrete Element Methods". *Particle Technology and Engineering*. Butterworth-Heinemann: pp. 213–242.

SHI, F., KOJOVIC, T., 2007, "Validation of a model for impact breakage incorporating particle size effect". *International Journal of Mineral Processing*, v. 82, pp. 156–163.

SHI, F., KOJOVIC, T., LARBI-BRAM, S., *et al.*, 2009, "Development of a rapid particle breakage characterisation device - The JKRBT". *Minerals Engineering*, v. 22, pp. 602–612.

SINNOTT, M. D., CLEARY, P. W., 2015, "Simulation of particle flows and breakage in crushers using DEM: Part 2 - Impact crushers". *Minerals Engineering*, v. 74, pp. 163–177.

TAVARES, L. M., 2004, "Optimum routes for particle breakage by impact". *Powder Technology*, v. 142, pp. 81–91.

TAVARES, L. M., 2007. "Chapter 1 - Breakage of Single Particles: Quasi-Static". *Handbook of Powder Technology*. Elsevier: pp. 3–68.

TAVARES, L. M., 2009, "Analysis of particle fracture by repeated stressing as damage accumulation". *Powder Technology*, v. 190, pp. 327–339.

TAVARES, L. M., 2017, "A review of advanced ball mill modelling". *KONA Powder and Particle Journal*, v. 34, pp. 106–124.

TAVARES, L. M., CARVALHO, R. M., 2007, "Impact work index prediction from continuum damage model of particle fracture". *Minerals Engineering*, v. 20, pp. 1368–1375.

TAVARES, L. M., CARVALHO, R. M., 2009, "Modeling breakage rates of coarse particles in ball mills". *Minerals Engineering*, v. 22, pp. 650–659.

TAVARES, L. M., CARVALHO, R. M., 2012, "Modeling ore degradation during handling using continuum damage mechanics". *International Journal of Mineral Processing*, v. 112–113, pp. 1–6.

TAVARES, L. M., CARVALHO, R. M., SILVEIRA, M. W. DA, *et al.*, 2015, "Degradação mecânica de pelotas de minérios de ferro durante o manuseio e transporte. Parte 1: Modelo matemático e simulador". In: *Anais do 16º Simpósio de Minério de Ferro*, pp. 1–11, Rio de Janeiro, August.

TAVARES, L. M., CAVALCANTI, P. P., CARVALHO, R. M., *et al.*, 2018, "Fracture probability and fragment size distribution of fired Iron ore pellets by impact". *Powder Technology*, v. 336, pp. 546–554.

TAVARES, L. M., KING, R. P., 1998, "Single-particle fracture under impact loading". *International Journal of Mineral Processing*, v. 54, pp. 1–28.

TAVARES, L. M., KING, R. P., 2002, "Modeling of particle fracture by repeated impacts using continuum damage mechanics". *Powder Technology*, v. 123, pp. 138–146.

TRIMBLE INC, 2016, *SketchUp Make 17.2.2555*.

VERVOORN, P. M. M., AUSTIN, L. G., 1990, "The analysis of repeated breakage events as an equivalent rate process". *Powder Technology*, v. 63, pp. 141–147.

VOGEL, L., PEUKERT, W., 2003, "Breakage behaviour of different materials - Construction of a mastercurve for the breakage probability". *Powder Technology*, v. 129, pp. 101–110.

VOGEL, L., PEUKERT, W., 2005, "From single particle impact behaviour to modelling of impact mills". *Chemical Engineering Science*, v. 60, pp. 5164–5176.

WALTON, O. R., BRAUN, R. L., 1986, "Viscosity, granular-temperature, and stress calculations for shearing assemblies of inelastic frictional disks". *Journal of Rheology*, v. 30, pp. 948–980.

WEERASEKARA, N. S., POWELL, M. S., CLEARY, P. W., *et al.*, 2013, "The contribution of DEM to the science of comminution". *Powder Technology*, v. 248, pp. 3–24.

WEJRZANOWSKI, T., SKIBINSKI, J., SZUMBARSKI, J., *et al.*, 2013, "Structure of foams modeled by Laguerre-Voronoi tessellations". *Computational Materials Science*, v. 67, pp. 216–221.

WILLS, B. A., NAPIER-MUNN, T., 2006, *Mineral Processing Technology - An Introduction to the Practical Aspects of Ore Treatment and Mineral Recovery*.